

Hydrogen Interaction with Supermartensitic Stainless Steel studied by Energy Dispersive X-Ray Diffraction

Dissertation

zur Erlangung des akademischen Grades

Doktoringenieur

(Dr.-Ing.)

Von M.Sc. Eitan Dabah

geb. am 10, September 1981 in Rechovot, Israel

Genehmigt durch die Fakultät für Maschinenbau
der Otto-Von-Guericke-Universität Magdeburg

Gutachter:

Prof. Dr.-Ing. habil. Thomas Böllinghaus

Prof. Dan Eliezer

Dr.-Ing. Arne Kromm

Promotionskolloquium am 17. Juni 2015

Acknowledgements

- ❖ *I would like to express my appreciation to my supervisors Prof. Dan Eliezer and Prof. Thomas Böllinghaus for their thorough guidance, continuous support, useful comments and engagement through the process of this PhD work.*
- ❖ *Especially I would like to thank Dr. Arne Kromm for the priceless contributions for the preparation and the conduction of this work, and for his support through fruitful ideas and discussions.*
- ❖ *My gratitude to Prof. Thomas Kannengießer for his inestimable help and contribution in this research.*
- ❖ *Special thanks to Dr. Axel Griesche for his support and original ideas and the help in the scientific discussions.*
- ❖ *My sincere gratitude to the team members and colleges; Katrin Beyer, Dr. Tobias Mente, Franka Straub, Dr. Diana Marcano and Michael Rhode for sharing knowledge with me and assisting with fruitful brain storming and scientific discussions.*
- ❖ *My brother, Dr. Sharon Dabach for giving me his scientific perspective to help me improve the quality of this dissertation.*
- ❖ *Last but not least I would like to give special thanks to Georgia, my fiancée for her mental support during the hard times of my PhD work.*

Abstract

Over a century ago it was found that hydrogen can assist in the occurrence of premature failure of a serving metal component. This phenomenon was referred to as hydrogen embrittlement (HE), and later, as it was found that hydrogen is not solely contributing to the cracking process, it was referred to as Hydrogen Assisted Cracking (HAC). There are several existent suggested mechanisms explaining this phenomenon and the occurrence of the unexpected premature failure of the metal component. These suggested mechanisms are different from each other in principle. However, the common to these mechanisms is the dependence of the failure mechanism on the ability of the hydrogen atoms to reach the areas of defects and stress concentration, consequently assisting in the crack initiation and propagation process, i.e. the mobility of the hydrogen atoms in the material. There were several researches dealing with the issue of hydrogen transport in a material by several different experimental methods. However, none of these studies was able to perform an in-situ measurement and examination of the mentioned phenomenon. In the presented study, the lattice diffusion of hydrogen, which is one of the most important hydrogen transport mechanisms, was studied in supermartensitic stainless steel using energy dispersive X-ray diffraction technique. This technique allows for phase specific in-situ examination of mass transport of solute interstitial atoms, which can be examined through the changes of the material's lattice parameter. Moreover, the interaction between the residual stresses in the material and hydrogen was examined as well. It was found that EDXRD technique is beneficial for the in-situ study of hydrogen phase specific diffusion characteristics. An unequivocally tendency of the effusion process was observed and characterized, and diffusion coefficients were calculated at ambient temperature. It was found that the Hydrogen diffusion coefficients for the austenitic phase are about one order of magnitude smaller than those for the martensitic phase. Moreover, some former statements of other researchers were confirmed using such procedure.

The behavior of the residual stresses present in the material in the presence of hydrogen was studied as well. It was found that hydrogen interact in a reversible manner with the residual stresses in the material, as they regain their original value after desorption of the hydrogen.

Table of Contents

1.	Introduction	1
2.	Literature Review	3
2.1.	Supermartensitic stainless steel (SMSS)	3
2.2.	Hydrogen interaction with metallic material	7
2.2.1.	Hydrogen induced lattice distortions and phase transformations	7
2.2.2.	Hydrogen interaction with lattice defects (hydrogen trapping)	10
2.2.3.	Thermal desorption spectroscopy for hydrogen trapping characterization	15
2.3.	Hydrogen transport	16
2.3.1.	Hydrogen diffusion in SMSS	18
2.4.	Hydrogen Assisted Cracking (HAC)	19
2.4.1.	The pressure theory	21
2.4.2.	The absorption model	23
2.4.3.	Embrittlement caused by hydride formation	24
2.4.4.	Hydrogen Enhanced Decohesion Theory (HEDE)	26
2.4.5.	Hydrogen Enhanced Localized Plasticity (HELP)	28
2.4.6.	Adsorption induced Dislocation Emission (AIDE)	31
2.5.	Effect of hydrogen trapping on HAC	33
2.6.	HAC of SMSS and of SMSS in flowlines	36
2.6.1.	The role of the retained austenite in the embrittlement process of SMSS	42
2.7.	Fundamentals of X-ray Diffraction (XRD)	43
2.8.	Residual stresses	45
2.8.1.	Hydrogen interaction with residual stresses	47
3.	Objectives of the study	51
4.	Experimental procedure	53
4.1.	Supermartensitic stainless steel	53

4.2.	Hydrogen cathodic charging	55
4.3.	Carrier Gas Hot Extraction system (CGHE)	56
4.4.	Hydrogen desorption measurements by means of Energy Dispersive X-ray Diffraction.....	58
4.4.1.	Hydrogen desorption by degassing at room temperature	58
4.4.2.	Hydrogen degassing at elevated temperatures	63
4.5.	Residual stress measurements using XRD	64
4.5.1.	Mobile diffractometer for residual stress determination.....	66
4.5.2.	Synchrotron radiation for residual stress measurements	67
4.6.	Calculation of phase composition using X-ray Diffraction.....	68
4.7.	Other experimental methods.....	69
4.7.1.	Tensile test	69
4.7.2.	Optical microscopy.....	70
4.7.3.	Scanning electron microscopy (SEM)	70
5.	Results and discussion.....	71
5.1.	Microstructural analysis.....	71
5.2.	HE of the tested alloy	73
5.3.	Solubility of hydrogen in the tested material.....	75
5.4.	Hydrogen desorption at room temperature	77
5.5.	Hydrogen desorption during continuous heating.....	92
5.6.	Hydrogen interaction with residual stresses	102
6.	Conclusions and Perspectives	115
7.	References.....	118
8.	List of Figures	134
9.	List of Tables	142

1. Introduction

Once hydrogen is introduced to a metallic material it may cause serious degradation to the mechanical properties. This is commonly referred to as Hydrogen Embrittlement (HE) [1–3]. HE was first reported in 1874 by Johnson [4] and since then it presented a persistent problem for the applications of structural materials and therefore has been the subject of numerous studies over several decades.

In addition to internal and external mechanical loads in terms of stresses and particular strains such degradation of the material's mechanical properties might result in more or less brittle cracking of components in engineering approach (low extent of plastic deformation until failure disregarding the fracture surface). Since hydrogen is not solely responsible for the cracking process, and cracking is always introduced in the presence of mechanical load, this phenomenon is referred to as Hydrogen Assisted Cracking (HAC). The metallurgical mechanisms of HAC are not yet completely understood and numerous theories have been provided since the 1940's. More recently it has been assumed that HAC of metallic engineering materials, in particular steels and stainless steels, is a consequence of two interacting mechanisms between hydrogen and a metal matrix, namely the Hydrogen Enhanced Decohesion (HEDE) and the Hydrogen Enhanced Localized Plasticity (HELP) [5–8]. However, necessary for these theories in particular and for HAC in general is an understanding of the hydrogen diffusion and trapping behavior in the respective investigated microstructure [9,10]. In addition, phase transformations associated with the presence of hydrogen in the microstructure are also relevant for HAC [11–13]. Moreover, both of the above mentioned mechanisms are strongly dependent on the stresses which are present in the material (whether external or internal), as well as the interaction of the hydrogen atoms with those stresses.

Supermartensitic stainless steel (SMSS) is a classic example of a HAC susceptible material [14–20]. In these types of steels, a high hydrogen concentration can build up during electrochemical processes, such as cathodic protection or electrochemical corrosion resistance coating (e.g. zinc coating) [21], and/or during welding processes [22]. These processes were quite often applied to this steel, as it is widely used in the offshore industry for pipelines for oil and gas transportation [23]. During this service, the steel components are subjected to mild sour environments (having a lower pH value, usually due to significant H₂S saturation) and corrosion protection measures were applied to these steel components

in the past. However, the application of such measures has proven to be detrimental to the used SMSS due to occurrence of HAC, and is consequently not being applied anymore when SMSS are used.

As previously mentioned, hydrogen transport and trapping play a critical role in HAC. Notwithstanding where the few suggested embrittlement mechanisms defer, their common issue is hydrogen's ability to reach the area of stress concentration and to assist in the crack initiation and propagation process. So far, there are several existent methods to determine the hydrogen transport ability in a material. For instance, the electrochemical permeation technique enables the calculation of hydrogen effective diffusion coefficient in accordance to the time it takes for hydrogen atoms to permeate through a metal membrane [24–29].

However, as efficient as these methods are they offer no possibility of separating microstructure effects or determining the diffusion characteristic such as diffusion path, i.e. lattice diffusion, diffusion through dislocations or grain and phase boundaries.

The main objective of this work is to in-situ examine the hydrogen transport and trapping phenomenon in a metal lattice by using synchrotron radiation Energy Dispersive X-Ray Diffraction (EDXRD). The latter should be established as a beneficial and efficient new method for this kind of in-situ examinations. Additionally, an examination of the interaction and influences of hydrogen presence on the stresses state in the material will also be conducted. These examinations should lead to a further understanding of the hydrogen transport phenomenon and for further development of the existing models for HAC mechanisms.



Figure 1-1: A marine vessel for welding and placement of the SMSS pipelines for the oil and gas transportation industry

2. Literature Review

2.1. Supermartensitic stainless steel (SMSS)

Martensitic stainless steels are iron based alloys containing mainly alloying elements such as chromium, nickel and molybdenum. Designed in the early 90's, they serve as a low cost replacement for duplex stainless steels for offshore applications due to their lower nickel and chromium content, which are the most expensive elements in the alloy [30,31]. These steels possess a Body Centered Tetragonal (BCT) crystal structure in the hardened condition. The martensitic structure contains fine distributed retained and annealing austenite between the martensitic laths. This structure is illustrated in Figure 2-1.

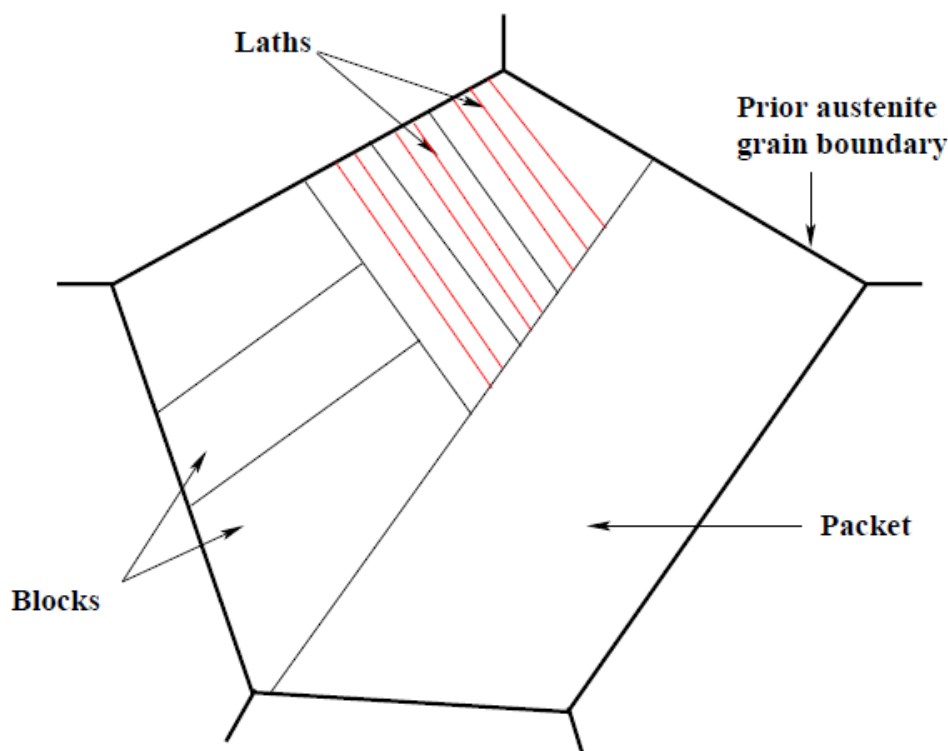


Figure 2-1: Schematic illustration of the microstructural features of SMSS

The dominant phase in these alloys is the martensitic phase which grants the alloy its desired strength. This phase is a result of a shear transformation of prior austenite under rapid cooling to room temperature. Under the mentioned conditions the martensite is forced to adopt a lath shape in alloys containing a carbon content of less than 0.6 wt-%. Usually

this lath structure is too fine to be observed by optical microscopy and it implies the use of electron microscopy [31]. The hardness of the martensitic phase depends on the carbon content. Carbon trapped in the lattice of the martensitic phase cause tetragonal strain and grants it its BCT structure. This strain reduces the dislocation mobility and thus achieves higher hardness. Since the carbon content is smaller in the super grades, these are consequently softer than the normal ones. This is compensated by the high amount of alloying elements such as chromium which reduces the M_s temperature and consequently achieves higher hardness under the same quenching conditions.

The retained austenite present in those steels is usually a result of an uncompleted martensitic transformation due to the initial cooling temperature and the duration of the quenching procedure. It can be also introduced by the thermos mechanical heat treatment that follows quenching, usually the annealing heat treatment. This phase is enriched with the austenite stabilizing elements such as nickel, nitrogen etc. When this phase is finely distributed between the martensitic laths it decreases the hardness of the alloy and improves its ductility. This is attributed to the presence of stress concentration in the vicinity of the austenite islands and the release of the energy by the martensitic phase transformation and consequently the inhibition of the crack propagation [32].

In addition, these steel grades possess an increased chromium concentration (of about 11-14 wt.-%) for stabilizing the BCC structure and for enhanced corrosion resistance. These grades have also reduced nickel concentration (of about 4-6 wt.-%), which grants them the better price efficiency over the duplex stainless steel grades. The latter have a superior corrosion and HE resistance due to their microstructure and high alloying, but are less economical than the supermartensitic.

The SMSS are divided into three main categories in accordance to their level of alloying. The classifications mainly depend on the most important alloying elements which are chromium, nickel and molybdenum. Additionally, the high cost of these three elements makes them the most significant factor effecting the alloy's price [33]. The SMSS are categorized as Lean, Medium and High alloyed as described and specified in Table 2-1.

Table 2-1: The three main SMSS grade in accordance to the concentration of alloying elements (the values are presented in wt.-%) [34–36]

	Cr	Ni	Mo	C
Lean alloy	11	2	-	<0.02
Medium alloy	12	4.5	1.5	<0.02
High alloy	12	6.5	2.5	<0.02

The microstructure of SMSS is dependent mainly on its alloying elements. Increased nickel concentration is crucial for obtaining the austenite to martensite transformation. In order to estimate the martensite formation for the specific alloy, one can use the M_s Temperature dependence on the alloying elements for 13 wt.-% Cr martensitic steel [37]:

$$(2-1) \quad M_s = 300 - 474C - 33Mn - 17Ni - 17(Cr - 12) - 21Mo - 11W - 11Si$$

The M_s , M_f and Ac_1 temperatures for the above mentioned martensitic steels categories are summarized in table 2-2.

Table 2-2: Martensite start, martensite final and Ac_1 temperatures of the martensitic stainless steel categories [33]

	Lean alloy	Medium alloy	High alloy
Martensite start M_s	360	250	150
Martensite finish M_f	220	120	30
Austenization Ac_1	650	640	630

In the annealed condition, martensitic stainless steels have tensile yield strength of over 600 MPa and they can be moderately hardened by cold working. However, these alloys are typically heat treated by hardening and tempering in order to increase the yield strength up to about 1900 MPa. The hardness of these alloys is ranging from about 150 HB for the annealed condition up to values above 600 HB for fully hardened condition [38].

SMSS are ferromagnetic, hardenable by heat treatments, and resistant to corrosion only in relatively mild environments. These steels have similar mechanical properties as standard martensitic steels. However, this type of steel exhibits very good weldability.

All the grades of SMSS have a low carbon concentration of <0.02 wt.-% (LC) which allows superior weldability of these grades due to limited sensitization. Some alloys are also designed as ELC steels, having an extra low carbon content of <0.001 wt.-%. The low carbon concentration reduces the formation of chromium carbides (e.g. Cr_{23}C_6 , Cr_7C_3 and Cr_3C_2) at elevated temperatures, usually at the heat affected zone (HAZ). These carbides tend to segregate mostly at grain boundaries and they possess a cathodic potential in comparison to the iron matrix. Moreover, these carbides can act as hydrogen sinks if the latter is present. Therefore these chromium carbides are responsible for deteriorated corrosion and HAC resistance of the welded steel, especially at the HAZ, and their formation should be avoided in welding or at any other service under elevated temperature conditions [39].

The mechanical properties of SMSS are dependent on the microstructure and alloying elements such as carbon, and on the material processing such as heat treatment processes and cold working [33,40]. SMSS with the yield strength of 550 MPa are usually applied for the offshore industry as pipelines for transporting oil and gas products, where the material is subjected to high pressure and sour environments. The ductile-Brittle Transformation Temperature, which is very low in these types of steel, also plays an important role for pipeline applications in the North Sea. Thus, high alloyed SMSS are applied for -50°C service conditions.

Beside the mechanical properties dependency on the alloying elements, the mechanical properties can be also improved by appropriate heat treatment. For example after welding, post treated weld metal has an increased impact toughness and higher ultimate tensile strength (UTS) after austenitization heat treatment [40]. This heat treatment includes annealing at temperatures between 950°C and 1000°C for 2 hours and then quenching in cooled air. Afterwards the steel is heated up to 600°C for 6 hours and quenched in air again [41]. Such procedure provides a fine distributed austenitic phase and the desired mechanical properties.

SMSS are applied when the application requires good to excellent mechanical properties such as tensile strength, creep and fatigue resistance, combined with moderate

corrosion and HAC resistance. These steels are applied mainly in the petrochemical and petroleum industry as pipelines for transportation of fossil fuels (e.g. gas or oil) due to their mechanical properties, corrosion resistance, and especially due to their superior weldability as described earlier.

Martensitic steels with increased molybdenum concentration, possess higher corrosion resistance and mechanical properties, and as such, are used as cutlery, valve parts, gears, rollers and shafts. High carbon level grades of martensitic stainless steels (type 440 grade) are used for surgical and dental instruments [31].

2.2. Hydrogen interaction with metallic material

The interaction of hydrogen with metals characterizes the fundamental aspects of absorption, desorption and diffusion. These aspects are inherently dependent on factors such as lattice diffusion, interaction of hydrogen with lattice defects (trapping) and interaction of the hydrogen atoms with the crystal lattice. These theories will be widely discussed in the following sections.

2.2.1. Hydrogen induced lattice distortions and phase transformations

As hydrogen is introduced into a metallic material, it induces lattice distortions. This phenomenon has been published in previous researches and was mainly conducted on austenitic stainless steels and titanium alloys. It was shown that hydrogen causes significant distortions in a metal matrix. These distortions may be lattice inter atomic spacing expansion or phase transformations [42–49]. When hydrogen is absorbed into an ideal metallic lattice it occupies octahedral or tetrahedral sites depending on the lattice structure (body centered or face centered) of the matrix, as described in Figure 2-2 (for cubic crystal structures). By this occupation of the interstitial sites, the presence of hydrogen induces elastic stresses upon the lattice. These stresses then induce the expansion of the lattice or stress induced phase transformations such as austenitic to martensitic transformation. In addition, in some metal hydrogen can bind with the metal atoms or with the alloying elements to form hydrides.

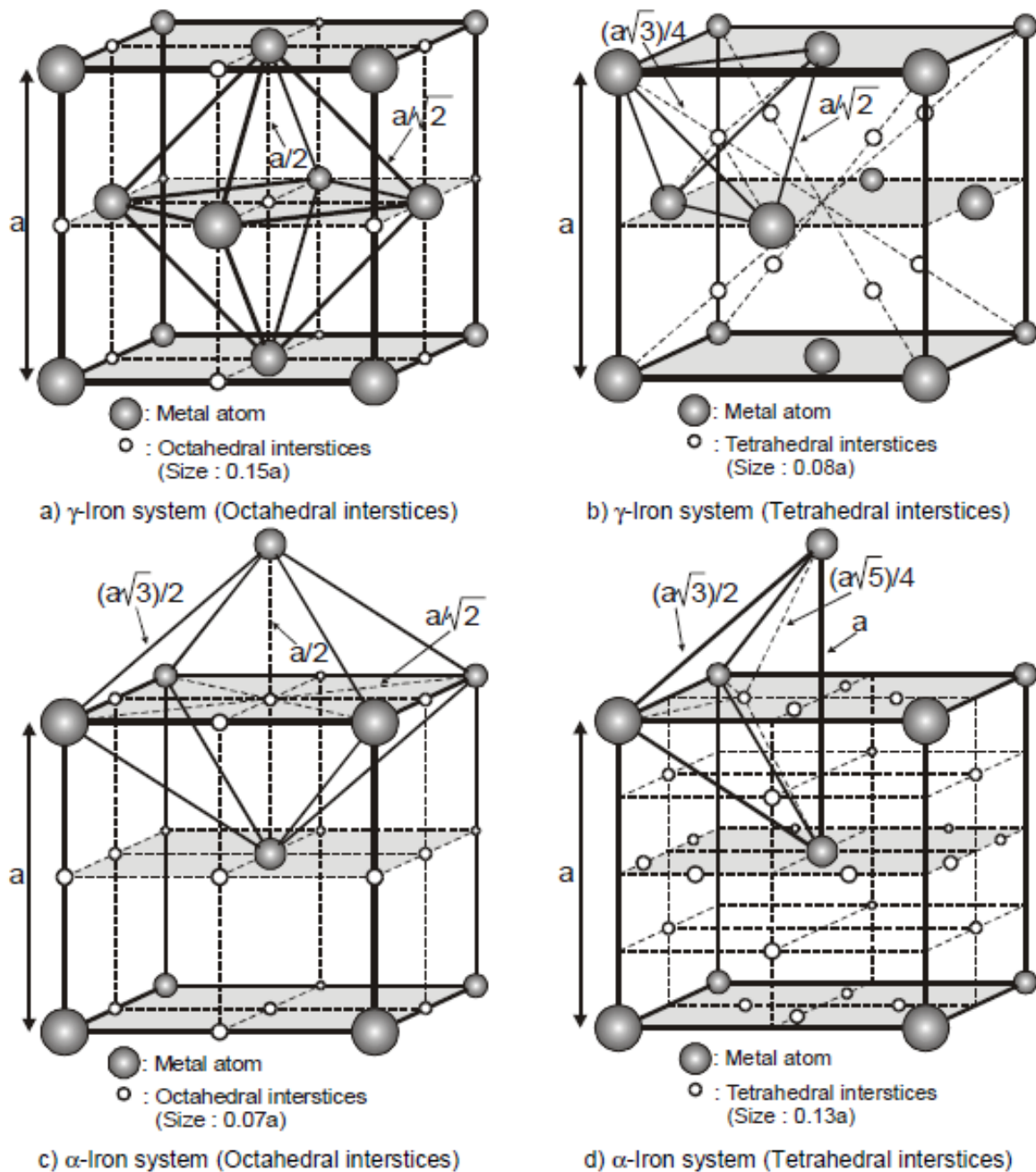


Figure 2-2: Schematic illustration of the interstitial sites (octahedral and tetrahedral sites) for foreign atoms in BCC and FCC crystal structures [50]

It was first shown by Narita et al. [46] that hydrogen can induce a phase transformation in an austenitic stainless steel, i.e. the austenite phase transforms into a pseudo hydride phase named γ^*/γ_H having the same FCC crystal structure, with a 6% volume increase compared to the hydrogen free γ phase. This occurs in the case of a very stable austenitic phase (e.g. nickel rich austenite). Later, Rozenak et al. [44,49] and Ulmer et al. [42] showed the influence of different hydrogen charging durations (hence different hydrogen

concentrations) on the phase composition of austenitic stainless steels with a less stable austenitic phase. It became evident that hydrogen spontaneously introduces ϵ -martensite, i.e. a stress induced martensitic phase with a HCP (Hexagonal Close Pack) crystal structure, and definitely causes broadening of the lattice inter atomic spacing as this martensitic phase is hydrogen rich, as can be seen in Figure 2-3. It was shown later by Rozenak and Eliezer [51] that the lattice inter atomic spacing contracts during degassing of the hydrogen charged sample as the hydrogen desorbs from it. During this degassing process at ambient temperature, there were evidence for the formation of the α' martensitic phase.

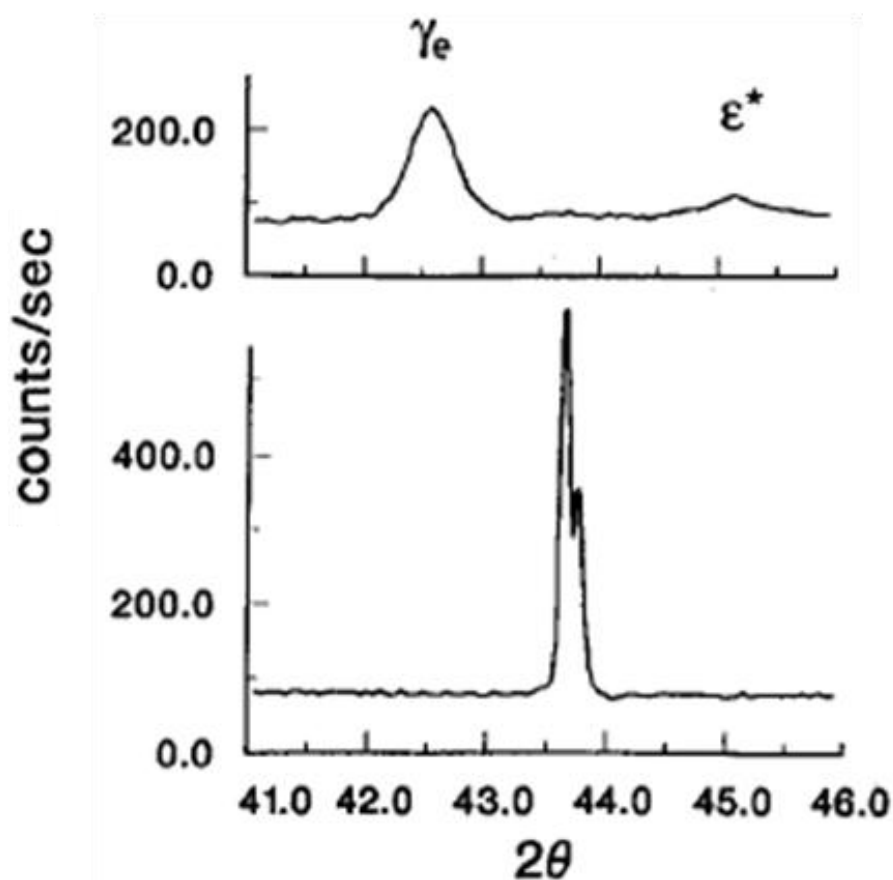


Figure 2-3: Evidence for the formation of hydrogen rich HCP ϵ^* phase after hydrogen charging up to 25 at.% in austenitic stainless steel [42]

It can be deduced from these studies that for every type of steel containing an austenitic phase, such as duplex steel or martensitic steel, a martensitic transformation can occur during the introduction of hydrogen and the accompanying stresses in the material. The

character of the respective martensitic transformation depends on the alloying elements that are present in the austenitic phase and the correspondent stability of this phase.

Expansion of the metallic lattice have also been observed as hydrogen was introduced into titanium alloys, together with the formation of a titanium hydride phase TiH_2 [52,53]. Such hydrogen influences have also been detected while observing various two phase steel such as duplex and martensitic stainless steels [54,55].

2.2.2. Hydrogen interaction with lattice defects (hydrogen trapping)

For a homogenous solution of hydrogen inside a metal lattice, a preliminary condition of ideal single crystal is required, as well as hydrogen concentrations below the solubility limit. However, ideal single crystals are extremely rare, and therefore the hydrogen distribution inside the metal lattice is affected by interaction of the hydrogen single atoms (adatoms) with defects and inhomogeneities in the lattice crystal. In the vicinity of these inhomogeneities, the mean residence time of the hydrogen adatoms is significantly longer than in interstitial sites in the lattice because of energetic benefits [56]. These inhomogeneities and defects can be dislocations, vacancies, impurities, grain boundaries, second phase particles and voids, as illustrated in Figure 2-4 [57]. Those defects and inhomogeneities are usually referred to as hydrogen trap sites. Hence, the distribution of hydrogen in the material is normally not homogeneous and the majority of the hydrogen is located at the vicinity of the hydrogen traps. As the interaction between hydrogen atoms and traps increases, usually through the increased amount of hydrogen traps, the capacity of hydrogen in the metal will increase [58–60].

The trapping theory was first suggested by McNabb and Foster in the early 1960's [61] and was exhibited as a mathematical model. This particular idea of trapping came from the observation that hydrogen diffusion in a metallic material does not correspond to Fick's law of diffusion (for diffusion at lower temperatures than 400°C). According to their theory, hydrogen trapping occurs when the hydrogen free energy in a certain location in the lattice is smaller than its energy in the lattice interstitial site. Consequently, the mean time for hydrogen residence inside this specific location is longer than the mean time for hydrogen residence in a normal lattice interstitial site. This effect is referred to as the trap's "binding energy" as described in Figure 2-5 [58].

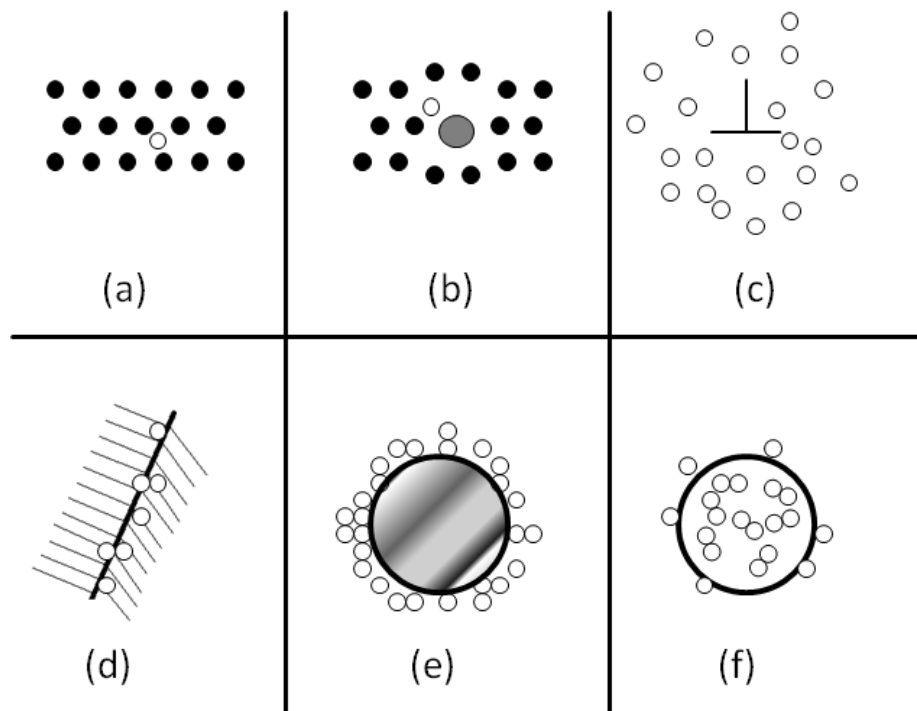


Figure 2-4: Schematic view of examples of destinations for hydrogen in a metal microstructure: (a) solid solution; (b) solute–hydrogen pair; (c) dislocation atmosphere; (d) grain boundary accumulation; (e) particle–matrix interface accumulation; (f) void containing recombined hydrogen (redrawn from Dayal [57])

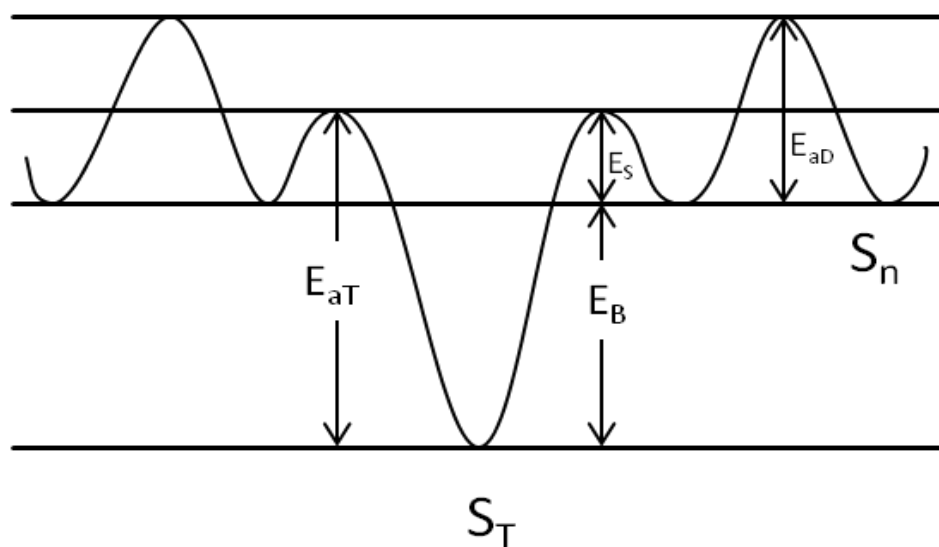


Figure 2-5: Schematic of energy near a trap site where S_T is the trap site, S_n is a lattice interstitial site, E_{aD} is the activation energy for hydrogen diffusion for an atom located in lattice interstitial site, E_s is the saddle energy, E_B is the trap binding energy (redrawn from Lee [62])

When a hydrogen atom jumps from a normal lattice site into a trap, the probability of an eventual return to the former site is relative small due to the energetic barrier. There are two main reasons why, in a crystal lattice, those jump probabilities should be modified. This is illustrated in Figure 2-6 a and b: in case that there is a certain force that pushes the hydrogen atoms in a preferred direction, or the lattice is distorted and may even be completely modified [63].

These reasons are sufficient to distinguish between two extreme types of traps; namely attractive traps and physical traps [63].

Attractive trap (illustrated in Figure 2-6 c) is a region of the lattice where hydrogen atoms are subjected to an attractive force such as an electric field, stress field, temperature gradient or to a certain chemical potential gradient. Stress fields are usually concentrated at the vicinity of defects such as dislocations, coherent and semi coherent grain boundaries and particles, crack tips etc. [63].

Physical trap (illustrated in Figure 2-6 d) is a site in the lattice in which a diffusing hydrogen atom will be trapped randomly rather than be attracted to. This type of traps exists due to modifications of the ideal crystal lattice such as high angle grain boundaries, incoherent particles or interfaces, voids etc. Hydrogen is energetically more favorable to stay in this type of trap rather than in interstitial lattice site.

Mixed trap (illustrated in Figure 2-6 e) is the most common type of hydrogen traps since in the very majority of the cases both of the mentioned characteristics are present, and only in an extreme case will the trap present only one of the above mentioned characteristics. An example of a mixed trap is an edge dislocation; the attractive character is due to the stress field, and the physical character is due to the region of the dislocation's core where the lattice is distorted and free chemical connections are available.

Concerning the reversibility of a trap, namely the ability of a hydrogen atom to be released from this site, it is easier for a hydrogen atom to diffuse out from an attractive trap than from a physical one. This applies for the case assuming pure physical characteristic and pure attractive characteristic of the traps with a same trap depth E_T (as illustrated in Figure 2-6 c and d).

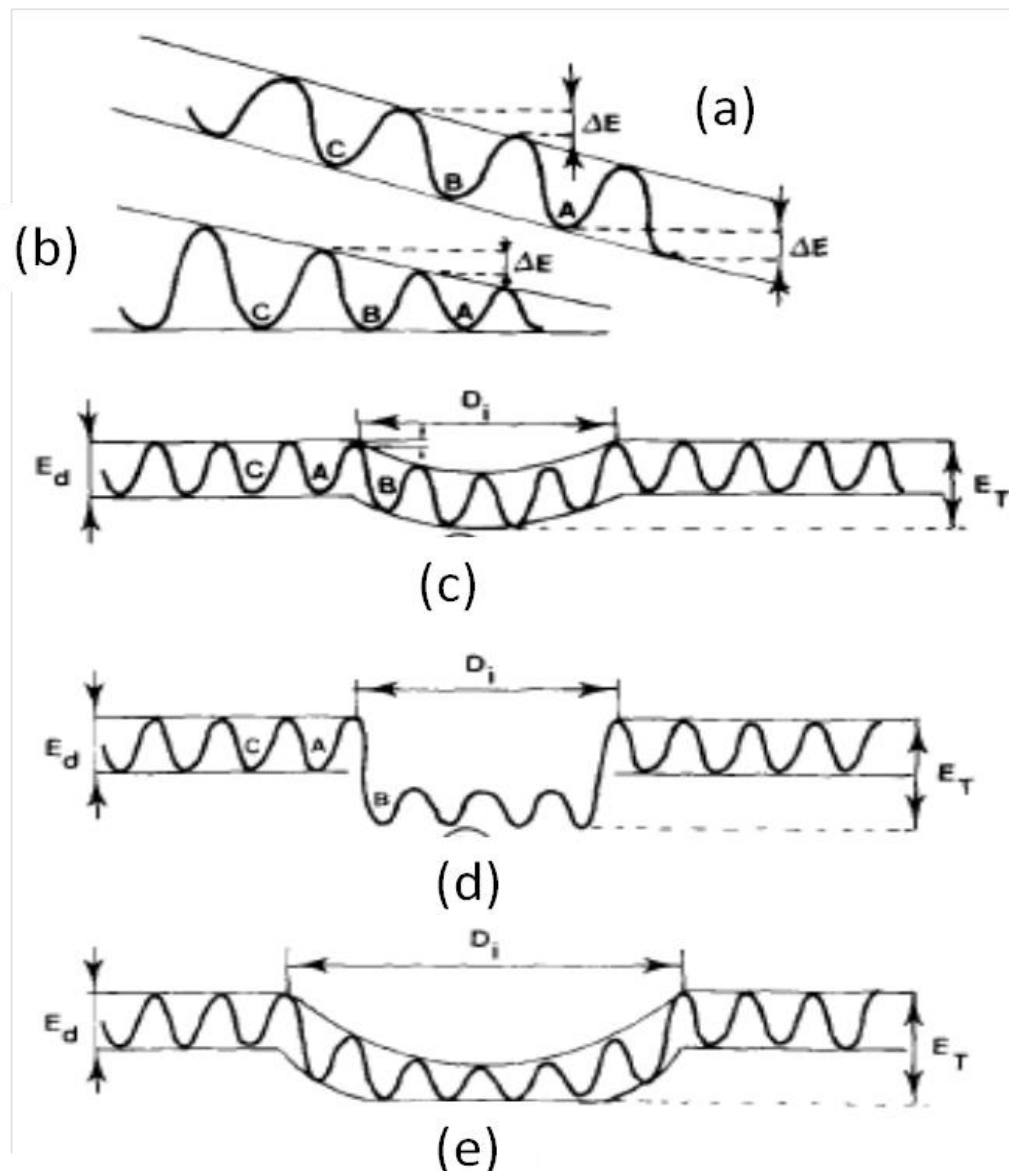


Figure 2-6: Schematic of energy steps necessary to the diffusion of hydrogen atom through a metal lattice in some particular cases: (a) existing attractive force, (b) distorted lattice, (c) attractive trap, (d) physical trap and (e) mixed trap where D_i is the effective size of the trap, E_d is the activation energy for diffusion and E_t is the activation energy of the trap [63]

The reason is that only small, very probable, jump increments are needed to get out of the attractive trap, while a hydrogen atom trapped in a physical trap requires one relatively big jump (perhaps impossible) in order to leave the trap. Therefore, attractive traps are more reversible than physical ones. Since the mean jump increments of a hydrogen atom depend on the temperature, a reversible trap, will release hydrogen continuously at elevated temperatures. On the other end an irreversible trap will release hydrogen only

above a certain temperature at which the thermal energy of the hydrogen atoms is high and consequently, the jump probability of hydrogen atoms outside of the trap is not negligible.

Reversible traps can act as both sink and source of hydrogen since they can take and give hydrogen by definition. At elevated temperatures these traps will be no different than the solute hydrogen. On the other hand, irreversible traps can act only as a sink for hydrogen, given that the service temperature is not high enough for the release of hydrogen from that kind of trap sites.

The reversibility of the trap is determined by its binding energy; traps possessing binding energy higher than 60kJ/mole are defined as irreversible traps, while those with binding energy lower than 60kJ/mole are defined as reversible traps. Irreversible traps due to their high binding energies only capture hydrogen until they become saturated with hydrogen [64]. A summary of the different trap sites with their respective activation energy is presented in Table 2-3.

Table 2-3: Binding energies of various types of hydrogen traps in steels (The data is obtained from thermal desorption analysis method and hydrogen permeation method performed by various researchers) [63,65]

<i>Trap site</i>	Binding energy in kJ/mole
Dislocation elastic stress field	~20
Dislocation core (screw)	20-30
Dislocation core (mixed)	59
Grain boundary	18-20,49,59
Free surface	70,95
Interstitial atom	3-10
Vacancies	38-48
Clusters	57-67
Inclusions	87-96

2.2.3. Thermal desorption spectroscopy for hydrogen trapping characterization

Many studies have been conducted in order to understand the trapping behavior of hydrogen in steel. As tools for investigating potential hydrogen traps, several experimental methods are discussed regarding their potentials to characterize the physical nature of hydrogen traps. These methods include among them the hydrogen permeation technique [26,27,66] and Thermal Desorption Spectroscopy (TDS) or Thermal Desorption Analysis (TDA) by some researchers [27,54,67–76]. TDS is a very effective procedure for the identification of different types of trapping sites and for the measurement and calculation of their binding energy and the trap density. This technique involves heating the sample at a constant heating rate and respectively monitoring the hydrogen degassing rate. A typical thermal desorption spectrum is presented in Figure 2-7. According to a model established by Lee and Lee in the 80's [68], one can calculate the binding energy for trapping of hydrogen by comparing the temperature positions of hydrogen desorption peaks at different heating rates. Since de-trapping and desorption are diffusion-controlled processes, the position (temperature) of the desorption peaks depends on the heating rate. As faster the heating rate the higher is the desorption temperature. From these changes of the peak's temperature as a function of the heating rate one can calculate the trap's binding energy.

In addition, when more peaks are present in the thermal desorption spectrum, one can calculate the trap density of each of the identified traps.

For the case of SMSS, Eliezer et al. conducted a series of examinations in order to categorize the trapping sites present in this material [55]. The trapping sites were characterized according to three different hydrogenation methods: electrochemical charging, gaseous phase charging and introduction of hydrogen through welding with hydrogen in the shielding gas. It was found that all the trapping sites are of reversible type, as the calculated binding energy was <10 kJ/mole.

Moreover, Eliezer et al. found that when hydrogen is introduced through the welding atmosphere, it is more deeply trapped in the material than when introduced by electrochemical charging, although the hydrogen concentration introduced by the latter is about two orders of magnitude larger.

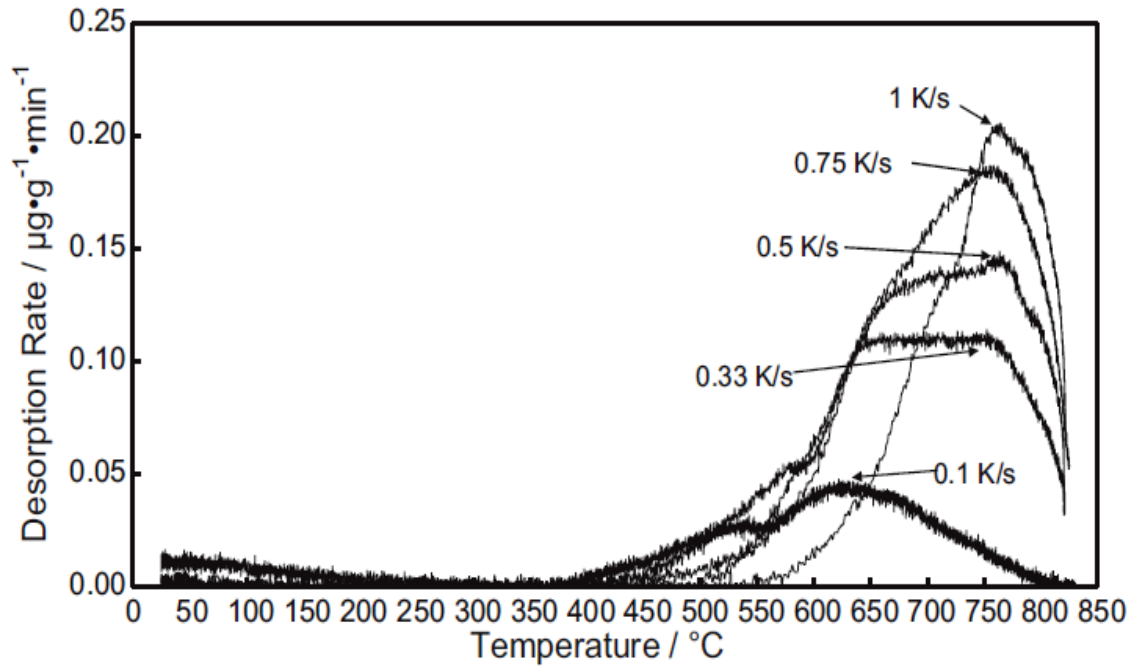


Figure 2-7: Thermal desorption spectrum of a LECO standard sample with a known hydrogen concentration [76]

2.3. Hydrogen transport

The transport of hydrogen from its original location, whether external or internal, to another location within the component where the critical degradation can occur is probably the most complex aspect of the HAC process. Yet, the understanding of this process is crucial for the development of the existent HAC mechanisms and for the predicting of a component life time under hydrogen surrounding [77,78]. The absorption of hydrogen in the component can occur during production (usually welding), processing, and under service conditions (e.g. when corrosion protection is applied). Hydrogen atoms enter into the metal lattice as a single proton which behaves as a screened proton and give away their electron to the metal electron cloud. Immediately after the entry of the hydrogen atoms in the material the diffusion process begins. This process is mostly controlled by the concentration gradient and the chemical potential in the material ($d\mu_{\text{H}}/dx$), as described by the Fick's first law of diffusion. The chemical potential is mainly a combination of the hydrogen concentration gradient and stress concentration in the component. The diffusion of the hydrogen atoms through metallic materials is influenced by the material's crystal structure. The different crystal structures, e.g. BCC and FCC have interstitial sites with different

behavior for foreign atoms such as hydrogen. The FCC structure exhibits relatively large interstitial sites and hence, higher hydrogen solubility. On the other hand, the BCC crystal structure exhibits a less condensed structure (packing factor of 0.63 compared to FCC crystal structure with packing factor of 0.74), which allows faster hydrogen diffusion in the metal lattice (see Figure 2-2). The diffusion coefficients of the BCC crystal structure are usually between 4 or 5 orders of magnitude larger than those of the FCC crystal structure [79].

Hydrogen transport in a metallic material can occur in three different forms: as dislocation atmospheres [80–82], by interstitial jumps in the lattice (lattice diffusion), or along short circuit paths. Hydrogen transport by dislocations movement is much faster than the two others mentioned diffusion forms. This form of transport was suggested by Bastien and Azou in 1951 [80] and a relevant model was developed by Tien et al. after observing a severe loss in ductility of a serving component and yet, a still ductile characterized fracture surface [81]. This form of hydrogen transport takes place when the material is subjected to severe external loading and therefore undergoes plastic deformation, accompanied by enhanced dislocations formation and movement. Under plastic deformation, the dislocation density in the material increases and dislocations are a favorable place for hydrogen atoms, as they possess high density of unbounded chemical connections. Moreover, the presence of hydrogen atmosphere in the dislocation facilitates its movement through interaction with stress fields and obstacles, which will be discussed in Section 2.4.5. For this reason, the transport of hydrogen is facilitated and enhanced during plastic deformation and enhanced dislocations movement [83–86].

Numerous studies have been conducted on Ni and Ni-Cr alloys, proving the enhancement of hydrogen mass transport under the conditions of external loading and consequently induced plastic deformation. The findings of these researches highlighted that hydrogen effective diffusivity increases by approximately 5 orders of magnitude under the combined conditions of plastic deformation during electrochemical cathodic charging [87,88]. These researches also elucidated the reason for the strong dependency of the embrittlement phenomenon on the strain rate of the tensile test. It is apparently due to the dynamic trapping effect of hydrogen at dislocation, of which the density is increased during plastic deformation.

2.3.1. Hydrogen diffusion in SMSS

In order to assess the lifetime of a serving steel component in hydrogen environment, the estimation of the hydrogen transport characteristic in the specific material is of very high importance. The estimation of hydrogen transport behavior in a specific material is a very complicated task, as a number of factors play a role including the lattice diffusion, the crystal structure of the metal, and most importantly, the microstructure characteristics.

In principle, steels possess two main dominant phases; austenite (FCC crystal structure) and ferrite/martensite (BCC/BCT crystal structure). These two structures have different hydrogen diffusion behavior characteristics, for the hydrogen diffusion behavior is specific and different with every steel microstructure, and depends on both the morphology as well as the phase composition. In order to determine the effective diffusion coefficient and diffusion characteristics every type of steel should be examined separately [89–95]. Generally, it is known that the diffusion coefficient of hydrogen in ferritic microstructure is about four to five orders of magnitude larger than that of austenitic microstructure [96]. It was shown that hydrogen diffusion is slower in alloys containing larger content of the austenitic phase. The morphology of the phases also plays an important role. Alloys with continuous ferritic phase (fast diffusion path), such as rolled duplex steel, exhibit higher hydrogen diffusion coefficient than alloys in which the austenitic phase (slow diffusion path) is continuous and blocks the diffusion path in alloys, such as welded duplex steel, where the austenitic phase is distributed along grain boundaries. This formation prevents a continuous morphology of the ferritic phase and thus slows the global hydrogen diffusion in the specific alloy, so that the so-called effective hydrogen diffusion coefficient is reduced [97,98].

A wide review of the influence of different microstructures on hydrogen diffusion characteristics was summarized by Böllinghaus et al. [9,10], and scatter bands for various kinds of steel microstructure were established. This study is a review based on various studies of hydrogen diffusion in steels. An example of the wide range of hydrogen diffusion coefficients for martensitic microstructure can be seen in Figure 2-8, as was measured and calculated by Seeger [99].

Specifically for martensitic structure, the metallurgical condition of the alloy has an important role in the hydrogen transport characteristic. Hydrogen transport in these alloys strongly depends on the dispersivity of the retained austenite particles and the presence of

precipitations (usually chromium carbides) which act as irreversible traps. Dislocations have apparently a secondary role in hydrogen transport characteristic in these alloys [100]. The relatively low content of the austenitic phase allows a continuous morphology of the martensitic phase and consequently the martensitic steels possess higher hydrogen diffusion coefficient than duplex steels which possess higher austenite content. Martensitic steels usually have a lower hydrogen diffusion coefficient than pure ferritic steels since the hydrogen diffuses slower in the martensitic phase and is arrested by the austenitic particles in the martensitic matrix [96].

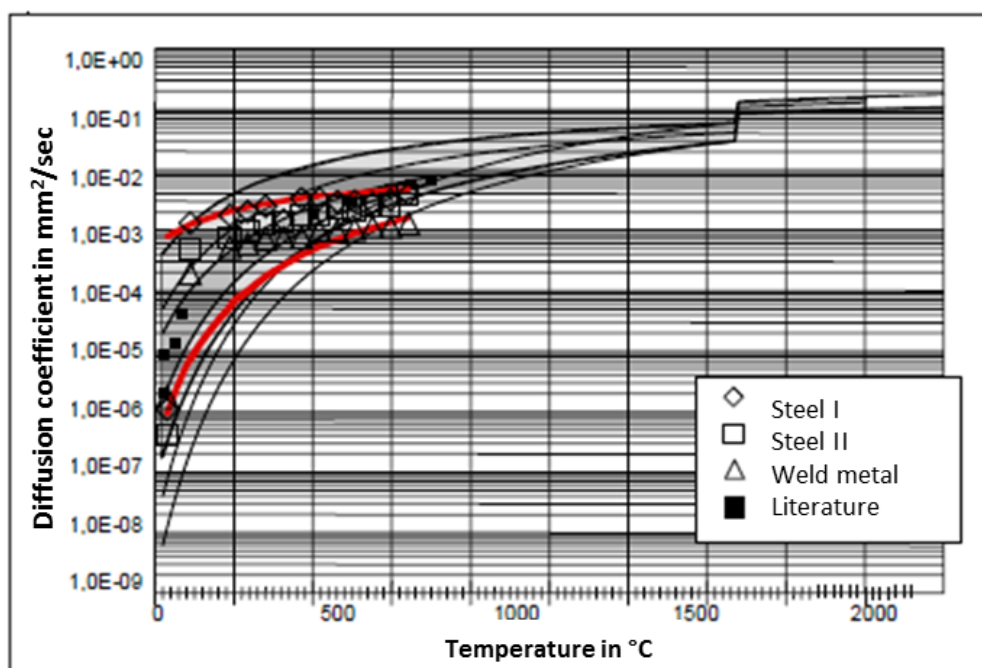


Figure 2-8: Published values of hydrogen diffusion coefficients in two types of SMSS as a function of temperature [99] (the literature values are taken from [9])

2.4. Hydrogen Assisted Cracking (HAC)

HAC is a generic term which is applied for a wide variety of fracture phenomena having in common the presence of hydrogen in the alloy as a solute element or in the surrounding atmosphere as gas [1,101]. Louthan [102] summarized the following cases as a result of HAC: failures of fuel cladding in nuclear reactors, breakage of aircraft components, leakage from gas filled pressure vessels, delayed failure in various high strength steels, reductions in mechanical properties of nuclear materials, and blisters and/or fisheyes in steel parts.

Steels, particularly the high strength stainless steels with the bainitic/martensitic microstructure tend to be susceptible to HAC [103,104]. However, HAC is not specific to high strength steels. Other materials such as titanium, nickel and aluminum can exhibit this phenomenon to some extent as well [105–107].

The aspects of the HAC phenomenon and the micro scale influences of hydrogen on the material will be widely discussed in the following sections.

HAC is mainly referred to as the degradation of the mechanical properties of a given material in the presence of hydrogen. The interaction of the hydrogen adatoms with the metal lattice causes degradation in mechanical properties, especially ductility, and consequently leading to early failure at stress levels lower than the yield strength of the metal.

HAC is a complicated process which makes the forecast of the component reliability nearly impossible to establish. Consequently it requires a real-life testing procedures prior to the application in order to assure the material's compatibility for the application. In spite of numerous studies of this phenomenon, the mechanisms of HAC are not yet completely understood. There are many factors that influence the form and the severity of the process. The exact mechanism which causes embrittlement is dependent upon factors such as hydrogen transport characteristic (mainly diffusion behavior and trapping), on the amount of available hydrogen (namely diffusible hydrogen), and on the susceptibility of the material to HAC. These factors are derived from factors such as microstructure, alloying elements, applied and residual stresses, service temperature etc. [108].

In order to explain the HAC phenomenon, a variety of mechanisms and theories have been proposed and established in the course of the study of this phenomenon over the last century. However, there are still controversies and disagreements about the dominant failure mechanism and its dynamics. It is claimed by Hirth [109] that the degradation of the mechanical and physical properties of steels due to hydrogen presence is a complex process which involves many of the existent embrittlement mechanisms. Generally speaking no single mechanism of the existent suggested mechanisms is applicable to all of the materials, microstructures and hydrogen environments. Rather, each individual case has its own circumstances and mechanism of failure. Within a given system, depending on the hydrogen source and whether it is an electrochemical source or due to welding, the

embrittlement mechanism can be alternated. In the following sections the suggested embrittlement mechanisms will be presented and discussed in detail.

2.4.1. The pressure theory

The pressure theory is very likely to be the first theory trying to explain the HAC phenomenon. It was first suggested by Zapffe and Sims in the early 1940's, and they termed the phenomenon "The Planar Pressure Theory" [110]. This theory was further developed by Petch and Stables [111], which discussed a delayed fracture of materials under static load due to absorption of gas on the crack's surface. The pressure theory is based on the assumption that hydrogen adatoms possess a lower chemical potential at lattice defects and as a result are attracted to microstructural defects (e.g. grain and phase boundaries, pores, non-metallic inclusions, dislocations etc.) and recombine there to create hydrogen gas molecules (H_2). This happens, when hydrogen is electrochemically introduced into the material, and thus it reaches a state of extreme supersaturation due to effective hydrogen external pressure of >1000 atmospheres. Since the hydrogen molecules possess a significantly larger volume than the hydrogen adatoms, the formation of these molecules induce a severe high pressure within the material [110]. As this pressure exceeds the yield strength of the material, it is believed that an initiation of a crack and/or a blister can occur even in the absence of external applied stress. This effect, combined with internal hydrogen gas stresses and external applied stress, might lead to catastrophic consequences [112].

In Figure 2-9 the pressure development is illustrated as hydrogen recombines at impurities and defects in the material's microstructure and inducing blisters. A realistic example of hydrogen blistering, hence cracking induced by hydrogen recombination at defects, can be seen after electrochemical cathodic charging of a technical ARMCO iron specimen (Figure 2-10).

The pressure theory supplies an explanation for the origin of the stresses that induces the initiation of cracks and/or blisters. However, this theory applies only for cases of extreme supersaturation of hydrogen in the metal's lattice. In most cases of HAC the hydrogen concentration in the component was well below the solubility limit of the material. Thus, this theory is not adequate with the majority of HAC failure cases.

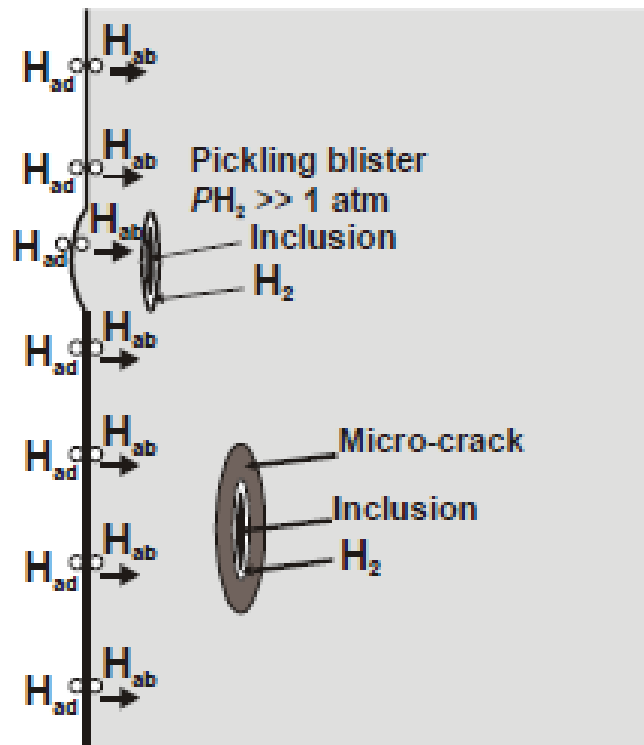


Figure 2-9: Illustration of the principles of the pressure theory: It describes the formation of hydrogen molecules in microstructural defects [50,113]

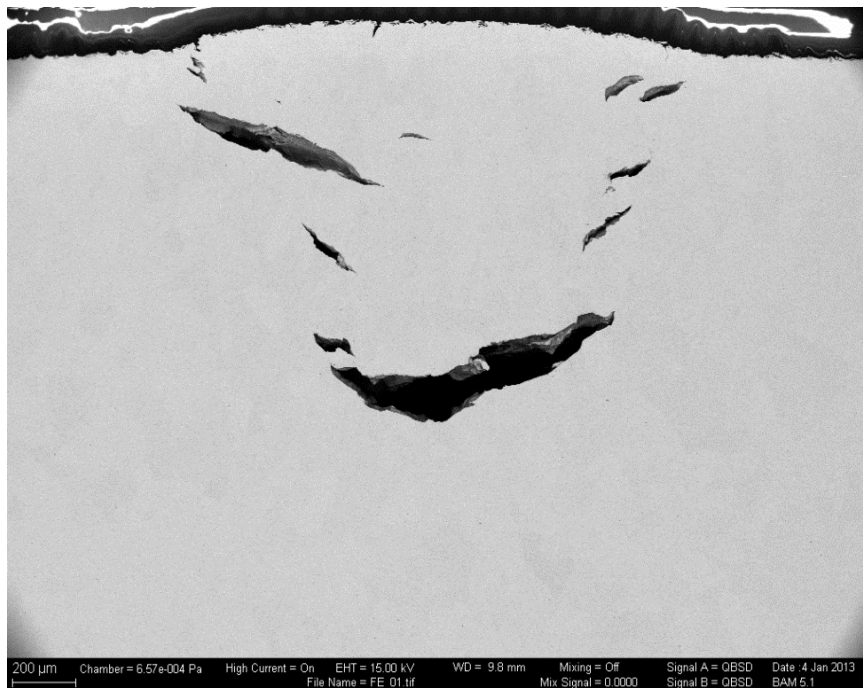


Figure 2-10: A cross section of hydrogen induced blister after electrochemical cathodic charging in technical iron of ARMCO grade. The formation of this blister is described in detail in [114]

The mechanisms that describe the degradation of the mechanical properties and thus the nature of the crack and the crack's surface morphology will be described and discussed in detail in the following sections.

2.4.2. The absorption model

The model of absorption, suggested by Uhlig [115] and by Petch [116], corresponds to HAC in the process of stress corrosion cracking and it is advocated to hydrogen-liquid embrittlement (referred to as "Stress Sorption Cracking"). According to this theory, absorption of hydrogen ions reduces the surface energy term in both Griffith and Petch-Stroh equations, thus leading to lower stress failure, as illustrated in Figure 2-11. The solute hydrogen interacts with the strained bond at the tip of a crack and reduces the bond strength [117].

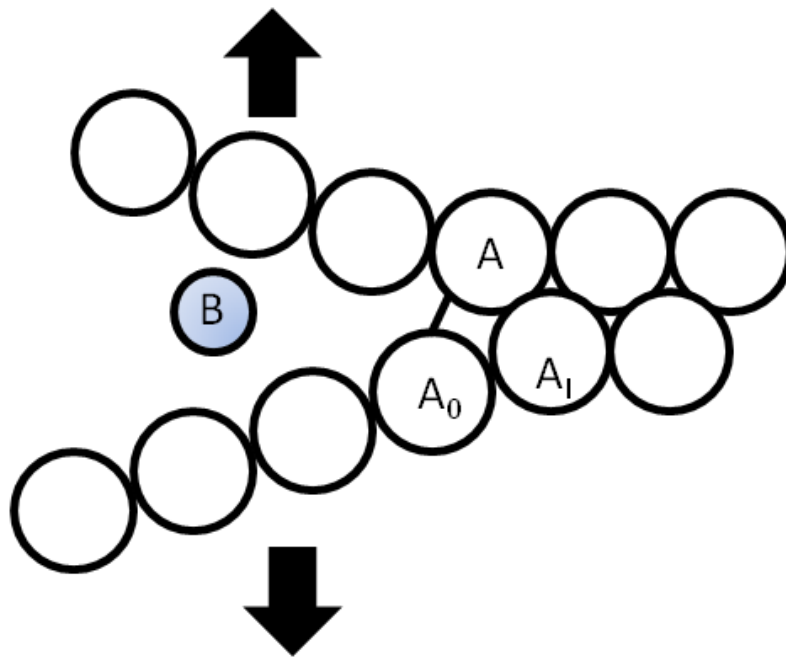


Figure 2-11: Schematic illustration of the absorption mechanism: hydrogen ion from the environment *B*, interacts and reduces the cohesive strength of strained bond *A-A₀* at the tip of a crack (redrawn from Pugh [117])

The effect of the absorption model is expressed by the Griffith criterion for crack propagation. The Griffith criterion relates the surface energy with the theoretical stress for brittle fracture and is introduced in Equation 2-2.

$$(2-2) \quad \sigma_f = \sqrt{\frac{2\gamma E}{\pi c(1-\nu)}}$$

Where σ_f is the theoretical stress, E is the young modulus, γ is the free surface energy, c is half of the crack length and ν is the Poisson's ratio.

Therefore, the absorption of hydrogen atoms on the metal surface, decrease the surface energy, thus decreasing the theoretical stress required for the crack's propagation [116]. However, this model does not take into account the influence of the energy for plastic deformation included in the effective surface energy. The energy for plastic deformation controls almost entirely the effective surface energy for fracture, thus the changes of surface energy induced by absorption of hydrogen is almost insignificant [14]. However, this model does not explain the reason why surface free energy reduction due to the adsorption of oxygen (or any other gaseous elements) does not inflict the same deleterious effect as hydrogen inflicts.

Despite its disadvantages, this theory is suitable with the mechanism of crack propagation in high-strength stainless steels, most probably due to the inferior ductility of these alloys [118].

2.4.3. Embrittlement caused by hydride formation

In some metals the formation of the intermetallic hydride phase is considered to be the main cause for HAC. This mechanism was first proposed by Westlake in 1969 [119], and was well established by numerous experimental and theoretical support. Titanium alloys make a good example for this kind of embrittlement mechanism [7,105,120–122], as hydrogen induced cracks tend to initiate at the sites of hydride formation (see Figure 2-12).

Among the systems which have been clearly shown to exhibit hydride formation embrittlement are the groups IV and V transition metals (e.g. Ti, Zr, Nb, V and Ta) and their alloys, which exhibit a strong thermodynamic force for the formation of hydrides [123]. In the case of Zr alloys, a direct observation of hydrides in the front of crack's tip were made by Cann and Sexton in 1980 using TEM [124].



Figure 2-12: Hydrogen induced cracks along the α phase boundaries in duplex Ti alloy, in the areas where hydride tend to form [120]

This mechanism is characterized and described by the following steps: (i) hydrogen diffusion to regions of high hydrostatic stress ahead of a crack, (ii) nucleation and growth of a hydride phase, (iii) cleavage of the hydride when it reaches a critical size (iv) and crack arrest at the hydride- matrix interface (see Figure 2-13)

The hydride phases in a metallic material can be classified into four different groups: (i) ionic hydrides that have salt-like characteristic, (ii) transition hydrides, (iii) intermediate hydrides and (iv) covalent hydrides [1]. These hydrides are formed from extremely high hydrogen fugacity, which usually develops in electrochemical processes such as cathodic protection, electroplating etc. The type of hydrides that is relevant to the HAC process is transition hydrides. These usually form in metals with relatively low hydrogen solubility. The embrittlement of metals by the presence of hydrides can occur because of the large volume difference between the hydride and the metallic lattice. This difference in volume leads to the development of high elastic stresses around the formed hydride. Hydrides are usually precipitate at dislocations and their presence enhances the dislocation movement and the deformation mechanism of the component. Hydrides precipitate at the head of a crack tip and at the area of stress concentration. Since hydrides are usually more brittle than metal, their formation eases the crack propagation in the matrix.

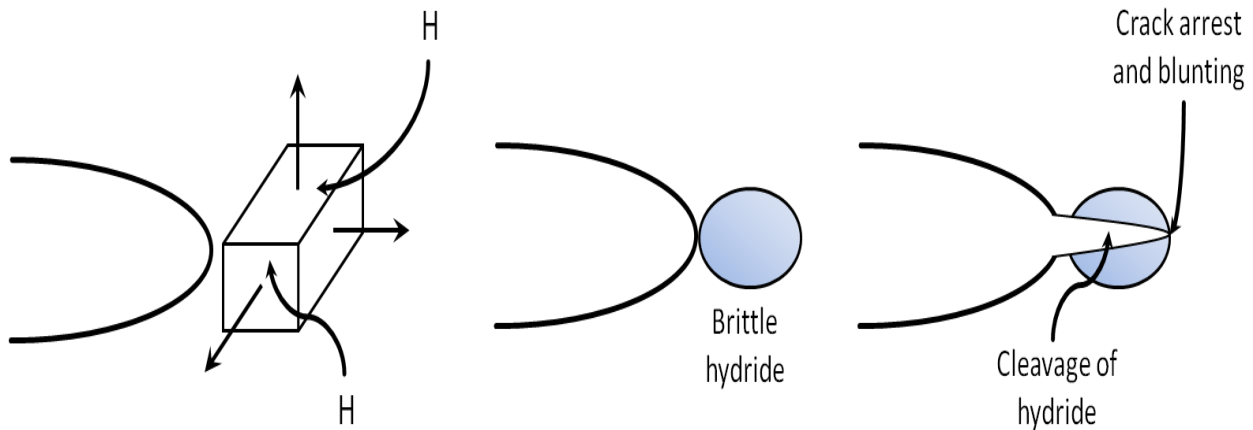


Figure 2-13: Schematic diagram illustrating subcritical crack growth involving hydrogen diffusion to hydrostatically stressed regions, then formation and fracture of a brittle hydride at a crack tip (redrawn from Lynch [125])

The hydride formation theory is acceptable for most of the materials that tend to form metal hydrides when hydrogen is present. In the case of non-hydride forming materials, such as steels and among them SMSS, the situation is far less simple. Currently, there are two main and competing proposed mechanisms of HE in non-hydride forming materials. These mechanisms are discussed in detail in the following sections.

2.4.4. Hydrogen Enhanced Decohesion Theory (HEDE)

The de-cohesion model is based on the theory introduced by Troiano et al. in 1955 and 1960 [126,127], and further supported and developed by the work of Oriani [3,128,129] and others [130,131]. It is suggested that solute hydrogen in metals decreases the cohesive strength of the cubic cleavage planes, due to the filling of the d bands of the metals by the electrons of hydrogen atoms. This filling of the d bands induces an increase of the inter-atomic spacing thus decreasing the cohesive force between the atomic planes. The weakening of the metal-metal bonds by the hydrogen presence leads to a preferential occurrence of tensile separation of atomic planes instead of slip, as illustrated in Figure 2-14.

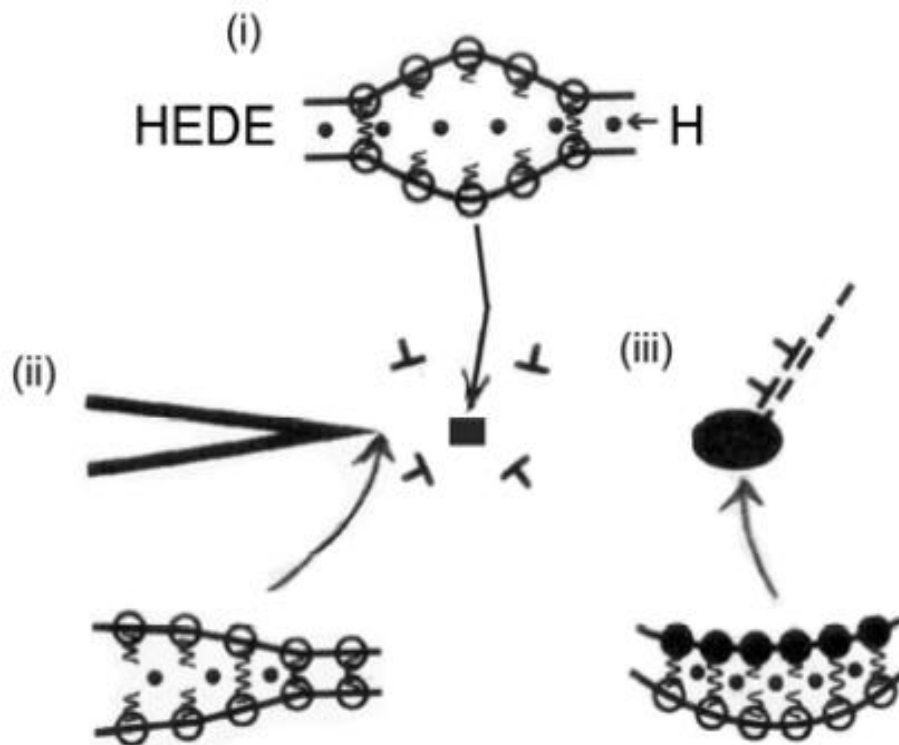


Figure 2-14: HEDE mechanism, involving separation of atomic planes due to the weakening of the interatomic bonding by (i) solute hydrogen, (ii) absorbed hydrogen and (iii) hydrogen at particle-matrix interfaces [132]

The presence of tri-axial tensile stresses at the tip of a crack induces a decrease of the chemical potential of hydrogen in the vicinity of the crack tip, thus stimulating hydrogen to diffuse toward the crack. The increase in hydrogen concentration at the crack tip induces more stress concentration in this region. Once the hydrogen concentration exceeds the critical concentration, the crack will propagate due to the synergetic effect of the decrease of the cohesive force combined with the increase of the local stress. The crack propagation will stop once the crack advances out of the region of hydrogen accumulation, where it becomes arrested by plastic deformation. When the propagation is stopped, the process repeats itself again ultimately leading to discontinuous propagation, which in most cases is characterized by cleavage like surface morphology.

Oriani has modified the De-cohesion model with respect to the magnitude of the elastic stresses, which are necessary to produce sufficient hydrogen accumulation, to the location of the crack nucleation sites. In contrast to the model of Troiano, Oriani considered the crack propagation to be continuous and as a result, is faced with the problem of explaining how a brittle crack can propagate at low velocities without being arrested by plastic deformation [128,129].

Direct experimental evidence for the HEDE mechanism is impossible to obtain, and it can only be supported theoretically. For example, quantum-mechanical calculations suggest that hydrogen weakens interatomic bond strength by reducing the electron charge density between the atoms, particularly at grain boundaries [133]. Lee and Unger [131] also developed this model using numeric simulation and showed that crack propagation and failure occur at realistic stress conditions when considering the reduction of the cohesive forces between the iron atoms in the presence of hydrogen.

2.4.5. Hydrogen Enhanced Localized Plasticity (HELP)

It was first observed by Beachem in 1972 that hydrogen eases the dislocations motion and generation in steels. This model is based on localized softening due to solute hydrogen, or more specifically, the presence of hydrogen atmospheres around both mobile dislocations and obstacles to dislocations movement in the vicinity of the head of a crack [134]. It is suggested that these atmospheres can reconfigure themselves rapidly in response to changes in the elastic stress fields, such that the total elastic energy is minimized when dislocations approach obstacles. The resistance to dislocation motion due to the obstacles is therefore decreased, and dislocations velocities are increased. The hydrogen is concentrated in the vicinity of the crack's tip due to hydrostatic stresses or entry of hydrogen at crack tip and thus, deformation is facilitated locally near crack tips. Therefore a dimples fracture surface or quasi cleavage cracking with tear ridges are to be expected when the HELP mechanism occurs [5,96,132]. An illustration of the basic principles of the HELP mechanism is given in Figure 2-15.

This theory was supported later in the early 1980's by Birnbaum, Sofronis, Sirois and Robertson [5,121,135]. In order to explain the effect of hydrogen on dislocation mobility, Sirois, Sofronis and Birnbaum proposed a mechanism in which hydrogen concentrates and forms hydrogen atmospheres around dislocations and other elastic stress centers. The redistribution of the hydrogen atmospheres around the dislocations effectively shields the dislocation from the elastic stress field of an obstacle and thus reduces the interaction energy between the dislocation and the obstacle. Consequently, dislocations movement requires less energy and dislocations can move at lower levels of applied stress [5,84]. In the late 1990's, Robertson proved the enhanced mobility of dislocations in the presence of hydrogen using Transmission Electron Microscopy (TEM). The examined samples were in-

situ deformed within a controlled environment; once in a vacuum surrounding and second, in a hydrogen gas atmosphere [86,135]. The TEM observations showed clearly an enhancement of the dislocation's mobility when hydrogen was in the surrounding atmosphere. This influence of hydrogen and the enhanced mobility of the present dislocations are presented in Figure 2-16 and Figure 2-17.

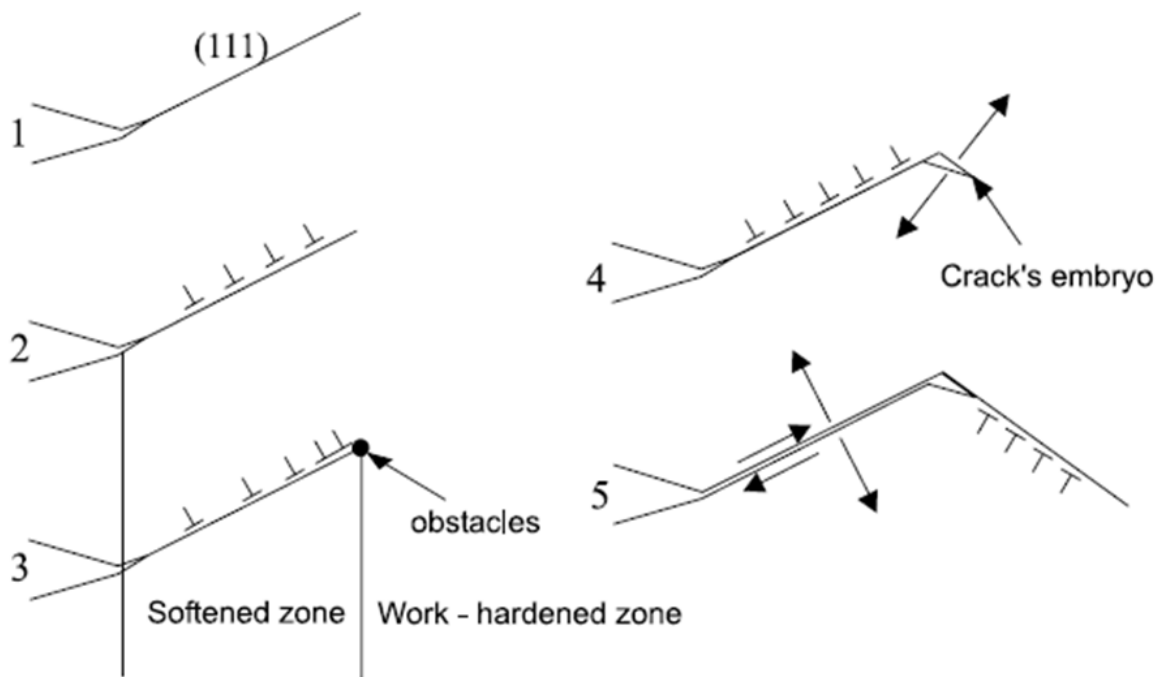


Figure 2-15: Steps in hydrogen enhanced local plasticity, HELP: (1) Slip planes activated at the crack tip, (2) enhanced plasticity on (111) planes due to hydrogen absorption, (3) pile up of dislocations near obstacle, (4) initiation of crack or micro void due to the local stress increase and (5) crack opens by shear De-cohesion along the slip plane [136]

Due to the enhanced plasticity effect described by this model, most of the cracks are characterized with ductile fracture surface such as Microvoid Coalescence (MVC) and/or the presence of dimples. The fracture according to this model is usually characterized as a transgranular crack, but intergranular cracks due to HELP can also appear when hydrogen is concentrated at the grain boundaries.

For HAC cases of fracture surface having a cleavage-like characteristic, there is no satisfactory explanation regarding the HELP theory. This theory therefore does not apply to these cases.

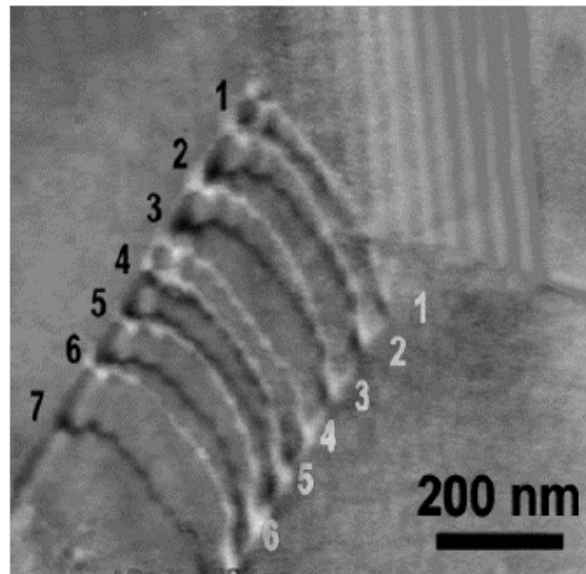


Figure 2-16: The influence of 90 torr hydrogen gas on dislocation configuration. The white dislocations show the position with hydrogen and the black dislocation show the initial position [137]

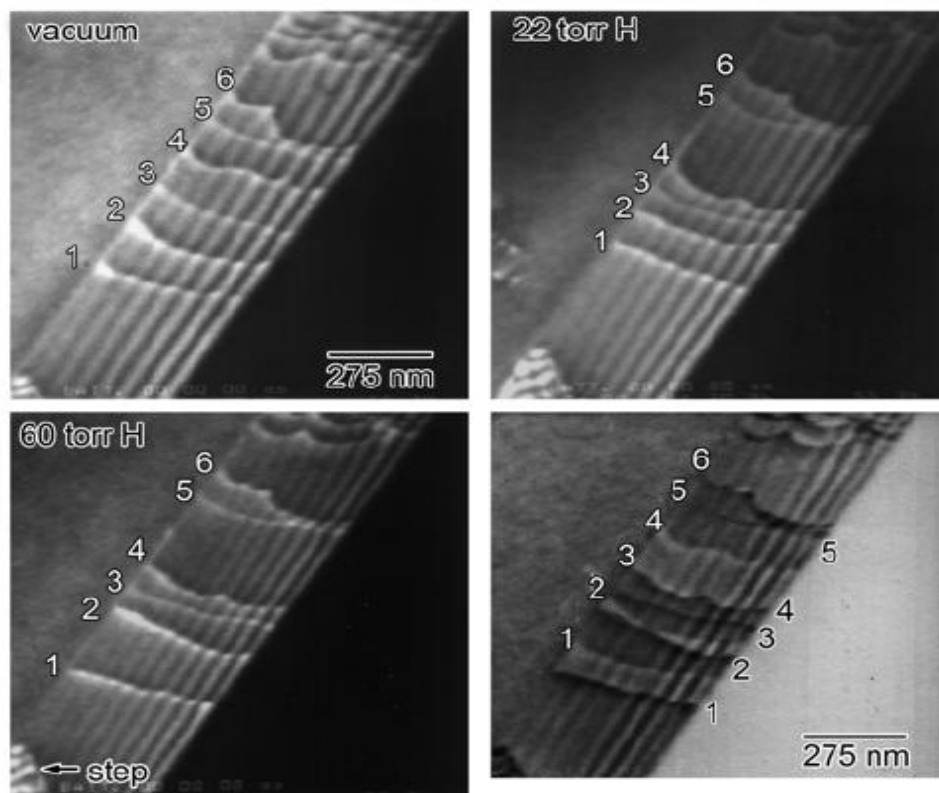


Figure 2-17: Effect of introducing hydrogen into the controlled environment transmission electron microscope and hence into 310S stainless steel on the motion of extrinsic dislocations in a grain boundary [86] . The introduced hydrogen atmosphere pressure is stated in the images. The last image is a combination of the first and the third images

2.4.6. Adsorption induced Dislocation Emission (AIDE)

The AIDE mechanism is in principle the combination of some basic principles of the HELP and the HEDE mechanisms. This mechanism was first suggested by Lynch in the mid 1980's [138–140] after comparing fracture surfaces in various liquid environments and gaseous hydrogen environment. He compared the "brittle" inter-granular and trans-granular cleavage-like fracture surfaces of metal specimens tested in both environments. The fracture surfaces of the gaseous hydrogen embrittled surfaces showed evidence of slip, dimples and tear ridges. These features are all evidence of an enhanced dislocation activity and led Lynch to propose that crack growth occurred by localized plastic flow in hydrogen embrittlement [112,141]. It was suggested that adsorbed atoms, i.e. hydrogen atoms located on the surface and in between a few atomic layers in the vicinity of a crack's tip, weaken the interatomic bonds and facilitate the formation and emission of dislocations.

The stresses required for dislocation emission are high enough for the enhancement of the general dislocation activity in the plastic zone ahead of cracks. This results in the formation of small voids at particles or at slip-band intersections. Thus, crack growth occurs mostly by dislocation emission. However, dislocation egress at crack tips and void formation ahead of cracks also contribute. Void formation ahead of cracks also assists to maintain small crack-tip radii and small crack-tip-opening angles.

To understand why facilitating dislocation emission from crack tips results in 'embrittlement', it is necessary to consider how crack growth occurs in inert environments for ductile materials. Ductile crack growth appears to occur predominantly by dislocations nucleated from sources in the plastic zone ahead of crack tips regressing at the crack-tip surface, with little or no emission of dislocations occurring from crack tips. Only a small amount of dislocations emanating from near-crack-tip sources would exactly intersect crack tips to produce crack advance – most would produce only blunting or contribute to the strain ahead of cracks. Large strains ahead of cracks are therefore needed to produce crack growth by MVC and deep dimples, with smaller dimples within them, are produced on fracture surfaces. The small dimples within large dimples arise because coalescence of large voids (nucleated from large particles) involves nucleation and growth of smaller voids (nucleated from smaller particles or other sites at higher strains) between large voids [125].

When hydrogen adsorption promotes dislocation emission from crack-tips, a larger amount of the dislocation activity results in crack growth since dislocation emission on

suitably inclined slip planes, produces crack advance as well as crack opening. Thus, coalescence of cracks with voids occurs at lower strains and shallower dimples are produced on fracture surfaces when AIDE occurs (Figure 2-18).

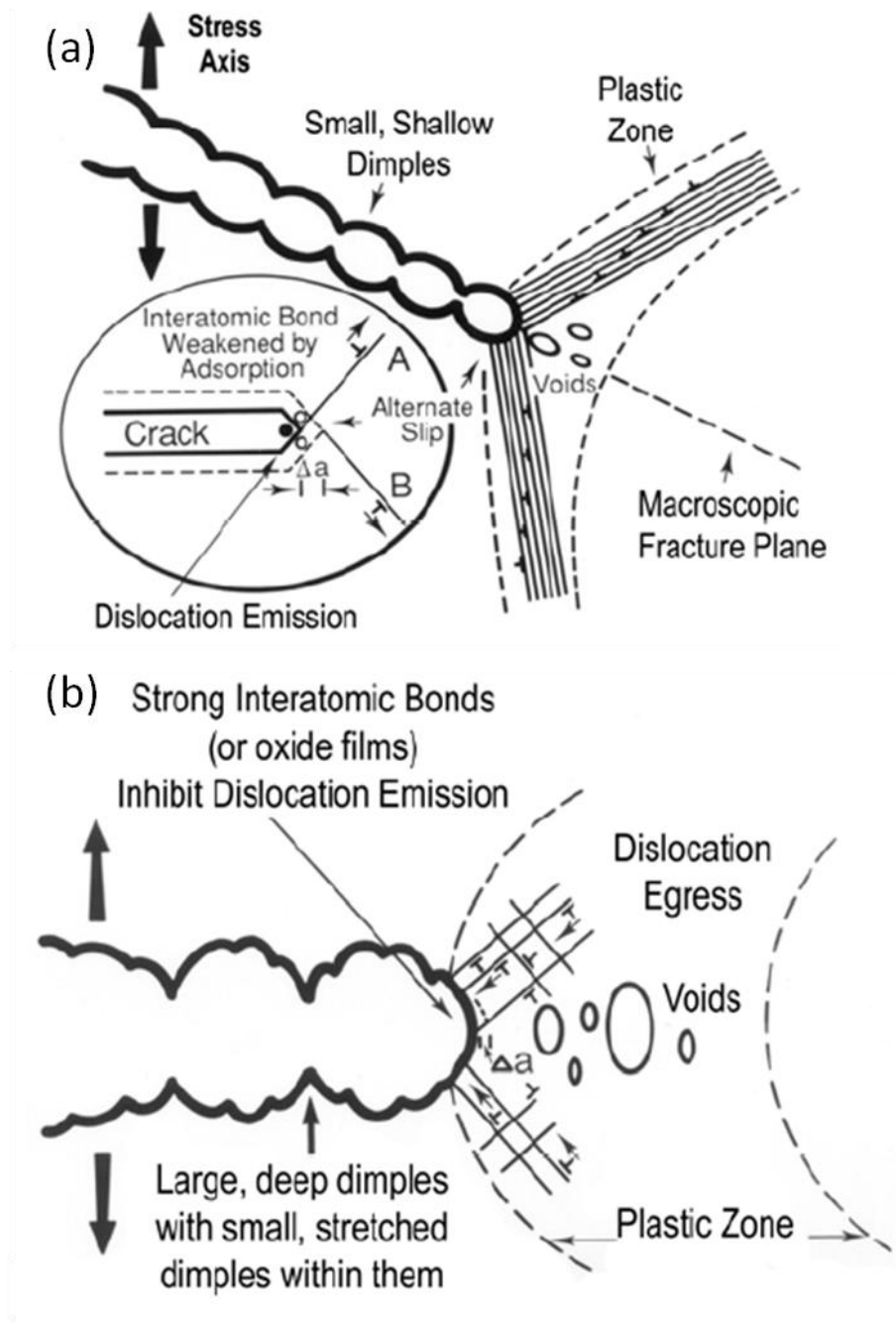


Figure 2-18: Schematic diagrams illustrating (a) the adsorption induced dislocation emission (AIDE) mechanism for transgranular crack growth, which involves alternate-slip from crack tips facilitating coalescence of cracks with voids formed in the plastic zone ahead of cracks, and (b) ductile crack growth involving coalescence of cracks with voids by egress of dislocations nucleated from near-crack-tip sources [142]

The dimples resulting from an AIDE/MVC process also appear to be smaller than those produced by ductile fracture since, for the latter, small dimples within large dimples are often stretched and difficult to resolve.

Crack paths produced as a result of the AIDE mechanism could be intergranular or transgranular depending on where dislocation emission and void formation occurred most easily. For transgranular cracking, alternate slip on planes on either side of cracks would tend to occur in order to minimize the back-stress from previously emitted dislocations. Macroscopic planes for transgranular cracking would therefore bisect the angle between the slip planes, and crack fronts would lie along the line of intersection of crack planes and slip planes. However, deviations from low-index planes and directions would occur if unequal amounts of slip occurred on either side of cracks owing to large differences in shear stresses on the different slip planes. Deviations of fracture planes away from low-index planes could also occur depending on the locations of void nuclei ahead of cracks [125,132].

Barnoush and Vehoff were able to prove later by using the nanoindentation technique that hydrogen presence in a metal crystal reduces the necessary stress for dislocation nucleation, which is named the “pop-in load”. This is allowed by reduction of the shear modulus, dislocation line energy and stacking fault energy [143–145]. These observations are a strong support for the occurrence and interaction of the HEDE and HELP mechanisms.

2.5. Effect of hydrogen trapping on HAC

As described in a former section (Section 2.2.2), hydrogen interacts with defects in the metal lattice (traps). This interaction, namely hydrogen trapping, can affect the nature, extent and kinetics of the HAC process.

Pressouyre [146,147] claims that the susceptibility of any given material to HAC is directly related to the characteristic of its trap population. In particular, reversible traps which can act both as sink or source of hydrogen. Generally, the main role of the traps in the embrittlement process is their ability to induce or suppress the formation of hydrogen enriched regions by affecting the hydrogen transport characteristics. Traps, both reversible and irreversible generally reduce the diffusion coefficient of hydrogen in the material and

consequently suppressing the formation of hydrogen enriched regions. However, irreversible traps with their large hydrogen capacity promote hydrogen concentration centers and since stress fields also tend to concentrate in the vicinity of defects, their presence might increase the material susceptibility to HAC [148].

The trap theory of HAC describes various situations where the influence of three major factors is playing a crucial role: the means by which hydrogen ingresses into the sample and diffuse inside of it (i.e. dislocations, interstitial diffusion, high diffusivity paths), the location of the hydrogen prior to the test (i.e. internal hydrogen vs. external hydrogen), and the character of the trap sites in the material (reversible or irreversible, saturable or unsaturable). The extent and the type of embrittlement will be determined according to the combination of these three parameters [59].

The role of the reversible traps is also determined by these parameters. When hydrogen origin is external to the material and if the initial hydrogen concentration carried by dislocation is constant then all traps are hydrogen sinks. However, if the initial concentration of hydrogen in a certain dislocation decreases with the number of dislocations, the reversible traps will act as sources. When the material is previously charged and hydrogen moves with dislocations, all reversible traps act as sources. The two cases of hydrogen transport by dislocations are illustrated in Figure 2-19.

Generally, the material is more susceptible to HAC when reversible traps act as hydrogen sources, and hydrogen is transported by dislocation. The reason is that hydrogen sources charge the dislocations while moving and the dislocation reaches the flaw (i.e. crack tip) with more hydrogen. Consequently more hydrogen is introduced to the flaw [146].

When hydrogen is external and diffuses by interstitial jumps in the lattice, reversible traps act as sources although with more difficulty to deliver the hydrogen than in the transport by dislocation case. Cracking will occur in regions where the critical concentration is first reached. The critical concentration is the minimum hydrogen concentration in a certain trap which will induce the initiation of a crack. The critical concentration corresponds to a sufficient hydrogen pressure and/or sufficient applied stresses to overcome the cohesive strength (which is lowered due to the presence of hydrogen). This phenomenon was verified experimentally by testing different Fe-Ti alloys containing different amount of Ti. These alloys contain different amount of TiC particles which act as a hydrogen trap. The experimental results showed a solid relation between the nature of the traps ;either they

decrease the time to reach the critical concentration, or they disperse the hydrogen in the material in such a way that the critical concentration could not be reached [147].

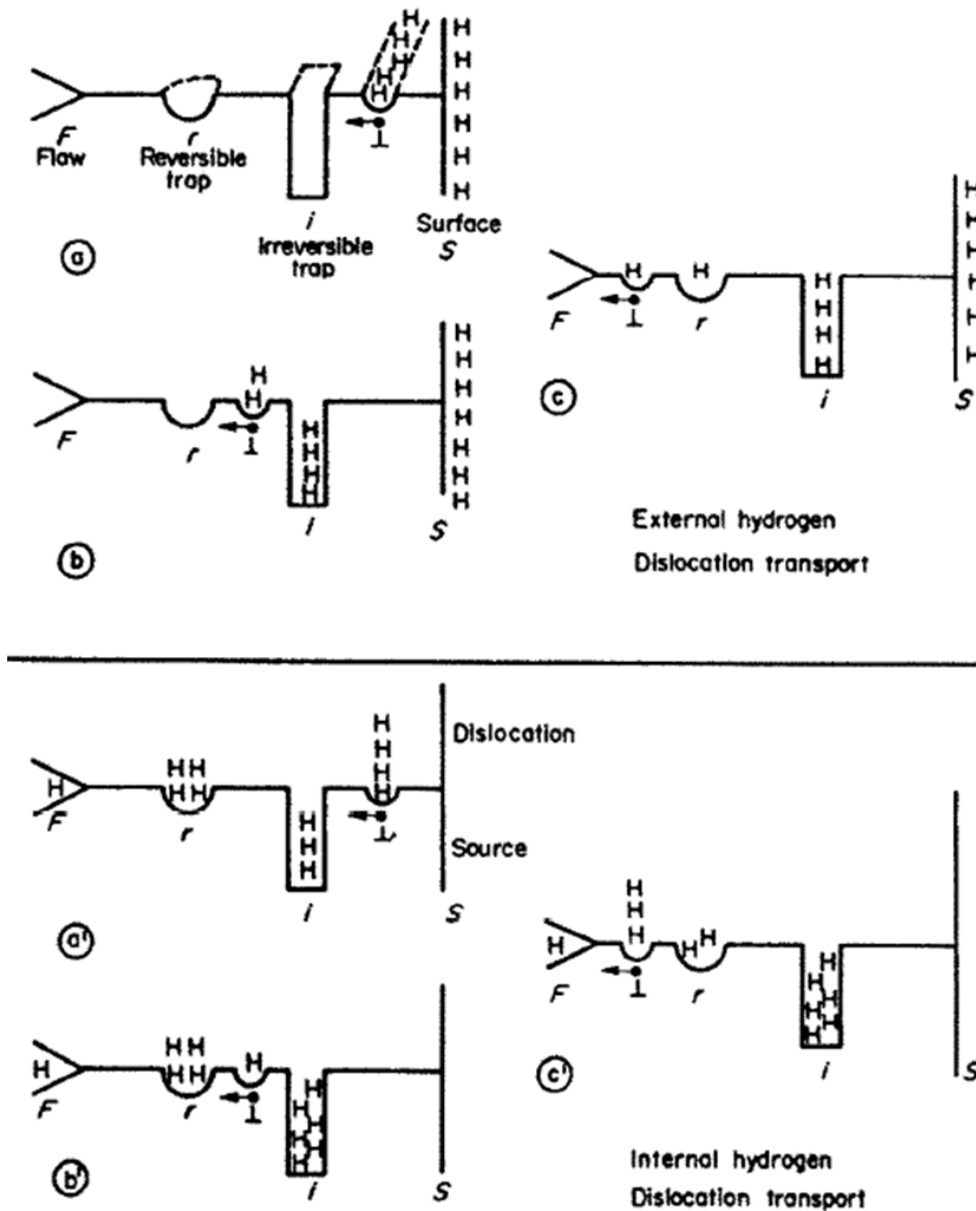


Figure 2-19: (a, b, c) External hydrogen atmosphere and transport by dislocation (a) the dislocation just nucleated at the surface has picked up hydrogen and moves toward the flaw. (b) On passing over an irreversible trap some hydrogen is lost (c) some more hydrogen is lost by the reversible trap. Thus the flaw sees less hydrogen coming in (a', b', c') material precharged and transport by dislocations. (a) hydrogen is distributed over all of the traps when the dislocation begin to move. (b) some hydrogen is lost on the irreversible trap (c) the dislocation recharge itself upon passing a reversible trap. Thus the flaw will see more hydrogen coming in [146]

2.6. HAC of SMSS and of SMSS in flowlines

SMSS are being applied since 1997 to pipelines among the others by Norwegian companies in the North Sea oil and gas fields. Since this application of the steel serves in a sour environment containing H_2S , there were some different failures that were correlated to HAC [14,23,29].



Figure 2-20: Failures in the Tune pipeline that occurred due to HAC. The right side photos present failure of the weld due to hydrogen absorbed during welding process. The left side photos present failure induced after the reparation and coating process. Hydrogen was introduced through gaps in the coating and the cathodic protection that was applied to the flowline [23]

A particular case of HAC of SMSS flowline occurred in Norway at the Tune gas field [23]. The cracks that were categorized as HAC occurred after installation and were attributed to hydrogen that was introduced through the welding process. The source of this hydrogen was related to high values of moisture in the shielding gas (of about 400 ppm H_2O) and high hydrogen concentration in the filler material (about 9-11 wt. ppm H) [22]. This problem was repaired by using annealed filler material and this reduced the hydrogen concentration in the weld down to 2-3 wt. ppm. After the final repair of the flowline some further leaks were detected. These leaks were originated in gaps of the coating that allowed

hydrogen ingress in the pipeline through the cathodic protection and combined with the present stresses the respected failure occurred. The cracking attributed to HAC can be seen in Figure 2-20. After the third failure case in 2002 the SMSS flowlines were scraped and were replaced by Cr-Mn steel flowlines.

It should be mentioned that those failures occurred during the test phase of the flowline and not during service and thus, not causing any environmental catastrophe.

In further investigations, Böllinghaus et al. proved the susceptibility of the modified SMSS used for this kind of applications by introducing different amounts of hydrogen into tensile specimens and testing the mechanical properties changes due to hydrogen [149]. It was found that increased hydrogen concentration significantly reduces the ductility of the tested SMSS, as shown in Figure 2-21 for the case of electrochemical hydrogenation. Furthermore, the fracture surface was alternated from ductile MVC to trans- and intergranular brittle fracture surface with increased hydrogen concentration in the tested samples.

Böllinghaus et al. conducted further experiments in order to assess the susceptibility of the steel to HAC in the as received and in the welded form [150]. It was shown that the low alloyed steels exhibit higher susceptibility after welding to HAC as opposed to the high alloyed grades (with around 6.5 wt.-% Ni and 2.55 wt.-% Mo), which possess the superior ability for creating a passivation layer.

In order to be able to test the susceptibility of the steel weld to HAC in realistic conditions Böllinghaus et al. developed a full scale cold cracking test that simulates the multi axial stress distribution caused by welding [151]. This kind of test provides the ability to predict the failure of a welded pipeline as the service conditions, environmental as well as mechanical, are fully reproduced. By applying this test it was found that the initiation of HAC occurs in the hardened HAZ very close to the fusion line of the welding nut (see Figure 2-22). This is due to quenched martensite in the HAZ which is known to be susceptible to HAC [152].

Hydrogen behavior in SMSS is generally characterized with ease of transport, which means high diffusivity and low solubility through the high content of BCT phase and low content of FCC phase. These conditions enable hydrogen supersaturation of the material when it is subjected to cathodic reactions.

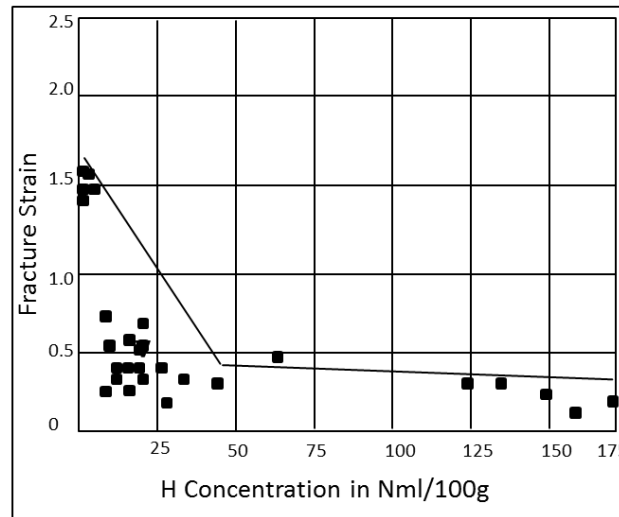


Figure 2-21: The changes of the real fracture strain due to hydrogen in SMSS (reconstructed from Böllinghaus [149])

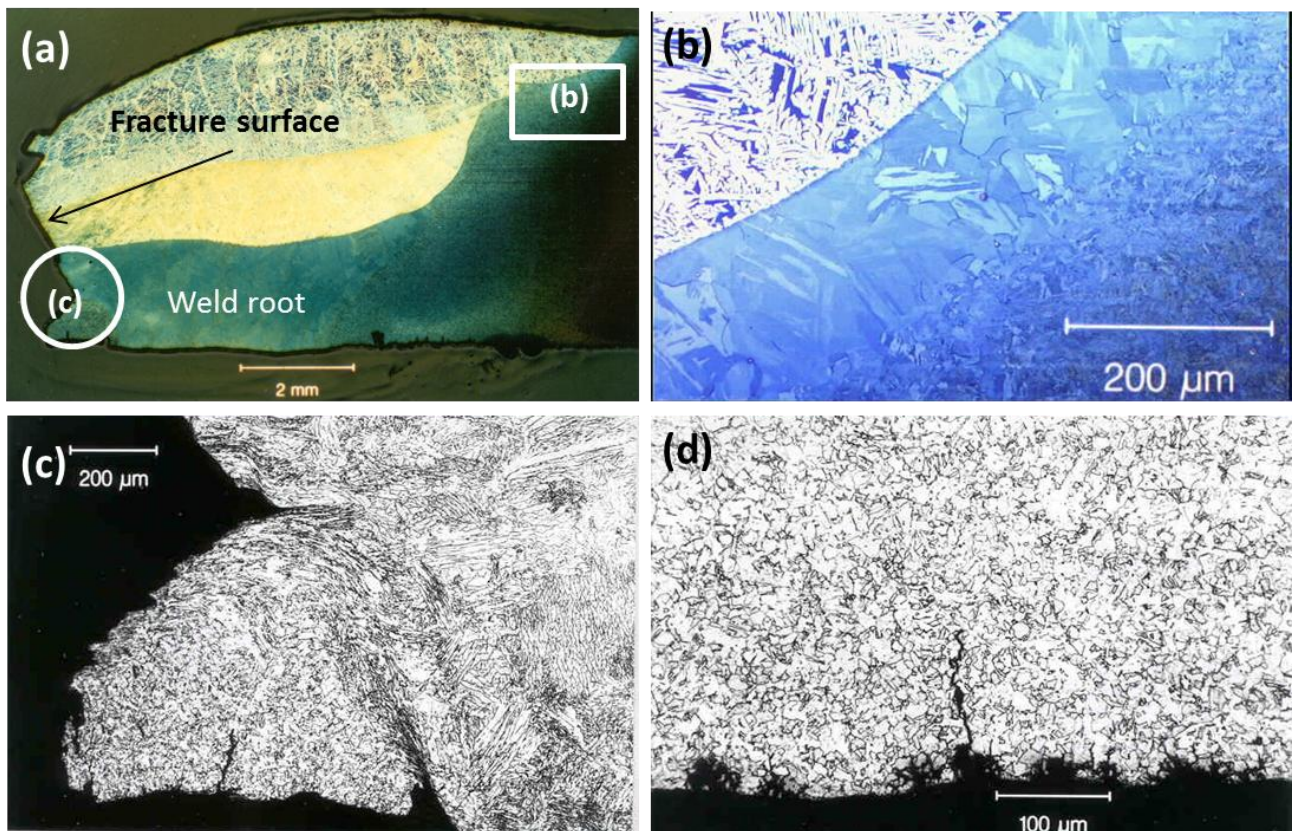


Figure 2-22: Optical microscopy and SEM inspection of the fracture surfaces of SMSS pipeline (a) overview (b) coarsened grains HAZ (c) main crack initiation in the HAZ (d) initiation of cracks at pits in the HAZ [151]

SMSS exhibits in most cases two types of hydrogen assisted failures. During service in sour conditions with low pH values, hydrogen critical concentrations build up on the surface.

At higher pH values, hence lower H_2S concentrations, the steel is subjected to localized corrosion and hydrogen cracking initiates at pits and surface defects [15]. It was shown by Splichal et al. [19] that very small hydrogen concentration can cause a change of the fracture surface characteristic from ductile to brittle and from trans-granular to inter-granular fracture. There is also a strong dependency of the extent of the brittle fracture on the number of saturated hydrogen trapping sites in the material and the hydrogen concentration. The extent of brittle fracture was smaller in weld metal than in base material since the number of saturated traps in this microstructure is larger. When the hydrogen concentration in the weld metal was increased, both weld metal and base material exhibited the same extent of brittle fracture. The changes of the fracture characteristic can be observed in Figure 2-23 and Figure 2-24.

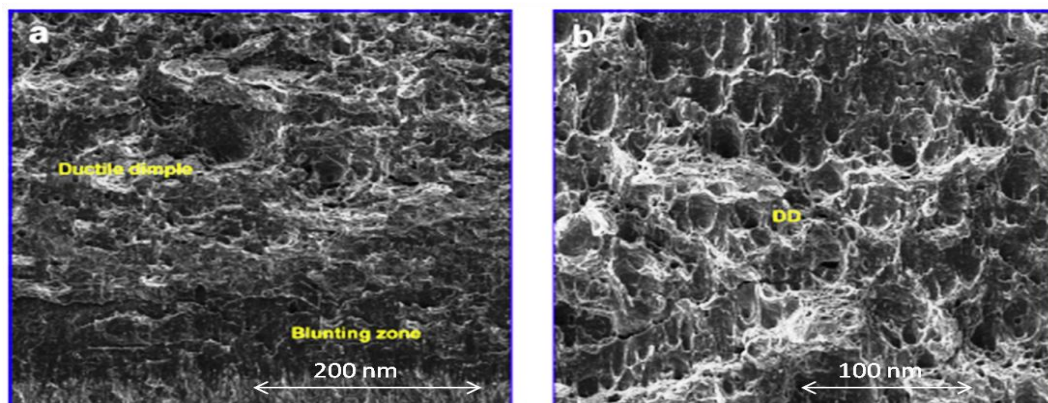


Figure 2-23: Without hydrogen charging (a) the area of crack initiation and (b) the central area of crack growth [19]

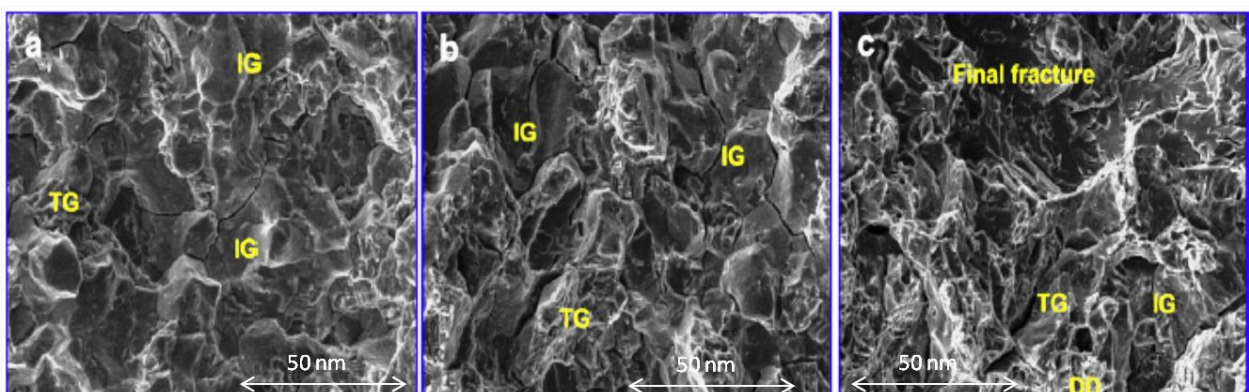


Figure 2-24: Charged with 3 wt. ppm hydrogen (a) area of crack initiation, (b) central area of crack growth and (c) area of near final fracture [19]

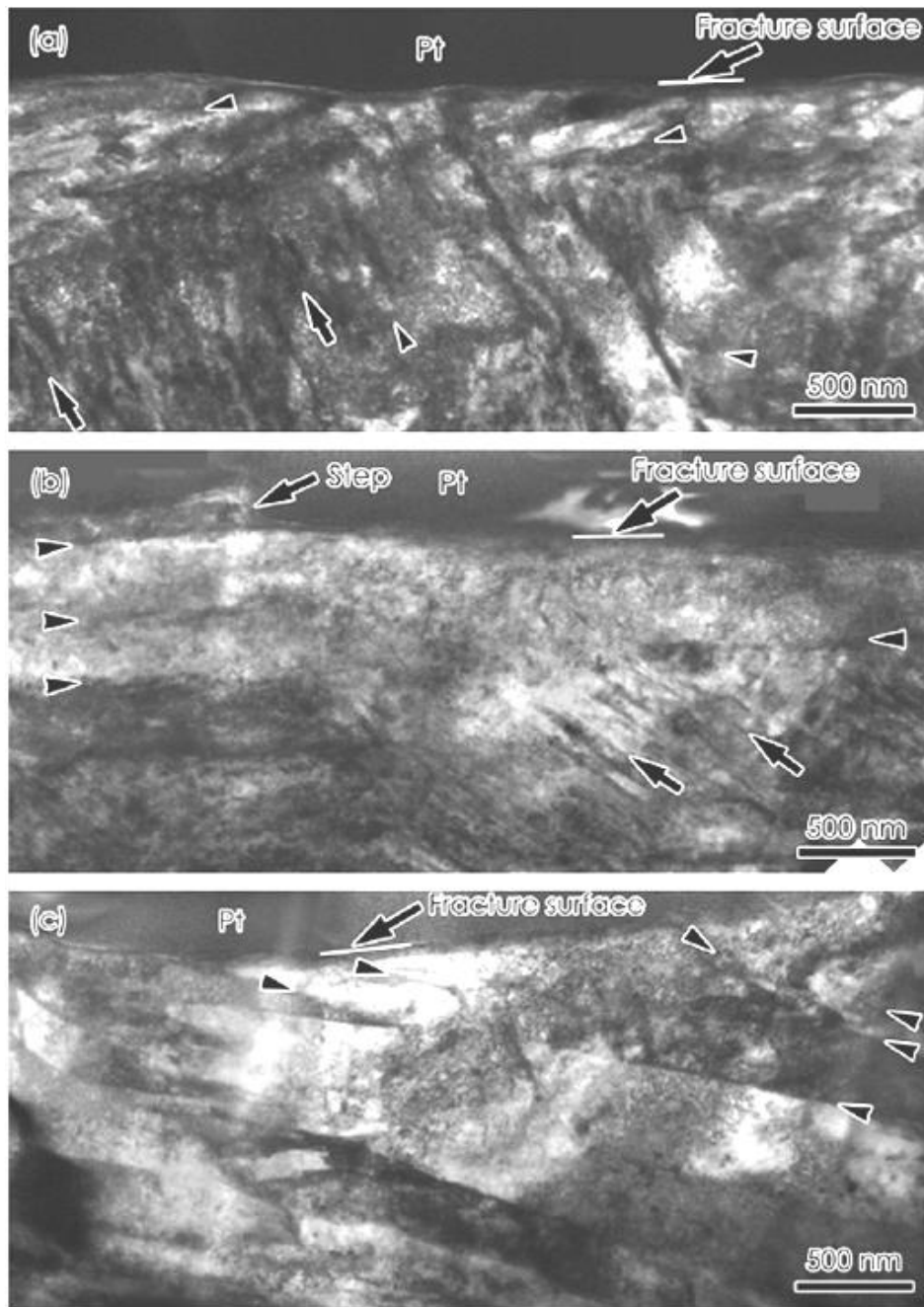


Figure 2-25: TEM micrographs showing microstructure immediately beneath the hydrogen assisted fracture surfaces characterized as (a) “flat”, (b) “quasi cleavage” and (c) low temperature induced “quasi cleavage”. Arrows and arrow heads indicate slip bands and lath boundaries, respectively [17]

The dominant HAC mechanism for SMSS was determined by Nagao et al. [17]. Zinc coated, notched bend specimen was hydrogenated in a high-pressure gaseous hydrogen environment (138 MPa) at 250°C.

It was found that hydrogen assisted failure has appeared along the former austenitic grain boundaries. With the presence of hydrogen the fracture surface was changes from

ductile MVC to a fracture surface which can be described as quasi-cleavage. By preparing TEM samples with a perpendicular orientation to the fracture surface, a direct evidence for the embrittlement mechanism was found. Clear slip bands and significant plasticity were observed beneath the fracture surface as well as partial destruction of lath boundaries (see Figure 2-25). From these observations it can be deduced that the acting mechanism in a lath martensitic stainless steel is hydrogen enhanced and plasticity mediated decohesion mechanism (a combination of the HEDE and HELP mechanisms, when HEDE is more dominant).

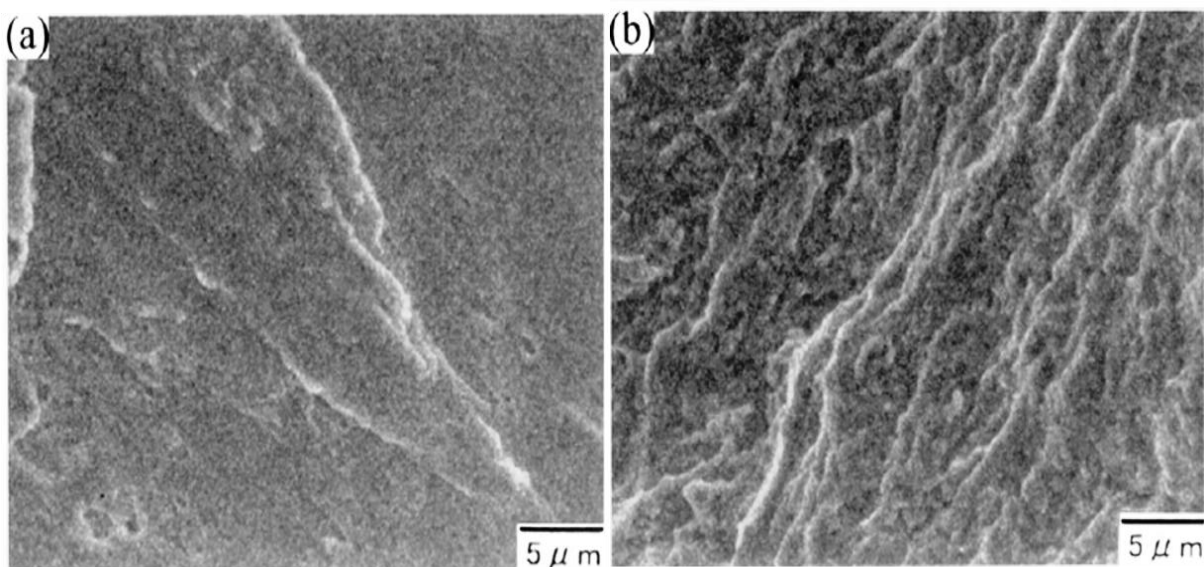


Figure 2-26: SEM (Scanning Electron Microscopy) images of a martensitic steel subjected to a fatigue test at a stress amplitude of 610 MPa (a) with and (b) without hydrogen [16]

In addition, hydrogen has a significant influence on the fatigue life of a SMSS component, as shown by Nagumo et al. [16]. Electrochemical precharging of a sample with hydrogen (before the fatigue test) drastically reduces the fatigue life, and changes the fracture surface as can be seen in Figure 2-26. The fracture surface of a hydrogenated sample exhibits smooth fracture surface without cleavage-like crystallographic features, as opposed to the uncharged sample, which exhibits rough fracture surface. The fracture surface reveals an increased defect density in the hydrogenated sample, indicating hydrogen assisted crack initiation. This assumption is also based on the fact that a crack initiates at earlier stages of the fatigue test at the hydrogenated sample than in the uncharged sample. It can be concluded from these experiments that hydrogen, when it

reacts with point defects in the material, significantly reduces crack growth resistance and increases the susceptibility of the material to crack initiation under conditions of cyclic loading. The finding of very early fracture in the presence of hydrogen proves that hydrogen is involved in the crack initiation phase through interactions with sub-structural changes during the crack's incubation phase.

2.6.1. The role of the retained austenite in the embrittlement process of SMSS

The retained austenite in the SMSS component also has an important role with respect to HAC. Since the austenitic phase has significantly larger hydrogen solubility than the ferritic/martensitic phase, it acts as a hydrogen source when the component is under mechanical load.

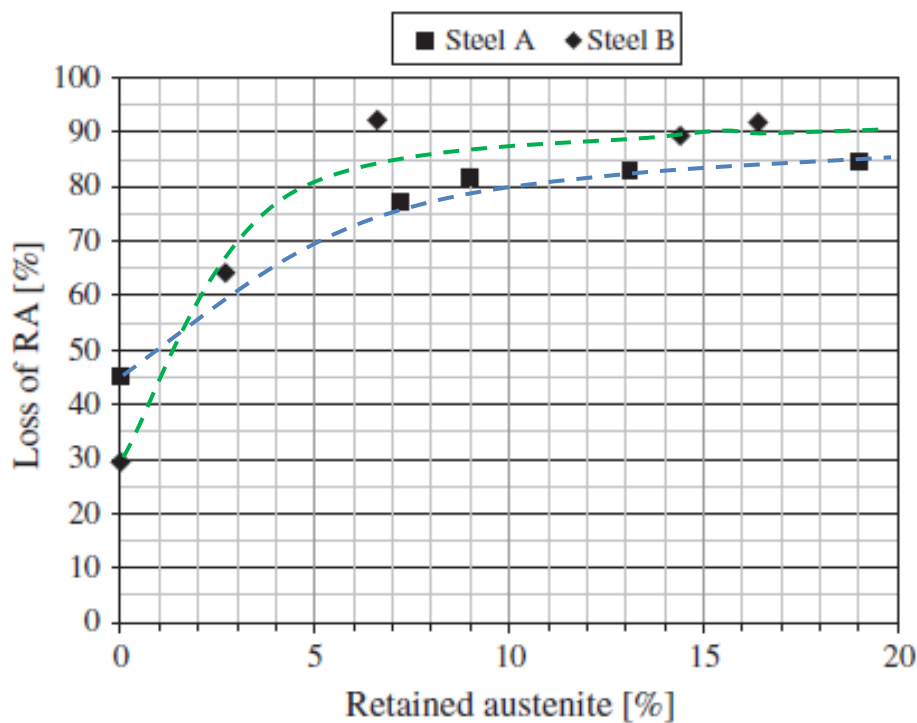


Figure 2-27: Loss of RA (the ratio between the cross section of the fractured sample and the initial cross section before testing) as a function of retained austenite for two types of SMSS pipeline steels (containing 12% Cr content) [153]

It was shown by Solheim et al. [150] by testing three different grades of SMSS (two typical low carbon pipeline steels and AISI 420) that a higher content of retained austenite

in the material leads to a greater loss of ductility when hydrogen is introduced into the material. The SMSS samples were heat treated in order to obtain different austenite content levels, and in order to examine the influence of different austenite content on the mechanical properties of the material. It was concluded that under conditions of external load the hydrogen, which is stored in the austenitic phase, is released from these "traps" and diffuses through the martensitic matrix to assist in crack initiation and/or propagation. Solheim's experiments demonstrated that the hydrogen solubility in the material increases with higher retained austenite content, which leads to a reduction of the material's ductility, as highlighted in Figure 2-27.

2.7. Fundamentals of X-ray Diffraction (XRD)

XRD is a non-destructive method of investigating and measuring the microstructure of a material and analyzing its phase compositions, as well as calculating surface residual stresses to depths of up to around 30 μm (depends mostly upon the beam energy) by measuring a material's inter-planar spacing [154]. The lateral resolution of the XRD technique depends upon the XRD focusing optics and is typically of mm order. Laboratory X-rays have wavelengths of the order of a few angstroms (\AA), which is the same order of magnitude as the typical inter-atomic/inter-planar spacing in metallic materials lattice. For this reason an interaction occurs between the X-ray photons and the material's lattice. X-rays scattered from a polycrystalline solid can constructively interfere producing a diffracted beam. The angles (usually assigned as θ) at which the maximum diffracted intensities occur are measured. From these angles it is possible to obtain the inter-planar spacing, d , of the diffraction planes using Bragg's law, as can be seen in Figure 2-28 and Equation 2-3.

$$(2-3) \quad n\lambda = 2d \cdot \sin \theta$$

Where λ is the diffracted wavelength, d is the interplanar spacing and θ the diffraction angle.

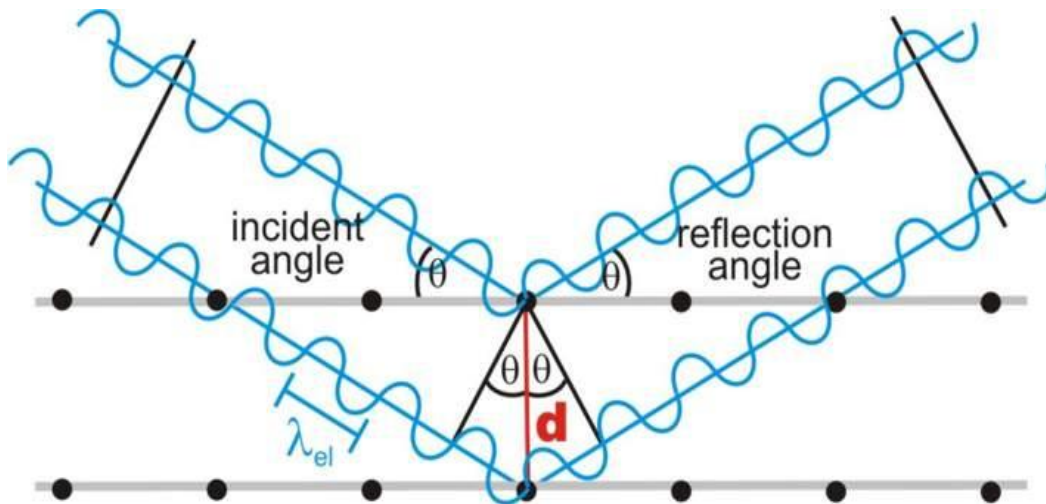


Figure 2-28: Illustration of constructive interference between X-ray photons according to Bragg's law

If residual stresses exist within the sample, then the d spacing will be different from that of an unstressed sample (i.e. d_0). The difference is proportional to the magnitude of the present residual stress. In principle, the grains of the material are being used as internal strain gauges for residual stresses.

Due to the low penetration depths of the laboratory XRD technique, measurements are restricted to the surface of materials, but benefit from the use of a differential analysis technique so that a stress-free reference (i.e. d_0) sample is not necessarily required, since an approximation of d_0 can be applied to the measurement. The diffraction angle, 2θ , and hence the lattice spacing, d , can be determined for multiple inclination angles, ψ , of the sample surface. Using these parameters enables the residual stresses to be determined by the $\sin^2\psi$ method, as will be explained in detail in Section 4.5. The use of XRD for material characterization has the advantages of being non-destructive, for it enables both laboratory and real application examinations, and the process can be relatively easily applied, consequently having low application costs.

The Synchrotron Diffraction or Energy Dispersive X-ray Diffraction (EDXRD) technique carries out crystal structure examination and residual stress measurements using the same principle as standard XRD. However, synchrotrons provide very intense beams of high energy x-rays, a million times more intense than laboratory based x-rays systems and therefore have a much higher depth of penetration (of about 20mm in steel). In addition, due to the high intensity of the beam it enables a much shorter acquisition time for a comprehensive diffraction spectrum [155]. Moreover, synchrotron diffraction is capable of providing high spatial resolution, 3D maps (tomographies) of the strain distribution to

millimetres depths in engineered components [156]. The big disadvantage of using synchrotron diffraction is the lack of ability to perform the measurements on real life applications and/or components and it is restricted to laboratory examinations in a synchrotron facility.

2.8. Residual stresses

Residual stress is an intrinsic stress in the material which is present in the absence of external loading [157,158]. It arises from misfits (eigenstrains) either between different regions or between different phases within a material. It occurs usually due to processing of the material whether mechanical, thermal or chemical. One important characteristic of residual stresses is that the sum of all of the combined residual stresses in a component must be equal to zero in all of the orientations, in case that no external load is applied to that component. The sorts of residual stresses are categorized into three different and main categories. Type I (σ^I); macro-residual stresses. These are stresses that vary within the component in a scale much larger than the average grain size. The other two types of residual stresses are referred to as microscopic stresses. Type II stresses (σ^{II}) vary on the scale of a single grain and may be caused by anisotropy in the behavior of each neighbor grain or phase. Type III stresses (σ^{III}) have the smallest scale and their range varies of a few atomic distances. These stresses are essentially caused by the presence of a dislocation or microstructure defects such as vacancies, interstitial atoms etc. an illustration of the scale of the three types of the residual stresses is presented in Figure 2-29.

Studying the aspect of residual stresses in a material is of high importance for the ability to predict the service lifetime of a given metal component. The residual stresses play an important role in crack formation in the material. The understanding of hydrogen influence on residual stresses may potentially assist in the understanding of HAC, and in predicting the time to failure of a material exposed to hydrogen environment, either in the presence of a corrosive media or hydrogen gas in high pressure vessels. One important factor that contributes to the cracking process is the residual stresses state in the material and especially in the surrounding of a crack's tip. The presence of high residual stresses levels leads to an increased anodic dissolution on one hand or to the opening and advancement of a crack on the other hand. Residual stresses have the largest effect relating to fatigue

cracking. The addition of residual stresses to the applied stress cycle can significantly accelerate or delay the initiation of a fatigue crack [159–161].

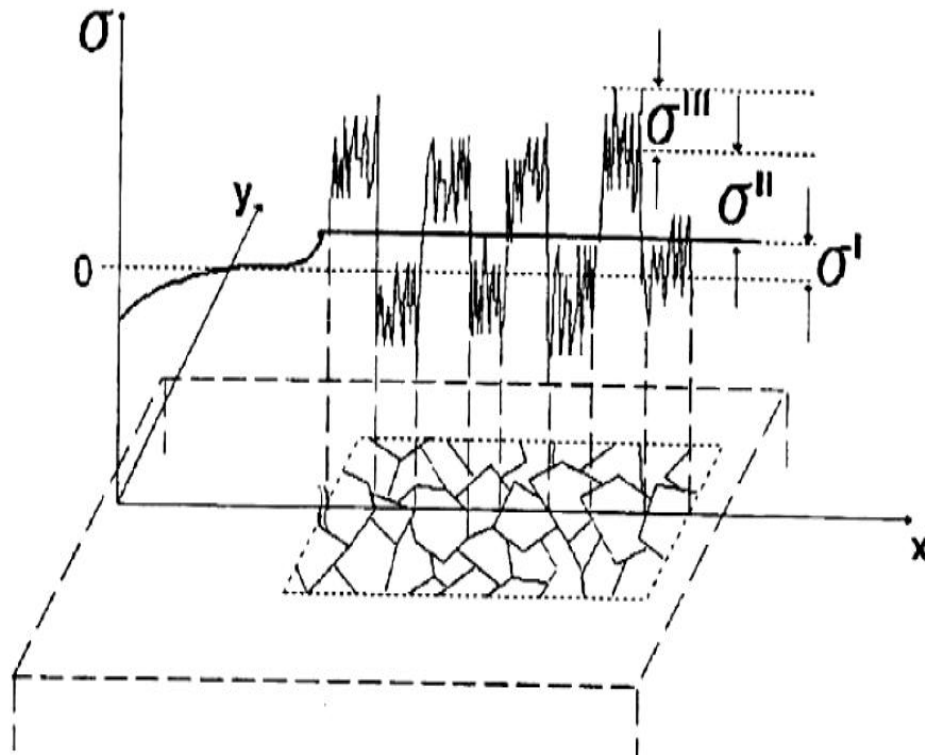


Figure 2-29: Classification of the three types of residual stresses according to their scale [157]

Quantifying the residual stresses present in a component is crucial for a number of reasons including to approve the component to a certain application, and to understand the cause of an unexpected and premature failure under service conditions, and under stresses below the tensile strength of the component's material.

The application of XRD procedure for residual stresses analysis for engineering applications began in the early 1950's. By the 1970's it was routinely applied in the nuclear and aerospace industries. This method is used for the calculation of macroscopic stresses from the present elastic strains in the component. The shallow depth of the X-ray penetration and small irradiated area allow for better and more accurate measurements of residual stresses distributions with spatial and depth resolution than all other existing methods. Current practice dictates that the XRD procedure for residual stresses measurements is readily available, both laboratory-based and portable, for measurements in real life applications [162].

2.8.1. Hydrogen interaction with residual stresses

The interaction and the influence of hydrogen on residual stresses in different kinds of materials were studied by several researchers and methods [159,163–168]. Toribio et al. was focusing on this issue in the case of steels. It was proved that stress and strain influence the hydrogen diffusion in the prestressing steel wire and affect the time to failure of the material. It was shown in [159] that compressive residual stresses in the component delay the hydrogen entry and consequently delay the failure of the component during fatigue test. In [163] Toribio simulated the hydrogen diffusion characteristics in the presence of tensile residual stresses. It was found that hydrogen ingress in the component is enhanced through the presence of tensile residual stresses and higher hydrogen concentration is obtained under these conditions. It is also mentioned that the highest hydrogen concentration is achieved on the wires surface and its vicinity, the area with the highest value of tensile residual stresses after cold drawing process (see Figure 2-30). This observation and its corresponding conclusions is particularly significant in the case of HAC since the combined presence of high tensile stresses and hydrogen concentration can lead to a faster crack initiation and consequently to a premature and unpredicted failure of the component.

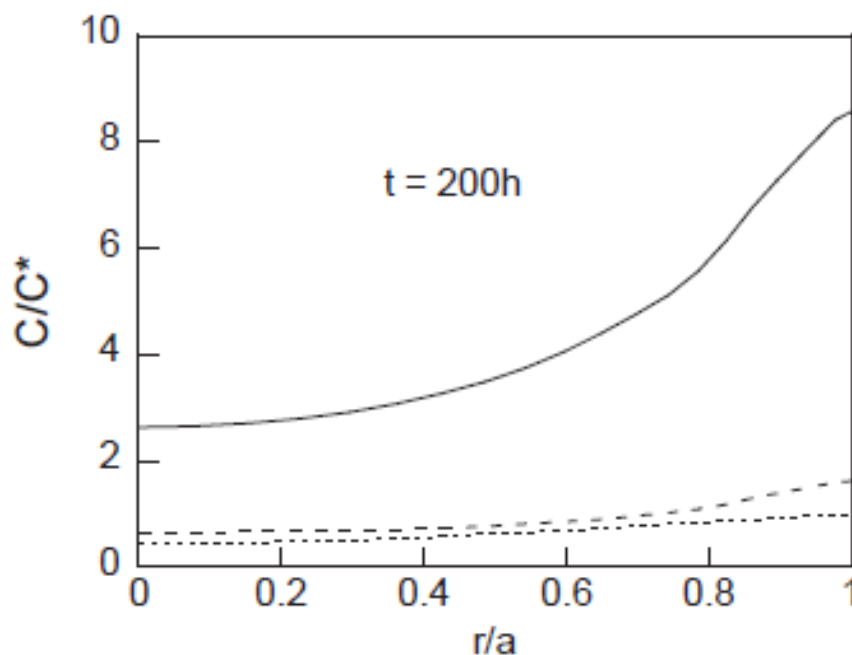


Figure 2-30: Distributions of relative concentrations of hydrogen (C/C^*) as a function of the dimensionless radial coordinate r/a , at diffusion time of 200 hours, for three modeling scenes: stress-and-strain assisted

diffusion (full line), stress-only assisted diffusion (dashed line) and conventional diffusion with no stress or strain assistance (dotted line) [165]

Barnoosh et al. [166] showed that hydrogen and tensile residual stresses have a significant influence on the microstructure of the alloy and thus on the mechanical behavior of a super duplex stainless steel. The ingress of hydrogen in the material with the presence of tensile residual stresses induces a severe plastic deformation that appeared as slip lines on the surface of the austenitic phase as was observed by means of Atomic Force Microscopy (AFM) and presented in Figure 2-31. This interaction took place in the highly stressed regions and caused microstructural changes. These microstructural changes can contribute to the degradation of the material's mechanical properties and play a crucial role in the HAC susceptibility of the serving material.

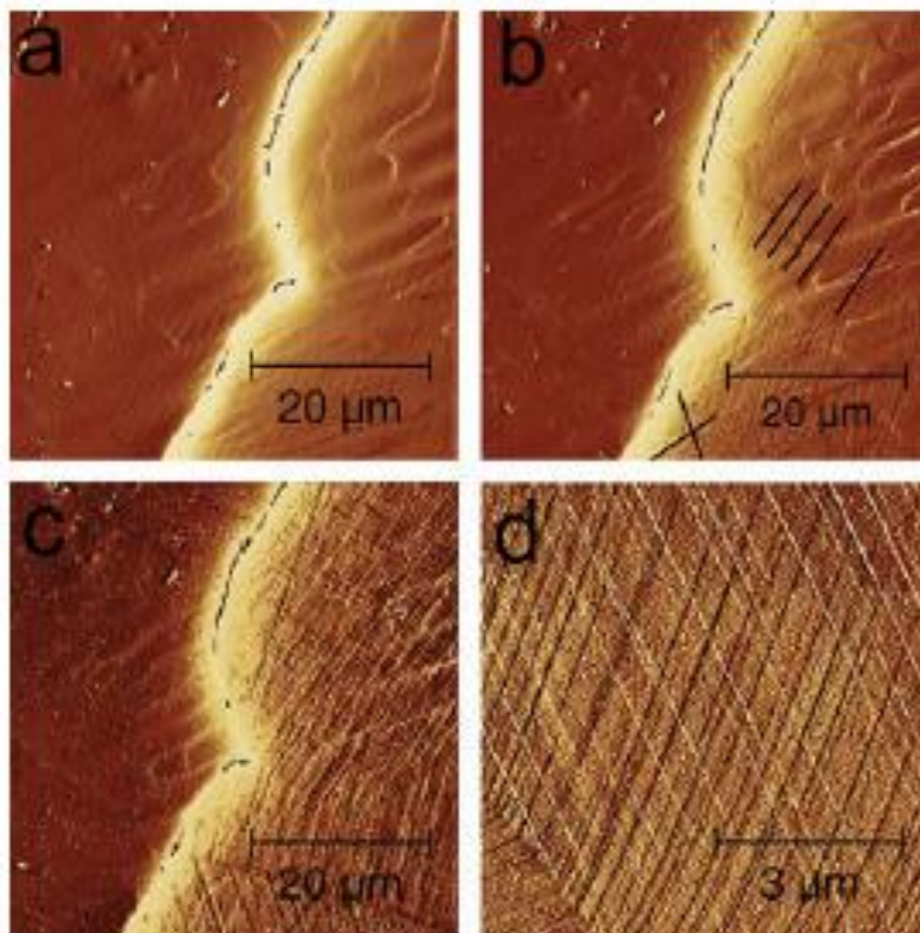


Figure 2-31: EC-AFM deflection mode images from the surface of the sample during in situ electrochemical H-charging. (a) Before H-charging at the open circuit potential; on the left is a ferrite grain and on the right is an

austenite grain which can be easily distinguished by its convex grain boundary. (b) The image of the same position after 1 h of in situ H-charging. (c) The image of the same position after 2.5 h of in situ H-charging. (d) Higher magnification image from the surface of the austenite grain [166]

It can be summarized that the presence of residual stress has a double effect in the aspect of HAC; first, the presence of tensile residual stress enhances the ingress of hydrogen in the component resulting in higher hydrogen availability. Second, the combination of tensile stress with hydrogen presence can lead to a catastrophic failure of a serving component due to the degradation of the mechanical properties induced by hydrogen. On the other hand, compressive stresses are acting in the opposite way; they suppress the ingress of hydrogen in the material and thus retard HAC related failures.

3. Objectives of the study

According to the actual state of knowledge and excitant knowledge of hydrogen behavior in SMSS it is known that those steels can undergo a failure that is due to HAC. These steels are widely applied in the petrochemical industry as pipelines for gas and oil transportation. A component failure under the stated conditions can lead to casualties as well as severe damage in the environmental and financial sectors. It was extensively proved and reported that hydrogen uptake has been involved in the majority of the failures in these applications and the failure mechanisms were more or less explained for some of the failure cases. However, none of these research works presented or suggested a procedure for the predication and prevention of the mentioned phenomenon due to the insufficient knowledge and data about hydrogen transport. Thus, in order to extend the knowledge of hydrogen behavior in SMSS and in order to facilitate the ability to create a procedure which enables the prediction of a component failure under hydrogen environment, the work was focused on the following objectives:

- To study and to extend the knowledge of hydrogen lattice diffusion in SMSS and to determine the phase specific lattice diffusion and solubility characteristics
- To determine and characterize the interaction of hydrogen with the existent residual stresses in a SMSS component
- To apply EDXRD analysis as an in-situ method for the measurement and analysis of hydrogen transport behavior in metals for the first time

4. Experimental procedure

4.1. Supermartensitic stainless steel

For the scope of this work, a SMSS of grade 1.1365 (13 for 13% Cr and 65 for 6.5% Ni) was chosen, which is categorized as high alloyed SMSS due to the relative high nickel and molybdenum contents, as was classified and presented in Table 2-1. The chosen material was delivered to BAM from H. BUTTING GmbH & Co. KG as a 20mm thick rolled and annealed plate. The tested specimens in this study were machined and processed from this received plate in the as-received version. The chemical composition of the tested material is listed in Table 4-1 as it was received from the manufacturer as stated in the shipping note. The material has a martensitic structure with about 15 vol.-% retained and annealing austenite in the martensitic microstructure, as validated by XRD, EBSD (Electron Back Scatter Diffraction) measurements and Transition Electron Microscopy (TEM) which is presented in Figure 4-1.

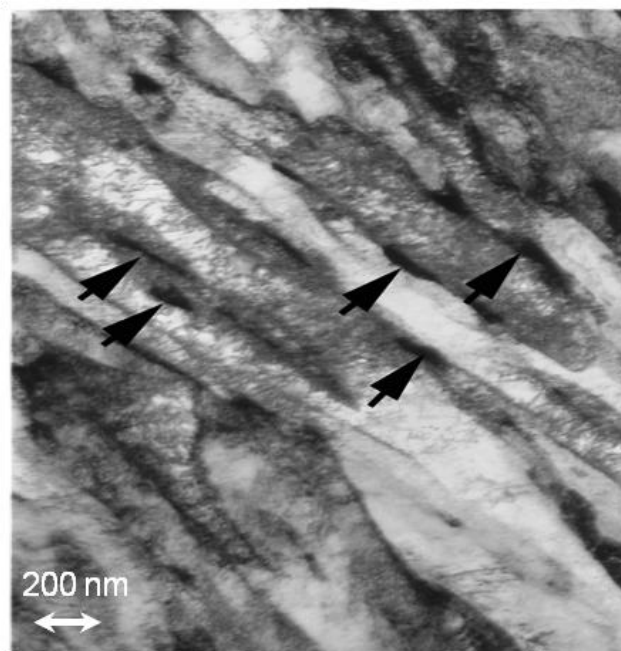


Figure 4-1: TEM image of the SMSS showing the martensitic lath microstructure and the austenite particles (see the black arrows) that are finely distributed between the martensitic laths [99]

Table 4-1: Chemical composition of the investigated SMSS as received from the manufacturer (values are given in wt.-%)

C	Mn	P	S	Si	Co	Ni	Cr	Mo	Al	N
0.006	1.870	0.021	0.0009	0.294	0.475	6.498	11.65	2.330	0.007	0.009

This type of steel, due to its microstructure and phase composition, facilitates the type of examinations that are scoped for this study. The fine distributed austenitic phase with its high hydrogen solubility and low diffusivity, combined with the surrounding martensitic phase with its high hydrogen diffusivity and low solubility creates a so-called structure of “highways and parking lots”. The absorbed hydrogen can move relatively fast in the martensitic phase which act as the highways and “settles” in the austenite small and fine distributed islands between the martensitic laths which act as the parking lots. Consequently to this characteristic the austenitic phase contains high amount of solute hydrogen, which reaches close to the solubility limit and therefore induces a large scale of lattice distortions that can be distinguished and observed by XRD procedure. Other grades of steels that are usually applied in the petrochemical industry and are also exposed to a hydrogen environment, such as duplex steels or ferritic steels do not enable this kind of examination due to their different microstructure and the consequent hydrogen behavior in the respective microstructure. For example, duplex stainless steel contains about 50-50 composition of ferritic and austenitic phases. Due to the low hydrogen diffusivity in the austenitic phase, which is distributed as large particles in the ferritic matrix, the majority of hydrogen is located at the interfaces between the ferritic and austenitic phases and in the outer layer of the austenitic phase particles. This kind of hydrogen distribution inhibits a simple detection of lattice distortions when using the XRD method.

The mechanical properties of the delivered steel plate were examined and yielded the following characteristic: yield strength of around 620 MPa, Ultimate tensile strength of 920 MPa, and elongation rate until fracture of around 22%. These results were extracted and can be seen in the obtained stress-strain diagram in Figure 4-2.

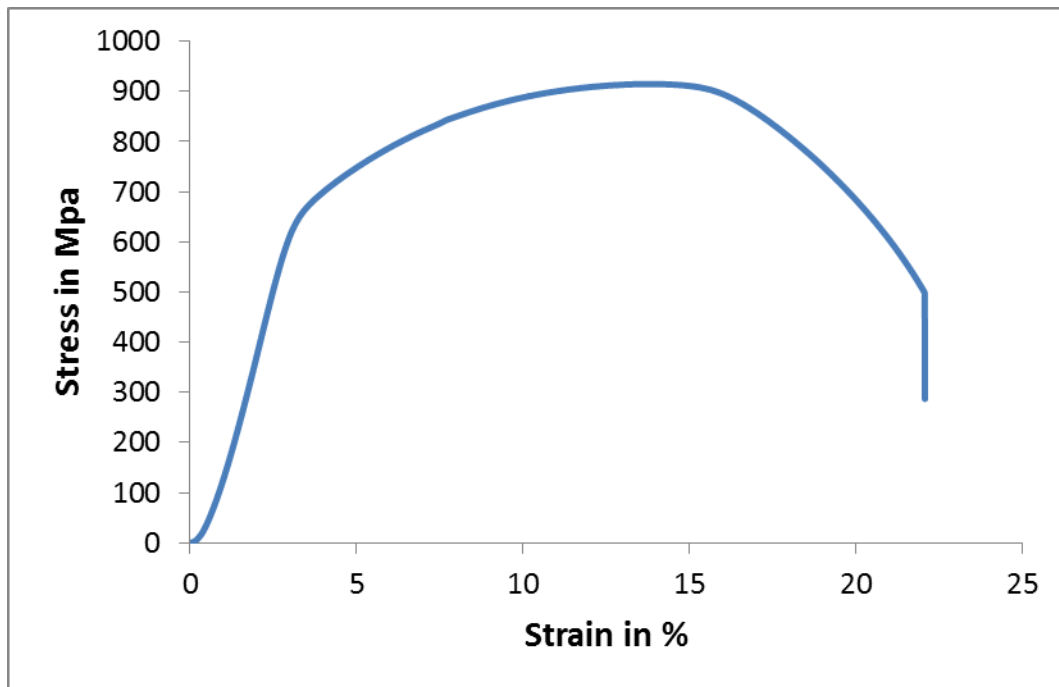


Figure 4-2: Technical stress-strain diagram of the as received SMSS. The tensile test was conducted at BAM laboratory at room temperature

4.2. Hydrogen cathodic charging

There are several methods of introduction of hydrogen into a metallic material, among them electrochemical cathodic charging, high pressure gaseous phase charging, and introduction through a welding process.

The studied material in this research was hydrogen charged by means of cathodic electrochemical charging method. This charging method simulates the service of a component in a sour surrounding and under conditions of cathodic protection or galvanic coating, which prevent corrosion reactions to occur on the surface of the component.

In general, the cathodic charging technique generates atomic hydrogen on the specimen's surface. A power supplier generates a constant current in the electrochemical cell, while the studied specimen acts as a cathode and an inert metal electrode (such as platinum) acts as an anode. The hydrogen positive ions (H^+) in the electrolyte are attracted to the cathode where a reduction reaction occurs and the hydrogen adatoms are absorbed and adsorbed into the cathodic polarized specimen. The anode is located symmetrically to the cathodic polarized ribbon, thus distributing the potential uniformly around the specimen.

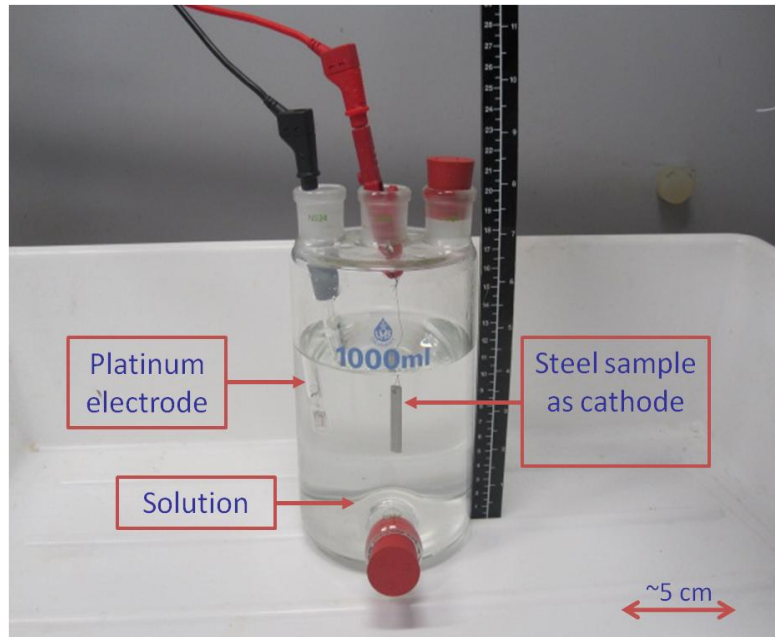


Figure 4-3: The electrochemical cathodic charging cell. The sample in the middle of the bottle which acts as a cathode, and the platinum electrode on the right side which acts as an anode

In order to inhibit the recombination reaction of hydrogen atoms to H_2 molecules on the sample's surface, traces of VI column elements are added as surface recombination inhibitors. The inhibition of the recombination reaction promotes the uptake rate of hydrogen atoms into the tested sample [169].

The hydrogenation (hydrogen charging) process in this study has been performed at room temperature in 0.5N H_2SO_4 solution containing 0.25 g/l of surface recombination inhibitor $NaAsO_2$ (sodium arsenide). The SMSS specimen was polarized as a cathode and a platinum electrode as an anode. The process was conducted under constant current density of varied values, and for varied periods of time, as required for the specific experiment. The assembly of the cathodic charging cell can be seen in Figure 4-3.

4.3. Carrier Gas Hot Extraction system (CGHE)

For the purpose of analyzing the hydrogen uptake and the hydrogen effusion behavior the CGHE system was used (see Figure 4-4).



Figure 4-4: The laboratory setup of the CGHE system developed by JUWE

This system is composed of a sample insertion quartz tube, an induction heating body, a system of filters to remove humidity and other impurities and a thermal conductivity detector (TCD). The hydrogen in the sample is transported to the surface after being thermally activated and released from its trapping site, and then diffuses from the trap to the surface. Due to interface reactions hydrogen desorbs and recombines to molecular hydrogen (H_2) at the surface of the sample. A constant carrier gas stream of N_2 (nitrogen) transports the hydrogen to the thermal conductivity detector (TCD) through an array of filters (reagents), as illustrated in Figure 4-5.

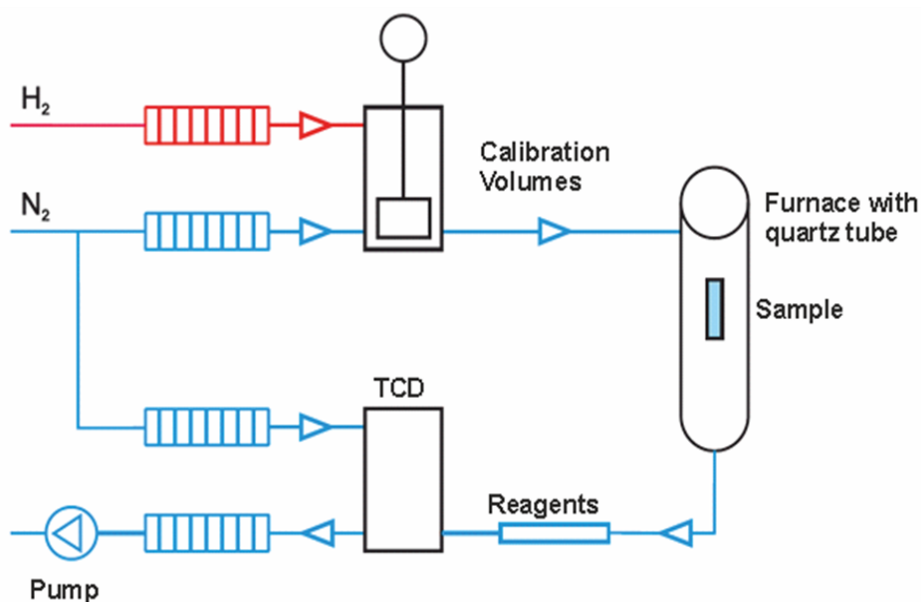


Figure 4-5: Schematic of the CGHE system

The received voltage signal from the TCD is then converted to a hydrogen amount and concentration in accordance to the sample's mass.

The calibration of the system is accomplished by inserting known amounts of hydrogen gas (H_2) into the nitrogen carrier gas (N_2). According to the signal values obtained from the TCD, a calibration curve can be established, as shown in Figure 4-6.

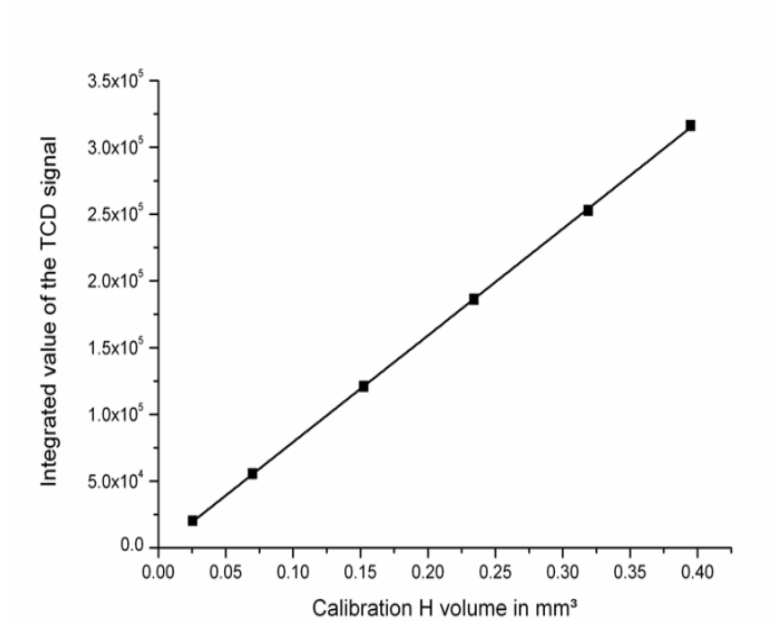


Figure 4-6: Calibration curve of the TCD signal dependency on hydrogen content in the carrier gas

According to the following calibration curve, the values obtained from the TCD can be converted to hydrogen total volume that was emitted from the sample and then with respect to the samples mass, the hydrogen concentration can be calculated.

4.4. Hydrogen desorption measurements by means of Energy Dispersive X-ray Diffraction

4.4.1. Hydrogen desorption by degassing at room temperature

The influence of hydrogen presence on the phase composition and lattice parameter was observed and measured by means of Energy Dispersive X-Ray Diffraction (EDXRD) provided at the beam line EDDI at the synchrotron facilities of the Helmholtz Zentrum Berlin

(HZB – BESSY II). This facility was used for the purpose of realization of in-situ measurements of the material's lattice distortion due to hydrogen presence and during hydrogen desorption. The beamline EDDI provides white synchrotron radiation beam with energy values ranging from 15 to 120 keV. The spectrum of the white beam as was recorded by the detector is shown in Figure 4-7.

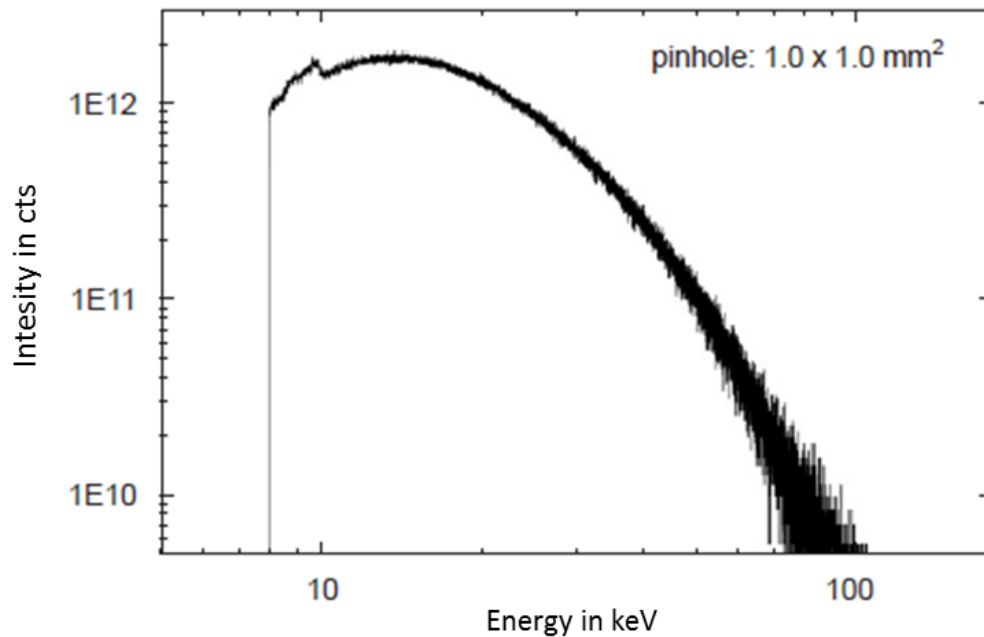


Figure 4-7: Energy spectrum of the white beam through a pinhole of 1X1 mm² corresponding to a ring current of 250mA [110]

The wide X-ray photons energy range and the wide detectability range of the detector enable the possibility of keeping the positions of the source and the detector fixed. For the following examinations the diffraction angle 2θ was set to a constant value of 12° . This angle is ideal for distinguishing the diffraction lines of different phases (establishing a satisfactory distance between the diffraction lines in order to avoid and/or minimize the overlapping of the lines) as well as obtaining data from deeper layers inside the material for depth profiling of the examined effects. A schematic of the experimental setup can be seen in Figure 4-8, and the real assembly, which was used for the execution of the experimentation program in the EDDI beam-line chamber, is presented in Figure 4-9.

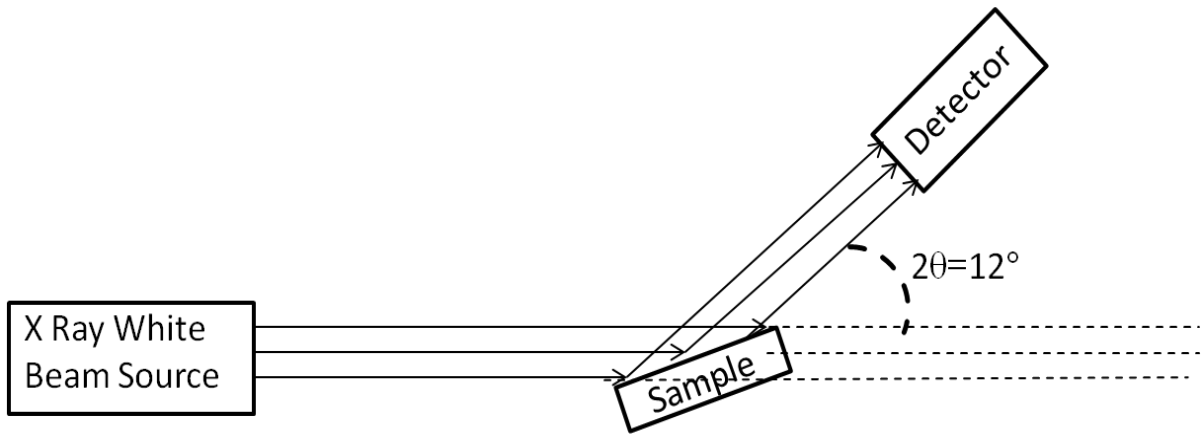


Figure 4-8: The experimental setup of the desorption at ambient temperature experiment

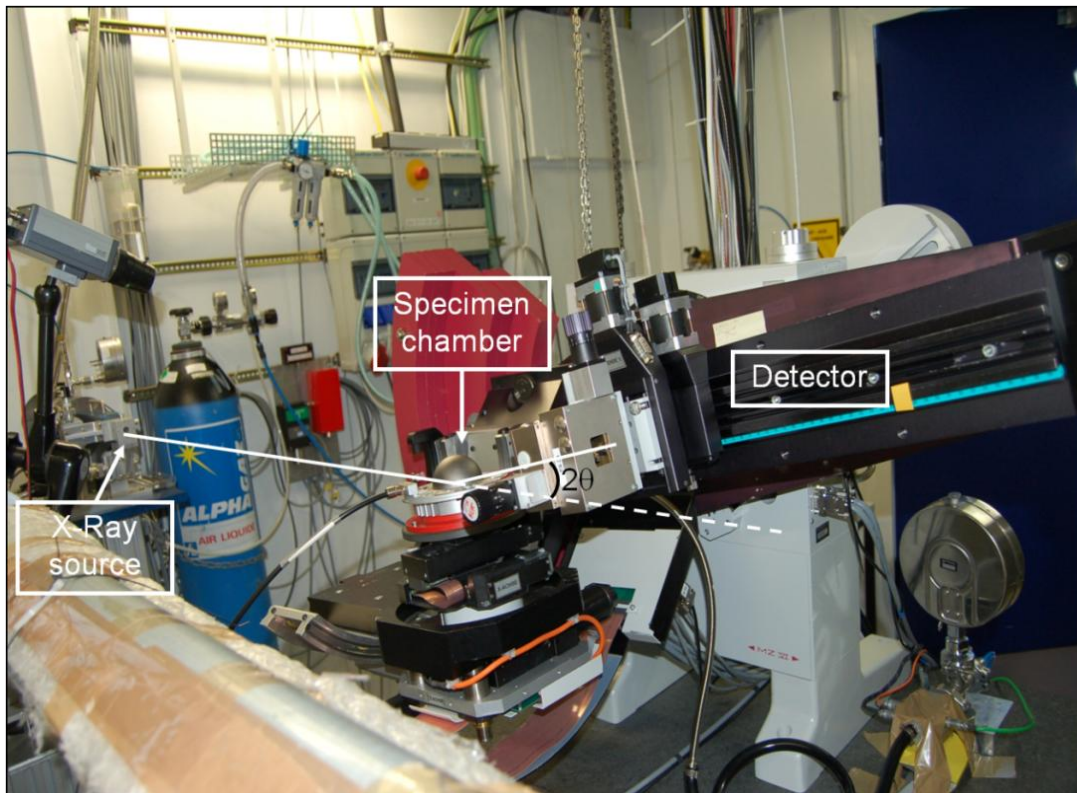


Figure 4-9: The experimental assembly in the EDDI experiments chamber at the synchrotron facility BESSY II in Berlin

The constant angle 2θ , the high intensity of the beam and the wide radiation energy range provide the conditions for obtaining a comprehensive diffraction spectrum within a very short time, of approximately 20 seconds. An example of a diffraction spectrum of steel can be seen in Figure 4-10. An important feature of this spectrum is the X axis. Whereas in conventional diffraction spectrums it represents the 2θ angle, in this method it represents

the energy of the diffracted X-ray. Since each of the diffraction lines possess different energy value of the reflected X-ray beam it has consequences on the measured parameters as will be elucidated in the following sections.

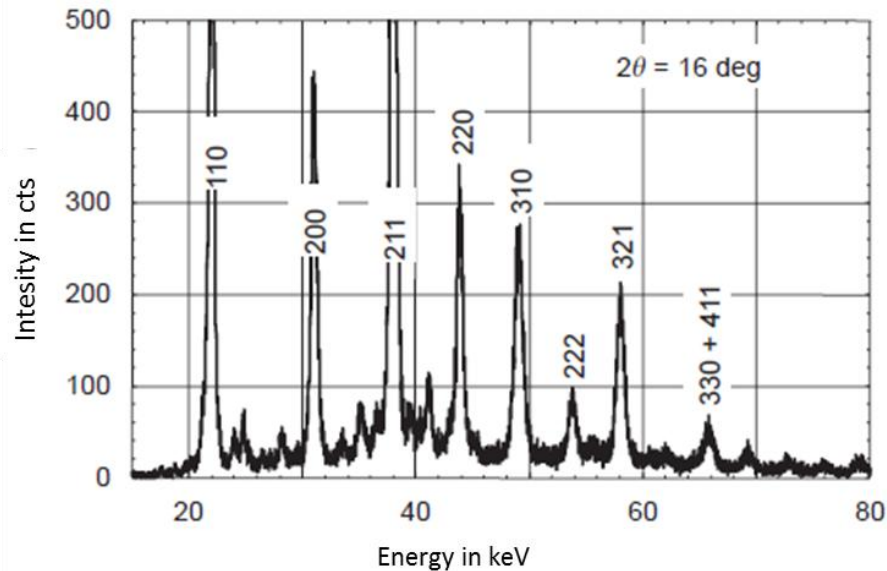


Figure 4-10: An example of a diffraction spectrum of a steel sample, obtained using EDXRD [170]

The previously discussed capabilities of the synchrotron radiation allow in-situ measurements of the diffraction spectrum's modifications caused by hydrogen presence during a period of 24 hours at an ambient temperature which, according to the draft standard ISO 3690 [171], is sufficient for desorption of the very majority of the diffusible hydrogen in the lattice. Each acquisition of a single and full diffraction spectrum lasted a time period of about 20 seconds and diffraction spectrums were continuously acquired during the whole experiment.

After the acquisition of the diffraction spectrums the exact positions of the diffraction lines were determined by application of the diffraction curve to a Pseudo-Voigt function. This was following the correction of the obtained diffraction spectrums from absorption, background and beam source artifacts. An example of the fit and the acquisition of the line's position on the energy axis can be seen in Figure 4-11. This fit was conducted using a macro of the Wolfram's "Mathematica" software (the software is commercially available at <http://www.wolfram.com/mathematica/>).

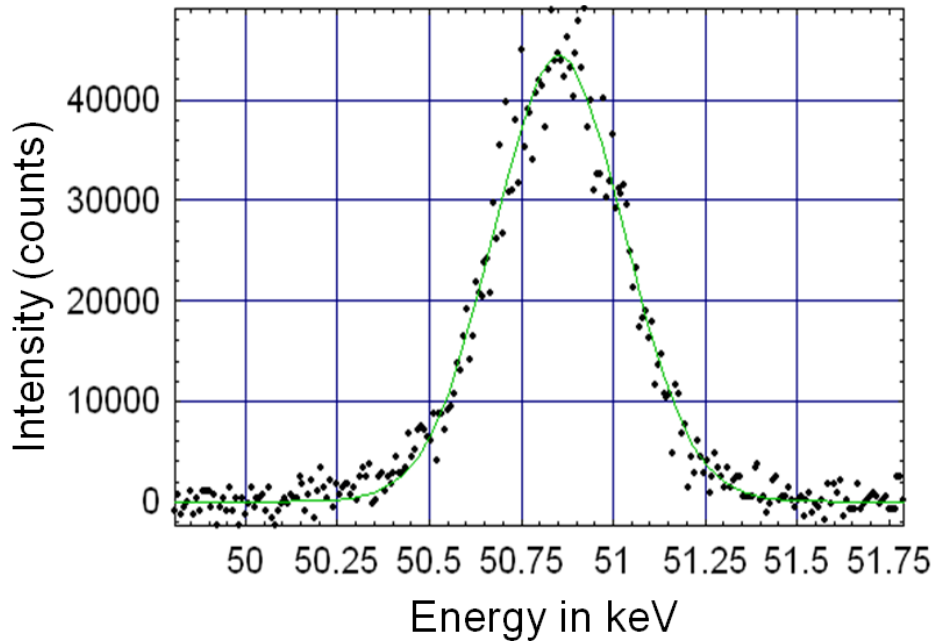


Figure 4-11: An example of the fit of the diffraction line $\alpha(2\ 1\ 1)$ to the Pseudo-Voigt function (the black spots are the experimental results and the green curve is the fit)

By using the described procedures, a depth profile of the inter-planar spacing and its changes can be obtained. According to the energy value of the diffraction line (corresponding the diffraction line's position on the x axis), the acquired information arrives from various depths in the studied specimen. This means that a diffraction line having a higher energy value carries information from deeper depths inside the material. It should be mentioned that the information carried by a single line is originated from the integrated depth; hence, the sum of the area up to the penetration depth. The beam's penetration depth, or the integrated depth of the collected data, can be calculated as a function of the diffraction angle θ and the corresponding Miller indices hkl , assembled into the following equation:

$$(4-1) \quad \tau(hkl, \theta) = \frac{\sin \theta}{2\mu(E)} = \frac{\sin \theta}{2\mu \left[\frac{hc}{2 \sin \theta} \frac{1}{d(hkl)} \right]}$$

Where τ is the absolute beam penetration depth as a function of the diffraction angle and the miller indices, θ : the diffraction angle, E : the beam Energy, d : corresponding inter-

planar spacing to the current hkl , h : Plank constant μ : the material's absorption coefficient, c : light velocity [172].

4.4.2. Hydrogen degassing at elevated temperatures

For the measurements and evaluation of the hydrogen influence on the material's lattice, thermal desorption measurements were carried out in the synchrotron measurement chamber. For that purpose, a heating unit was added to the experimental setup, as can be seen in Figure 4-12. The measurement was conducted while the sample was surrounded by an atmosphere of nitrogen gas as a shielding gas in order to avoid oxidization of the sample's surface at elevated temperatures.

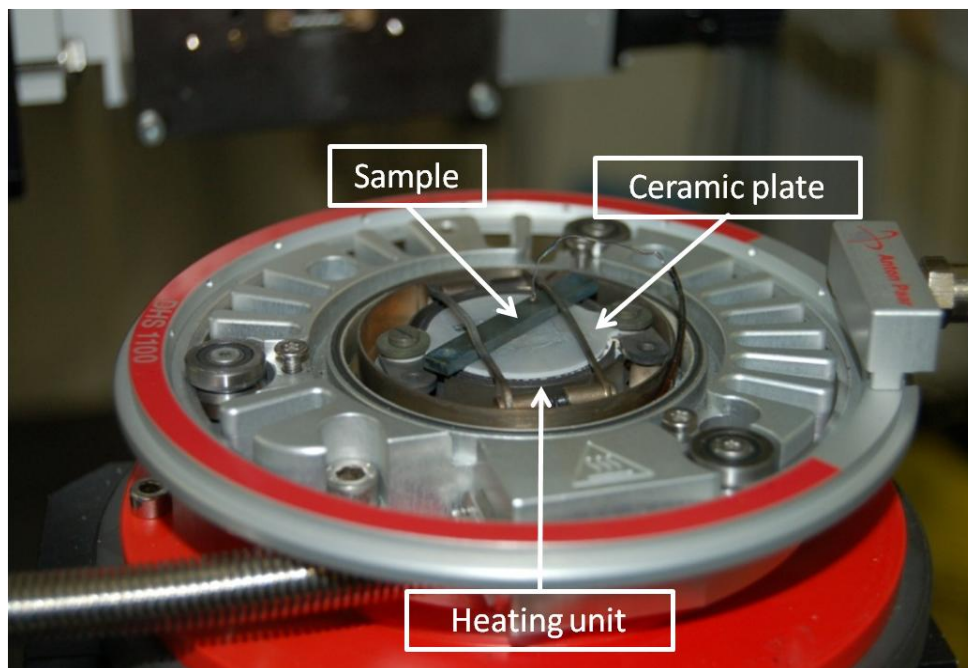


Figure 4-12: Photography of the specimen holder in the measurement chamber at the EDDI beamline. The cuboid sample is mounted in the centre of the specimen holder. Underneath the sample is the heating unit isolated from the sample with a ceramic layer

Two samples, hydrogen charged and uncharged reference sample were heated from ambient temperature to 625°C at a constant temperature ramp of 8 °C/min. After reaching the desired temperature the samples were held at this temperature for further 30 minutes. This has been conducted in order to observe the diffusion processes that occur at such elevated temperatures. The procedure was applied to both samples in order to later

compare the behavior of the two samples and to isolate the influence of hydrogen upon the measurements results. The duration of each acquisition of a diffraction spectrum lasted a time period of about 20 seconds, in order to achieve a satisfactory intensity resolution. The acquisition of the diffraction line's positions from the obtained diffraction spectrums were executed as described in the previous section (Section 4.4.1). Subsequently the hydrogen influence upon the lattice was evaluated.

A further calculation of the measurement depth was feasible by applying the same procedure as stated in the previous section (Section 4.4.1).

4.5. Residual stress measurements using XRD

The method of using XRD for residual stress measurement and calculation is the so-called "sin²ψ" method. With this method, the changes of the inter-atomic spacing in orientations parallel to the sample's surface are measured, as illustrated in Figure 4-13.

The sample is rotated around the axis parallel to the incident X-ray beam for conducting measurements with different ψ angles (illustrated in Figure 4-14).

According to this method, the stress perpendicular to the surface σ₃₃ is assumed to be equal to 0, as this method actually calculates the value of σ₁₁-σ₃₃. The shear stresses σ₁₃=σ₃₁ and σ₃₂=σ₂₃ that are also correlated to this orientation are assumed to be equal to 0 as well. According to these conditions, and when stress is present in the sample, there is a linear relation between the strain values and the sinus square values of the tilt angle ψ (see Figure 4-13). This relation is deduced from Equation 4-2:

$$(4-2) \quad \varepsilon_{\phi\psi} = \left(\frac{1+\nu}{E} \right)_{(hkl)} \cdot \sigma_{\phi} \cdot \sin^2 \psi - \left(\frac{\nu}{E} \right)_{(hkl)} (\sigma_{11} + \sigma_{22})$$

And according to this equation the slope of the linear plot is:

$$(4-3) \quad \frac{\partial \varepsilon_{\phi\psi}}{\partial \sin^2 \psi} = \left(\frac{1+\nu}{E} \right)_{(hkl)} \sigma_{\phi}$$

Where σ_ϕ is to be the calculated stress, E is the elastic modulus of the respective to the relevant crystallographic plane (according to the hkl indices) and ν is the poisson ratio [173,174].

When the strain is described according to the following equation:

$$(4-4) \quad \varepsilon = \frac{d - d_0}{d_0}$$

According to this there is a linear relation between the interplanar spacing and the square sinus of the tilt angle ψ .

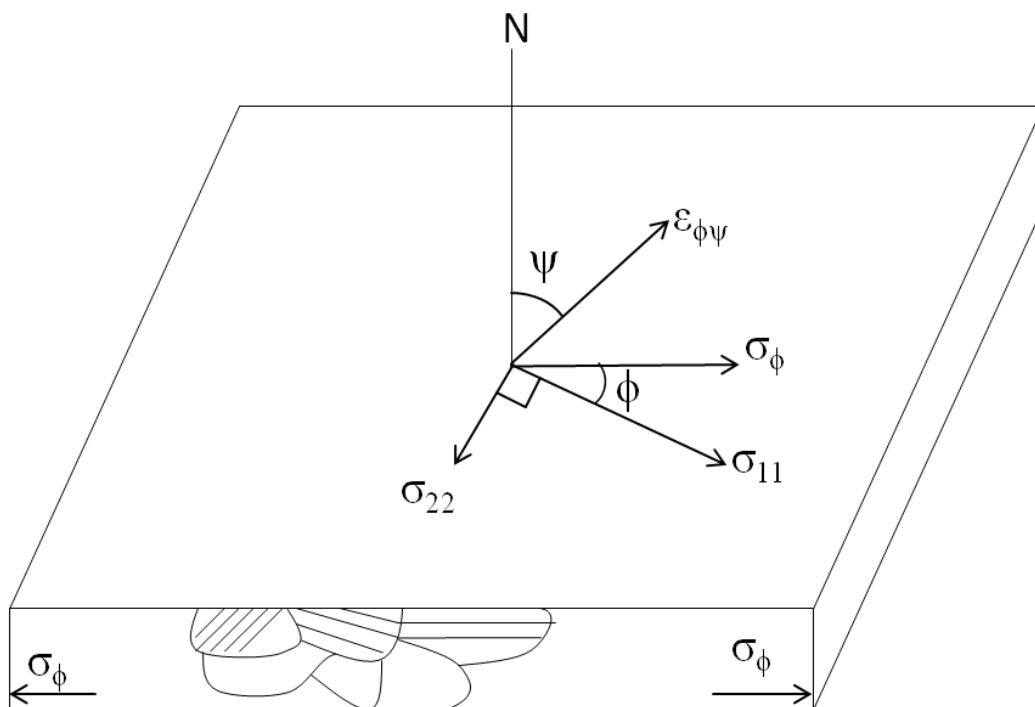


Figure 4-13: Schematic illustration showing diffraction planes parallel to the surface and at an angle $\phi\psi$. Note σ_{11} and σ_{22} both lie in the plane of the specimen surface (redrawn from Fitzpatrick [174])

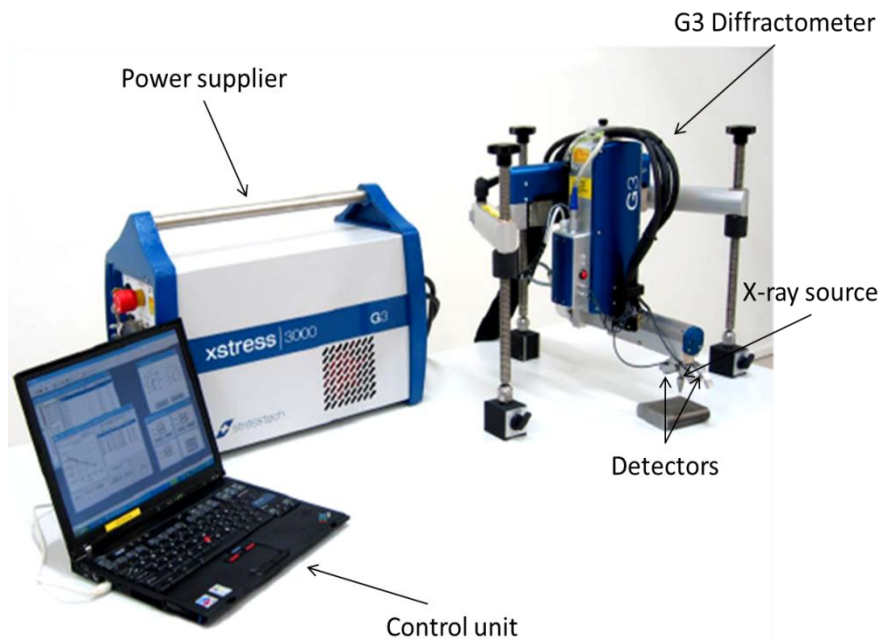


Figure 4-15: The G3 mobile diffractometer system for residual stresses measurement

4.5.2. Synchrotron radiation for residual stress measurements

Synchrotron X radiation with the energy dispersive diffraction technique has already been successfully used in order to measure in-situ the changes of residual stresses during various experiments and processes [170,175–179]. Genzel et al. showed the ability to use synchrotron radiation in order to observe residual stress formation during the growth process of thin films [170]. Kannengießner et al. showed the possibility to track and observe the residual stresses that evolve during a welding process [175,179]. The big advantage to using synchrotron radiation for residual stress measurement upon the usage of conventional, angle dispersive laboratory XRD devices is the ability to collect information simultaneously from several number of diffraction lines in opposition to the laboratory devices that can collect information only from a single line in a given measurement.

The influence of hydrogen upon the residual stress condition in the tested sample was examined with Energy Dispersive Diffraction (EDDI) beam line at the synchrotron facilities of the Helmholtz Zentrum in Berlin (HZB – BESSY II).

The residual stress measurements were conducted according to the $\sin^2\psi$ method. The measurements were set to 11 different ψ angles ranging from 0° to 89° . Each acquisition of

a diffraction spectrum lasted 20 seconds in order to achieve a sufficient intensity resolution of the diffraction lines without reducing the “in-situ character” of the experiment.

The interplanar spacing (d) was calculated with regard to the lines positions according to Bragg’s law, and it was plotted vs. $\sin^2\psi$. By linear fitting the plot using min square regression, one can calculate the magnitude of the residual stresses present in the sample, as described in Section 4.5.

4.6. Calculation of phase composition using X-ray Diffraction

Calculations of the phase composition from the obtained energy dispersive X-ray diffraction patterns were performed based on Laine’s work [180].

The principle of this model is that the phase content is somehow proportional to the integrated intensity of the phase’s lines.

The integrated intensity of a diffraction line, diffracted from a phase in a polycrystalline sample is expressed by:

$$(4-5) \quad I_{hkl} = CI_0(\lambda)\eta(\lambda)m|F_0|^2 \exp(-2M)\nu^{-2}\mu^{-1}(\lambda)\lambda^4V$$

Where I_0 is the intensity of the input beam, $\eta(\lambda)$ the quantum counting efficiency of the detector system, m is the multiplicity factor, F_0 the structure factor, ν the volume of a unit cell, $\exp(-2M)$ the temperature factor, $\mu(\lambda)$ the linear absorption coefficient, λ the wavelength corresponding to the interplanar spacing d_{hkl} and V is the volume fraction of the phase in the material.

If the sample has more than one phase, the intensity of each line is given by

$$(4-6) \quad I_{\alpha(hkl)} = CR_{\alpha(hkl)} \quad \text{and} \quad (4-7) \quad I_{\beta(hkl)} = CR_{\beta(hkl)}V_{\alpha}V_{\beta}$$

Where C is a constant parameter for specific hkl diffraction line due to the fixed geometry of the measurement (fixed position of the source, sample and detector), and

$$(4-8) \quad R = I_0(\lambda)\eta(\lambda)m|F_0|^2 \exp(-2M)\nu^{-2}\mu^{-1}(\lambda)\lambda^4$$

Where $I_0(\lambda)$ is the intensity of the beam, $\eta(\lambda)$ is the quantum counting efficiency of the detector, m is the multiplicity factor, F_0 the structure factor, ν the volume of a unit cell, $\exp(-2M)$ the temperature factor, $\mu(\lambda)$ the linear absorption coefficient, λ the correspondent wavelength of the hkl line and V the volume fraction of the phase in the material. Thus, for an alloy containing two phases it can be claimed that

$$(4-9) \quad \frac{V_\alpha}{V_\beta} = \frac{R_\beta I_{\alpha(hkl)}}{R_\alpha I_{\beta(hkl)}} \quad \text{and} \quad V_\alpha + V_\beta = 1$$

The phase composition can be thus calculated by measuring the integrated intensities of the diffraction lines and according to the diffracted beam wavelength.

4.7. Other experimental methods

4.7.1. Tensile test

For the inspection on the alloy's mechanical properties and the influence of hydrogen presence upon them an INSTRON tensile machine was used.

Tensile samples were prepared for this set of experiments according to the schematic illustration presented in Figure 4-16.

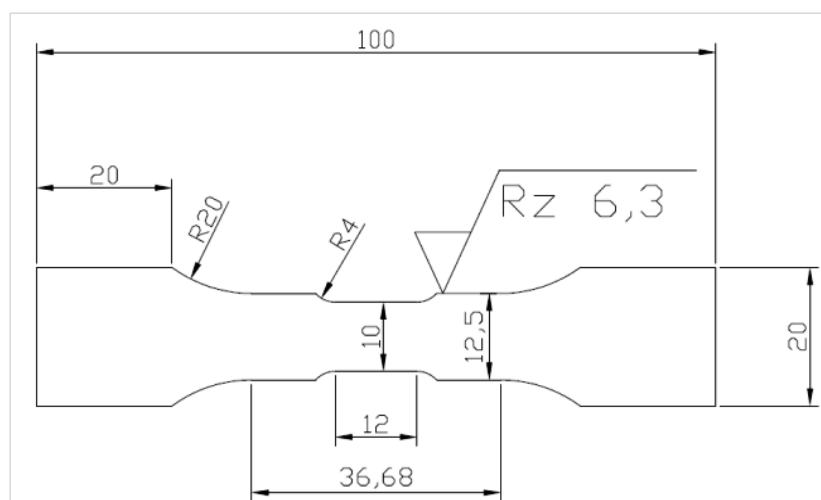


Figure 4-16: The geometry of the tensile specimens for HE analysis

The obtained stress strain curves of a hydrogenated sample and of an uncharged reference sample were compared in order to distinguish the mechanical properties differences between them and to assess the influence of hydrogen presence upon the mechanical properties of the tested material.

4.7.2. Optical microscopy

The microstructure of the studied material and the hydrogen influence upon it were studied using optic microscope. The sample preparation for that matter was conducted as the sample was grinded and polished up to level of 1 μm particle size of Alumina (Al_2O_3) and then was etched in a solution of: glycerin : HCl : HNO_3 in ratio of 3 : 2 : 1 for a duration of 60 seconds.

4.7.3. Scanning electron microscopy (SEM)

The microstructure and the surface analysis of the studied stainless steels were examined by means of SEM. The specimens were examined before and after hydrogen charging, in order to determine the influence of cathodic charging and hydrogen desorption on their microstructure. Preceding the SEM examination, the studied hydrogenated specimens were polished and etched in order to remove any by-products which were created during the charging process, and to achieve a proper image.

5. Results and discussion

5.1. Microstructural analysis

The basic microstructure of the studied alloy (SMSS), was examined by optical microscopy perpendicular to the rolling direction and parallel to the rolling direction, as presented in Figure 5-1 a and b, respectively. These optical images were obtained by applying the sample preparation procedure described in Section 4.7.2.

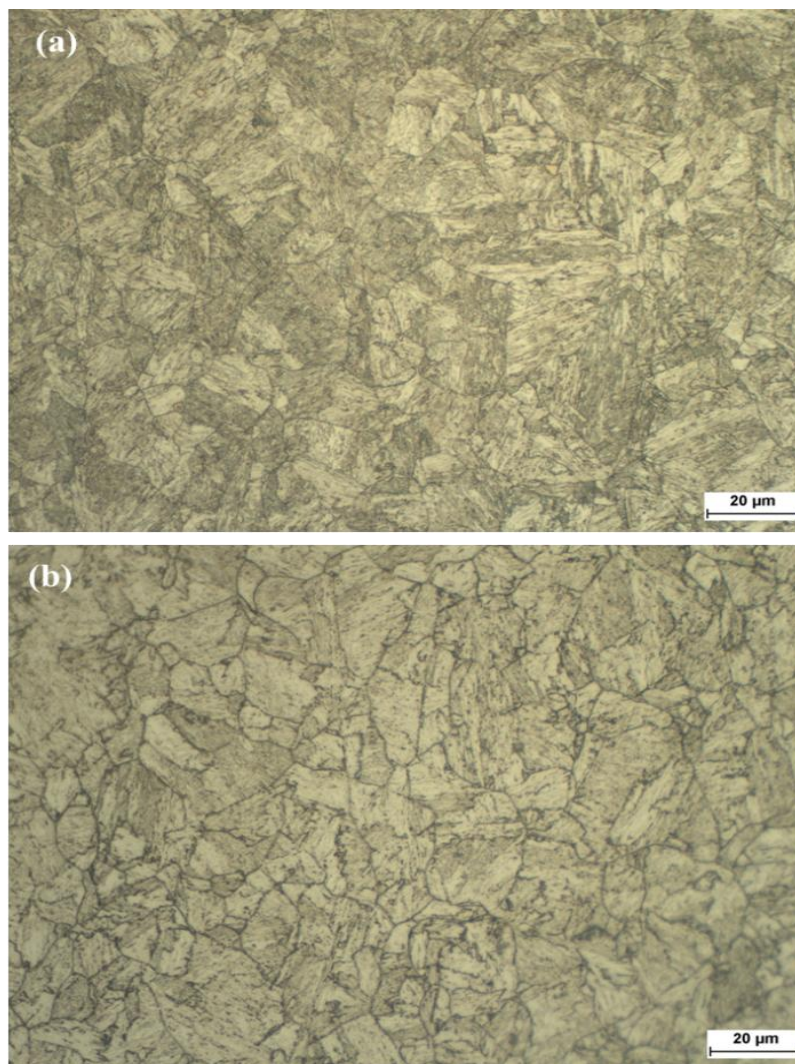


Figure 5-1: The microstructure of the as received material in the (a) perpendicular direction and in the (b) rolling direction

These images reveal mostly the structure of the former austenitic phase that was present in the sample prior to the quenching heat treatment.



Figure 5-2: SEM image of the studied SMSS, where the martensitic laths can be clearly seen (This image is perpendicular to the rolling direction)

A SEM image which clearly reveals the martensitic laths within the former austenitic grains is presented in Figure 5-2, and was obtained as well by applying the same etching procedure as was used for the optical microscopy.

It can be seen in these microscopic images, both optical and electron microscopy, that the examined material possesses the grain structure of the former austenitic phase former to the heat treatment. In addition, the material has an average grain size of about $20\mu\text{m} \pm 5\mu\text{m}$, as was statistically measured and calculated from the given images. The martensitic laths in this structure can be clearly seen in the SEM image within the former austenitic grains with the specific orientation of each grain.

In both optical and electronic microscopy it can be seen that there is no clear preferred orientation of the material's structure, despite the rolling process that was applied on the plate. The grains of the former austenitic phase seem to be isotropic orientated with no clear evidence of plastic deformation and reorientation as can be expected after the cold working of the steel plate. This lack of preferred orientation might be attributed to the fact that following the rolling process the steel plate was heat treated and annealed in a manner that disabled the effects of the mechanical processing and the induced plastic deformation.

One can assume that due to the discussed observations of the material's microstructure that the mechanical properties and the chemical properties (e.g. diffusion behavior) of the material are isotropic due to the lack of the preferred orientation of the material's structure.

5.2. HE of the tested alloy

In order to examine the influence of hydrogen presence upon the mechanical properties of the tested SMSS, two tensile specimens were tested. Both the samples were subjected to similar processing and possess the same dimensions as described in Section 4.7. One of the samples was hydrogen charged (to a concentration of about 6 wt. ppm) and the other remained in its "as prepared" condition for reference and comparison. The results of these tensile tests are presented in Figure 5-3.

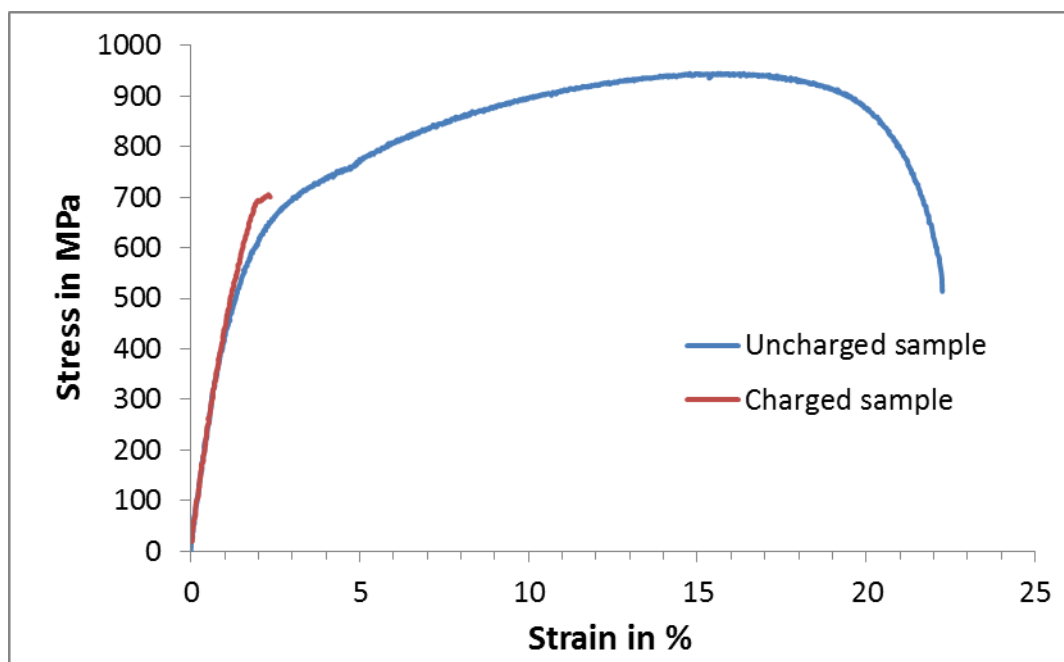


Figure 5-3: Tensile test results for a hydrogenated SMSS (red curve) and of an uncharged reference sample (blue curve) showing the drastic degradation of the ductility of the hydrogenated sample

It can be seen that a significant change of the stress-strain curve (a change of the mechanical properties) occurs with the presence of hydrogen, as summarized in Table 5-1.

Table 5-1: Summary of the mechanical properties of SMSS with and without the presence of hydrogen

	$R_{p0.2}$	U.T.S	Elongation
Reference	650 MPa	900 MPa	22%
Charged sample	700 MPa	700 MPa	2%

This change is mainly expressed in a severe degradation of the material’s ductility in terms of strain to fracture. The strain to fracture of the material is reduced from the 22% of the uncharged material to a mere 2% with the presence of hydrogen. In addition, it can be seen that the yield strength of the material is increased with hydrogen presence, as the yield strength around 650 MPa of the uncharged material is increased to a value of around 700 MPa in the charged condition. This indicates an increase of the material’s strength in the presence of hydrogen.

In order to comprehend the effect of hydrogen presence on the material’s severe loss of ductility, a metallographic examination of the charged specimen’s cross section was conducted using optical microscopy according to Section 4.7.2, as present in Figure 5-4. This examination was conducted directly after hydrogen charging without applying any external load to the sample.

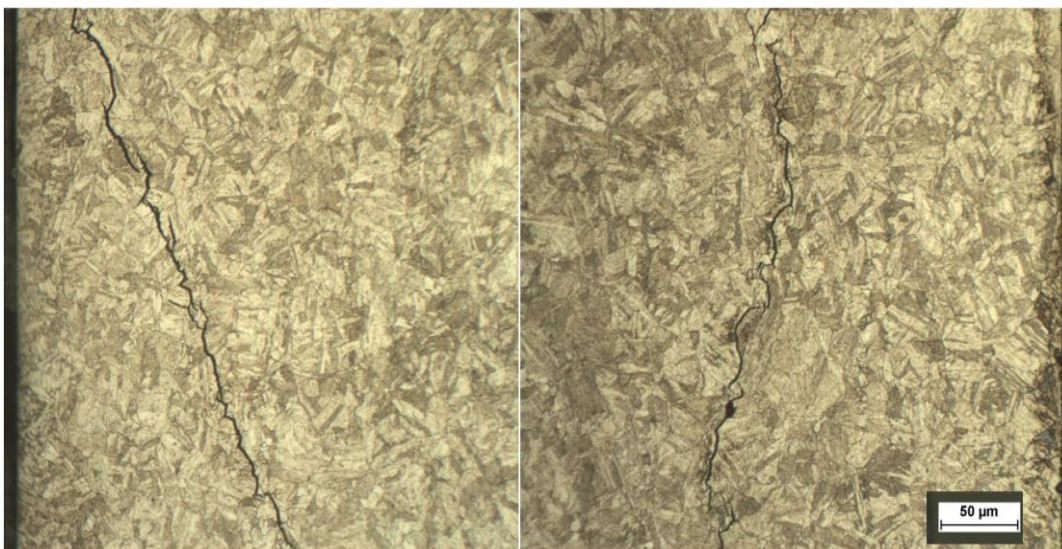


Figure 5-4: Identified cracks, appearing during hydrogen electrochemical charging in the microstructure of the SMSS

It is normally assumed that the presence of hydrogen in a component assists in the crack initiation and/or propagation, when external or internal loads such as residual stresses are present. However, it appears in this metallographic examination that the charging process itself, namely the electrochemical introduction of hydrogen into the sample may induce and initiate the cracking of a component, as cracks were detected in the specimen immediately after the electrochemical charging process. The cracks seemed to have an intergranular character and they were formed parallel to the sample' surface. It is assumed that the electrochemical charging process induced an extremely high partial hydrogen pressure on the surface of the sample and thus introducing a large amount of hydrogen atoms in the sample, which ingresses through an accelerated diffusion process from the surface into the sample's bulk. The inhomogeneity of the hydrogen content in the specimen due to this diffusion process induces large micro-stresses in the lattice due to the inhabitation of the interstitial sites and the tendency of the lattice to expand with the presence of hydrogen. The combination of the stresses and hydrogen presence allows the initiation of a crack parallel to the surface and normal to the direction of the concentration gradient, even in the absence of applied external loads on the component.

The presence of such intergranular cracks (seen in Figure 5-4) is certain to reduce the necessary stress for crack propagation, as the crack initiation step is skipped. Therefore the mechanical properties of the tested material are degraded and results in the premature failure of a serving component under lower stresses than the yield and tensile strengths.

5.3. Solubility of hydrogen in the tested material

For the determination of the maximal hydrogen solubility of the tested material a specimen, having the dimensions of $1 \times 5 \times 10 \text{ mm}^3$, was subjected to 144 hours (one week) of cathodic charging under the condition of current density of 20 mA/cm^2 . After the charging process the sample contained the concentration of 330 wt. ppm hydrogen, as was determined by the CGHE system (see Section 4.3) and presented in Figure 5-5.

The sample was degassed at more or less isothermal conditions of 900°C (1173K). The measurement was stopped when no further changes of the signal was recorded by the TCD. The extraction temperature of 900°C is sufficient for the effusion of all trapped (both reversibly and irreversibly) and diffusible hydrogen from the tested sample, as was determined by the standard ISO DIS 3690 [171]. It can be seen from the desorption curve

that the hydrogen effuses in one process as a single desorption peak appears. This observation suggests that at the aforementioned extraction temperature the trapped and diffusible hydrogen effuse at the same rate. Reasons for this result most probably derive from the hydrogen diffusion in that temperature which is similar for both trapped and diffusible hydrogen as the thermal energy is leveled or higher with the activation energy for the de-trapping and diffusion of hydrogen. The early initiation of the peak after approximately 50 seconds can be attributed to the martensitic structure of the material. The martensitic matrix allows fast hydrogen diffusion and the very fine distribution of the austenitic phase allows fast de-trapping of the hydrogen from the austenitic phase and from its interfaces with the martensitic phase, which are counted as the main trapping sites in this material, as established by former investigations [27,181].

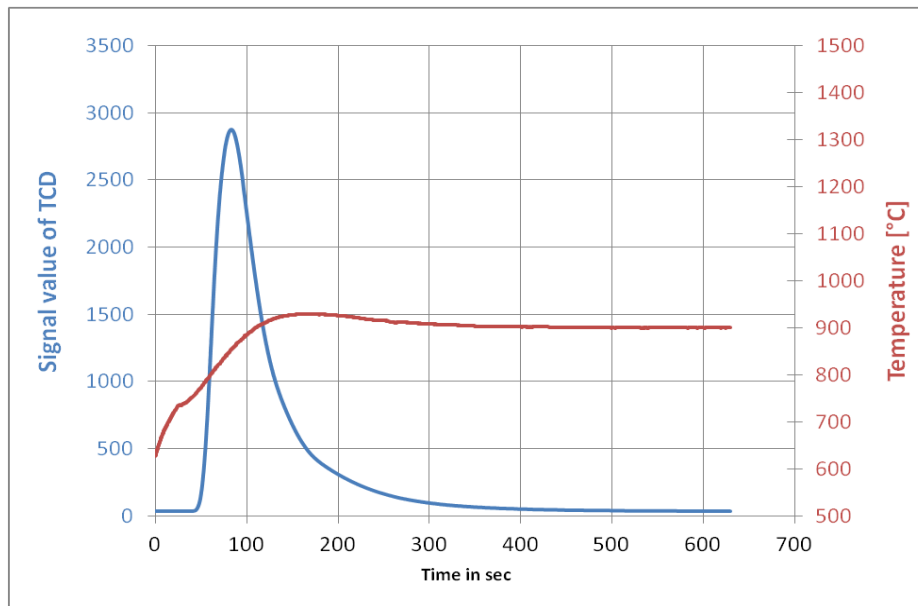


Figure 5-5: CGHE analysis at around 900°C for the super martensitic "as charged" sample

The relatively high hydrogen concentration (330 wt. ppm) in the sample could be also attributed to the martensitic structure of the material. The small austenitic "islands" between the martensitic laths act as trapping site for the hydrogen and it can be efficiently transported and distributed to these trapping sites due to the martensitic matrix which allows relatively fast diffusion of the hydrogen atoms.

5.4. Hydrogen desorption at room temperature

For the purpose of understanding the dynamics of the hydrogen desorption process at room temperature, in-situ EDXRD measurements were applied [182]. The measurements were performed upon a hydrogen saturated sample in order to observe and to analyze the effect of the hydrogen desorption process upon the crystal lattice of the material. Since diffusible hydrogen (also addressed as "solute hydrogen") expands the metal lattice the diffusion dynamics can be monitored through the changing of the atomic interplanar spacing of the material's crystal lattice.

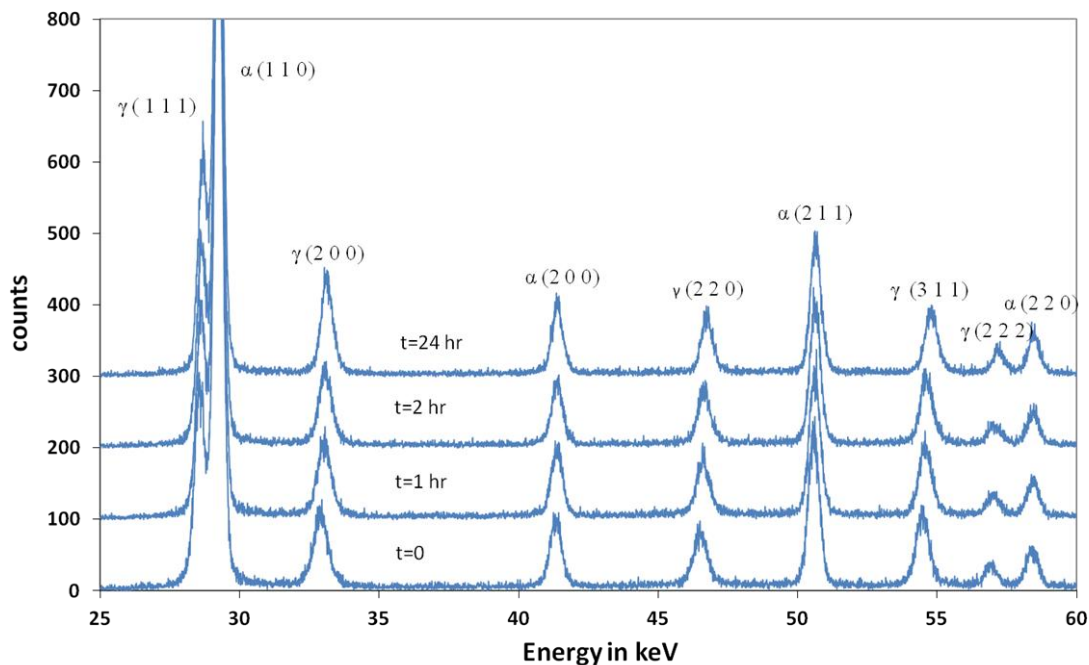


Figure 5-6: Energy dispersive X-ray diffraction spectrums, taken immediately after charging ($t=0$), after 1 hour of degassing at ambient temperature ($t=1$). After 2 hours and after 24 hours of degassing of the hydrogenated sample at ambient temperature ($t=2$ and $t=24$)

Figure 5-6 presents a few diffraction spectrums, obtained at different time intervals. It can be seen from these diffraction patterns that there is a slight shift of the diffraction lines towards higher energy levels with increasing time. The shift of the diffraction lines toward higher energy values is more pronounced in the case of the diffraction lines indicating the austenitic phase of the investigated microstructure (indicated with the sign γ). This is attributed to the higher hydrogen solubility in the austenitic phase compared to the martensitic/ferritic one, as will be shown and proved later in this section. The shift of the

diffraction lines indicates in principle the shrinkage of the atomic interplanar spacing in the lattice of each of the examined phases, both ferritic/martensitic and austenitic as hydrogen is desorbed from the sample.

For further analysis of these results the exact positions of the diffraction lines on the energy axis were extracted from all of the obtained diffraction patterns (Two diffraction patterns per minute in a time period of 2.5 hours). The extraction of the diffraction lines positions has been performed by fitting every line in the diffraction patterns to the Pseudo-Voigt Function. For this purpose the seven first lines ($\gamma(1\ 1\ 1)$ $\alpha(1\ 1\ 0)$ $\gamma(2\ 0\ 0)$ $\alpha(2\ 0\ 0)$ $\gamma(2\ 2\ 0)$ $\alpha(2\ 1\ 1)$ and $\gamma(3\ 1\ 1)$) were chosen, since these present the most distinguishable lines in the diffraction spectrums. The positions of the lines and their changes during the degassing process at ambient temperature are presented in Figure 5-7 and Figure 5-8 for the austenitic and the ferritic phases respectively. It should be mentioned that the large scattering in the positions are typical, and are attributed to fitting errors and an inexact match of the diffraction line's curve to the Pseudo-Voigt Function.

It can be clearly seen from these figures that the diffraction lines shift toward higher energy values (position on the x axis) during degassing of hydrogen at ambient temperature. Due to the in-situ characteristic of the measurement procedure, the dynamics of this shift can be characterized. It becomes apparent from the first observations that the shift of the diffraction lines is steep in the beginning of the process and moderates with increased time. This tendency will be analyzed in detail later in this section.

After the acquisition of the lines positions on the energy axis, the energy values were converted to atomic interplanar spacing, in accordance with the crystallographic plane Miller indices. This conversion was performed according to Bragg's Law (as described in Section 2.7 and Equation 2-3);

For energy dispersive diffraction the wavelength of the electromagnetic wave is converted to energy values thus the Bragg's law is represented as:

$$(5-1) \quad d(E) = \frac{hc}{2 \sin \theta} E^{-1}$$

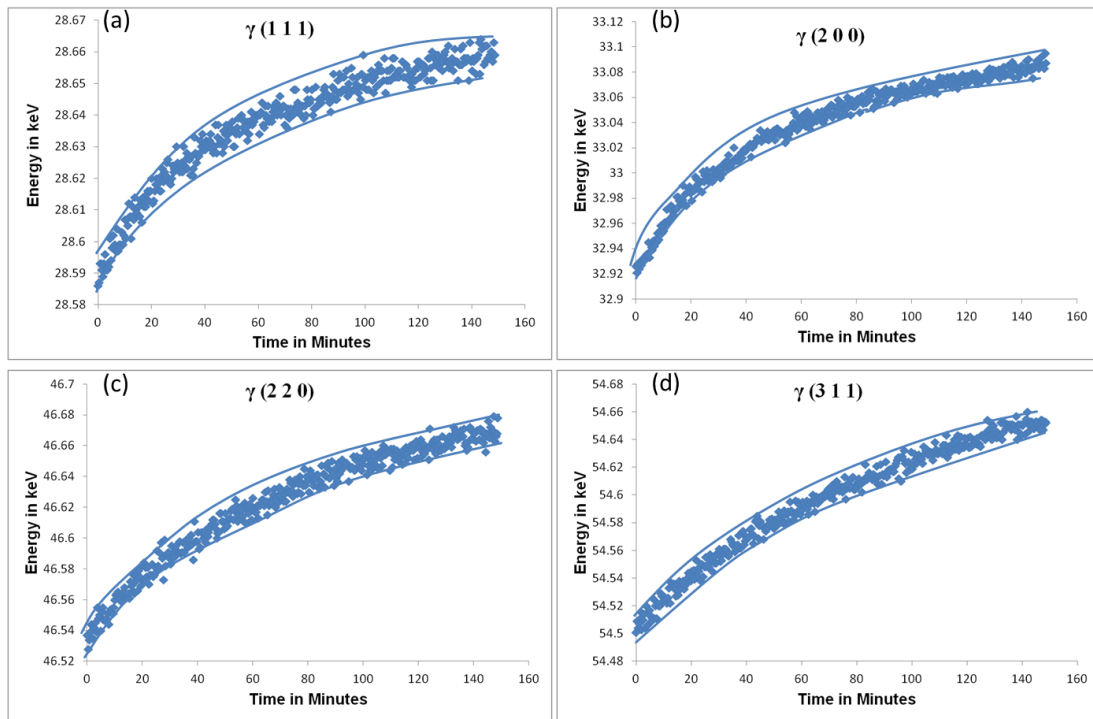


Figure 5-7: The changing of the line's positions during degassing at room temperature of the austenitic phase related lines (a) γ (111) (b) γ (200) (c) γ (220) (d) γ (311)

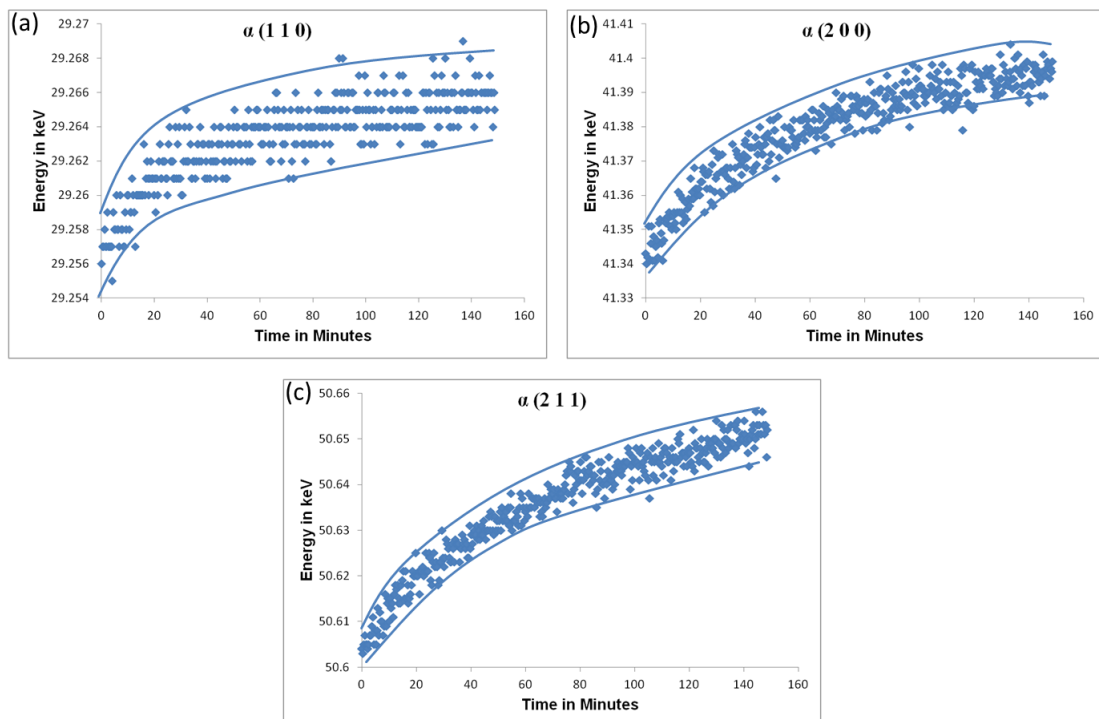


Figure 5-8: The changing of the line's positions during degassing at room temperature of the ferrite/martensite phase related lines (a) α (110) (b) α (200) (c) α (211)

From the acquired values of interplanar spacing one can calculate and convert this values and the measure the size of the lattice parameter of the examined phase according to the Miller indices hkl and according to the following formula (based on geometrical principles):

$$(5-2) \quad a_{(hkl)} = d_{(hkl)} \cdot \sqrt{h^2 + k^2 + l^2}$$

The calculated values of the lattice parameter have been assigned to Figure 5-9 and Figure 5-10 for the austenitic (γ) and ferritic/martensitic (α') related lines, respectively. These diagrams clearly exhibit the changes of the lattice parameter according to the shift of the lines positions during the hydrogen degassing process.

The expanded lattice parameter of the hydrogen charged samples, observed at the initial stage of the measurement, is attributed directly to the dissolved hydrogen atoms in the metal matrix. The relation between the hydrogen content and the lattice expansion is assumed to be linear in this material, since this relation has been proven previously for ferrous alloys and other metallic materials [183].

The contraction of the lattice, as a result of hydrogen effusion, shows a steep slope in the beginning of the process and moderates with further hydrogen effusion. This observation strengthens this examination's basic assumption that the lattice parameter is controlled solely from the hydrogen concentration, and its changes are controlled from the hydrogen effusion. Since hydrogen effusion rate is dependent on the hydrogen concentration gradient in the sample, the effusion rate is always higher in the beginning on the process and it declines with the time and with lower hydrogen concentration.

It can be claimed that the contraction of the lattice has a more or less exponential characteristic due to continuous decrease of hydrogen concentration. The effusion process of hydrogen from the material can be explained with the help of Sievert's law. The hydrogen partial pressure in the atmosphere is equal to zero, and consequently the hydrogen concentration at the surface area approaches zero as well. This induces a hydrogen concentration gradient ranging from the material's surface to the material's bulk. The hydrogen atoms diffuse in the direction of the smaller concentration and consequently out of the material. With increasing time the hydrogen concentration in the material decreases and

so is the concentration gradient. Since the effusion rate depends on the concentration gradient it decreases as well.

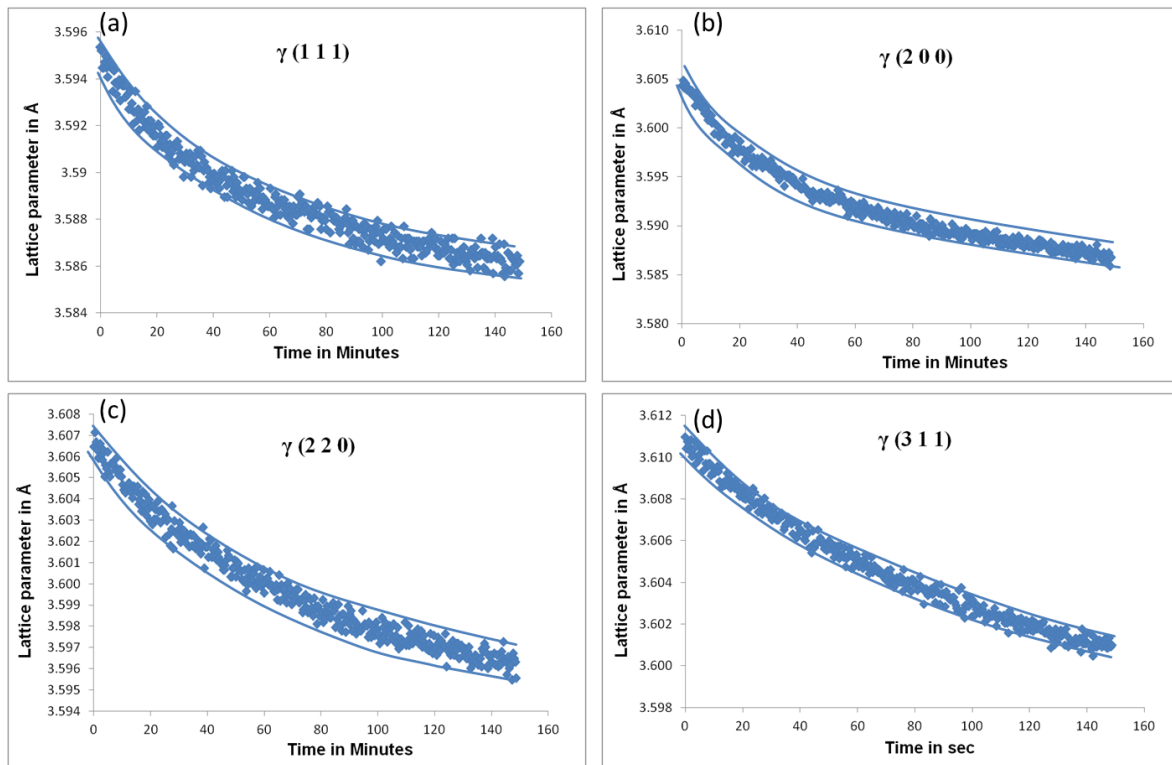


Figure 5-9: The lattice parameter changes of the austenitic phase during degassing of a hydrogenated sample at room temperature (a) $\gamma(111)$ (b) $\gamma(200)$ (c) $\gamma(220)$ (d) $\gamma(311)$

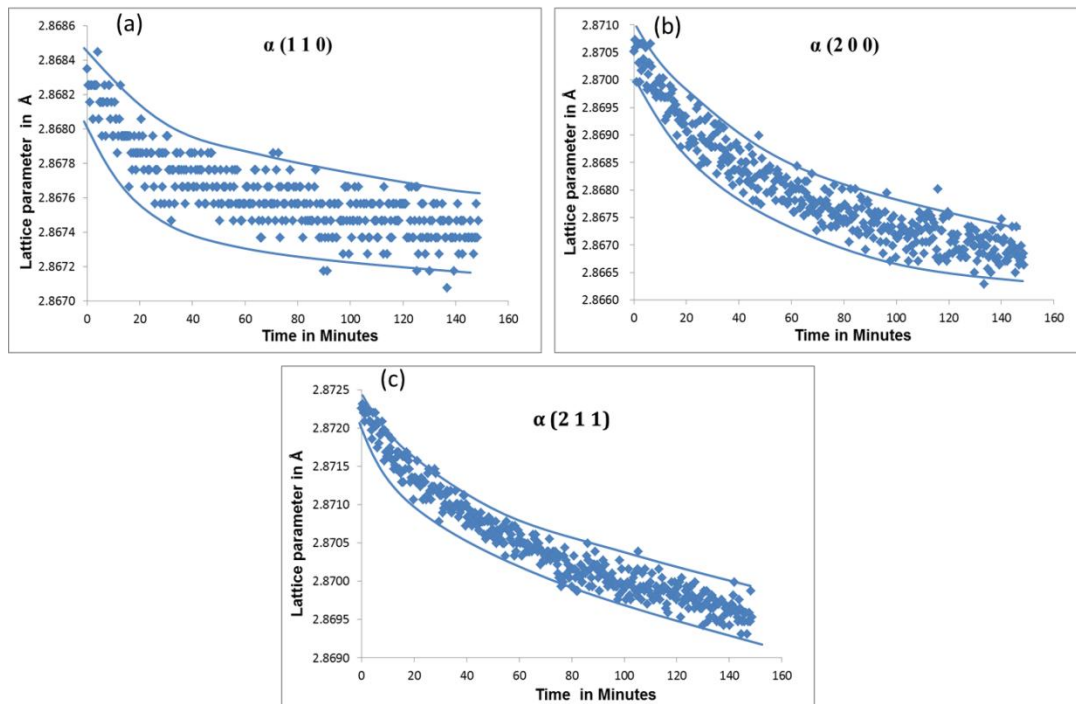


Figure 5-10: The lattice parameter changes of the ferritic/martensitic phase during degassing of a hydrogenated sample at room temperature (a) $\alpha(110)$ (b) $\alpha(200)$ (c) $\alpha(211)$

From the comparison of the diagrams in Figure 5-9 and Figure 5-10, such kinetics can be observed for each one of the examined crystal plane in each of the examined phases.

In order to evaluate the lattice diffusion coefficient according to the obtained curves in Figure 5-9 and Figure 5-10, the results were fitted to the solution of second Fick's law under the conditions of effusion as presented in Equation 5-3 and in the example in Figure 5-11.

$$(5-3) \quad C(x,t) = C_s - (C_s - C_0) \cdot \operatorname{erf}\left(\frac{x}{2\sqrt{Dt}}\right)$$

Where $C(x,t)$ is the given concentration at a certain time and depth in the sample, C_0 is the initial hydrogen concentration in the sample, C_s is the hydrogen concentration on the surface of the sample, x is the depth in the sample (distance from the surface), D is the corresponding diffusion coefficient and t is the time.

First, the values of the lattice parameter were converted to values of hydrogen concentration according to the initial value (directly after charging) and the end value (after 2.5 hours of degassing at ambient temperature) as measured with CGHE.

Equation 5-3 describes the concentration dependency on the location and effusion time. Since the location (depth) of the collected data for each diffraction line can be calculated in accordance to its energy, this equation represents the changes of the concentration as a function of the effusion time. Fitting this equation to each of the effusion plots can yield the hydrogen diffusion coefficient.

The fit curve, presented in Figure 5-11, exhibits a slight time delay at the beginning. This delay is originated by the fact that the EDXRD measurement is conducted at a certain depth in the sample (4 μm in the present example). Since the initial hydrogen distribution is assumed to be homogeneous through the sample, there is no concentration gradient at the measurement depth at the very beginning of the effusion process. This delay corresponds to the time from the start of effusion at the sample's surface until the buildup of a concentration gradient at the measurement depth and the consequent effusion in this location.

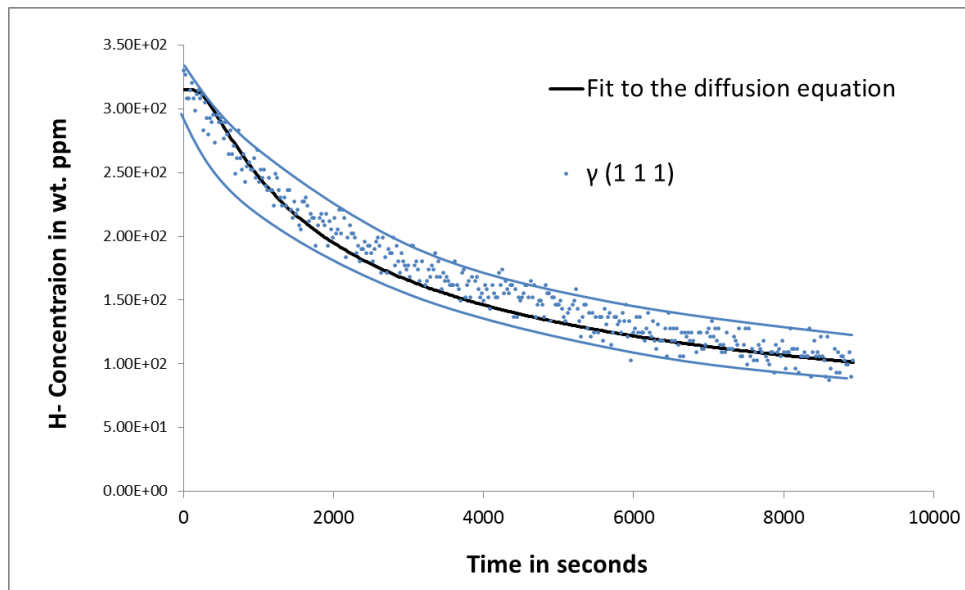


Figure 5-11: Fitting of the effusion curve to the solution of Fick's second law

The calculated diffusion coefficients for each of the in Figure 5-9 and in Figure 5-10 given curves are summarized in Table 5-2.

Table 5-2: Calculated diffusion coefficients from the effusion curves

Lattice plane	D in mm ² /sec	Lattice plane	D in mm ² /sec
γ (1 1 1)	5.21×10^{-9}	α (1 1 0)	7.68×10^{-8}
γ (2 0 0)	1.27×10^{-9}	α (2 0 0)	5.54×10^{-8}
γ (2 2 0)	3.85×10^{-8}	α (2 1 1)	1.11×10^{-7}
γ (3 1 1)	1.39×10^{-7}		

It can be seen from this table that the calculated hydrogen diffusion coefficients in the martensitic phase are about one order of magnitude higher than that of the austenitic phase. The values of the diffusion coefficients for both phases are in good agreement with values published in the literature by Böllinghaus et al. [9] and the obtained results of Seeger [99]. The calculated values in this contribution are located in the lower area of the scatterbands. This can be attributed to the fact that in this contribution the lattice diffusion was measured without any influence of other factors. Since diffusion at ambient temperature is usually not relying on lattice diffusion, it is reasonable that the lattice diffusion coefficient at ambient temperature is smaller than the effective diffusion coefficient.

Furthermore, according to published results in the literature, the difference between the diffusion coefficients of the two phases should be of about 3-4 orders of magnitude. It is known that austenite entails much higher trap density than the martensitic phase, especially in the form of dislocations and twinning defects. In addition, the austenitic phase contains high nickel concentration, which contributes to a low hydrogen diffusion coefficient in this phase. It can be assumed in accordance that those traps are responsible for the slow hydrogen diffusion in the austenitic phase which was measured in former studies, and the pure lattice diffusion in both phases is more or less similar. Since the EDXRD measurements are applied only to the lattice and only the changes of the lattice parameter due to hydrogen are measured, the influence of the traps on the obtained diffusion coefficients is not measured. This claim is reinforced from the scatterbands published by Böllinghaus et al. [9], showing that at higher temperatures the diffusion coefficients for ferritic/martensitic steels are comparable with those of austenitic steels. At elevated temperatures the reversibly trapped hydrogen (at dislocations and twinning defects in the case of austenitic steels) has high thermal energy and it acts as diffusible hydrogen.

The effective hydrogen diffusion coefficient of the material, calculated in accordance to 15% of retained and annealed austenite as was calculated by XRD, EBSD and TEM, yields the value of 7.6×10^{-8} mm²/sec. this value corresponds to the lower limits of the measured diffusion coefficients by Seeger (see Figure 2-8) [99]. The good agreement between the two measurement methods (electrochemical permeation and EDXRD) validates the reliability of EDXRD for measurement of phase specific diffusion coefficient in a multi-phase material.

Figure 5-12 and Figure 5-13 present the lattice parameter, calculated from the diffraction lines positions as they were measured after 24 hours of degassing of the sample at ambient temperature. This degassing time at room temperature for materials having body centered microstructure should be sufficient for desorption of the majority of the diffusible hydrogen [171].

These figures show that for both austenitic phase and ferritic/martensitic phase the energy values remain constant within a certain scatter indicating a steady state of the lattice parameter. This generally proves that nearly all hydrogen has been effused from the respective lattice after the mentioned time period and no further significant desorption process occurs afterwards. The calculated lattice parameter from the average value in these curves is presented in Table 5-3 along with the lattice parameter measured from the uncharged reference sample.

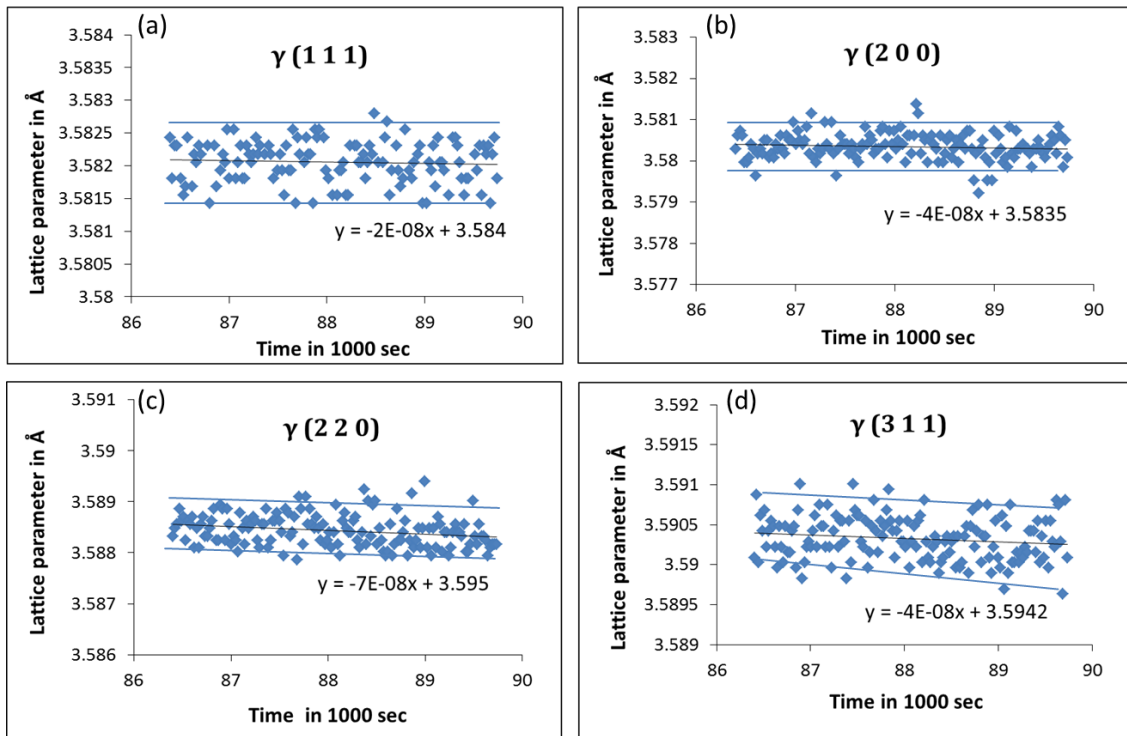


Figure 5-12: The line's positions related to the austenitic phase after prior degassing of 24 hours at room temperature (a) $\gamma(111)$ (b) $\gamma(200)$ (c) $\gamma(220)$ (d) $\gamma(311)$

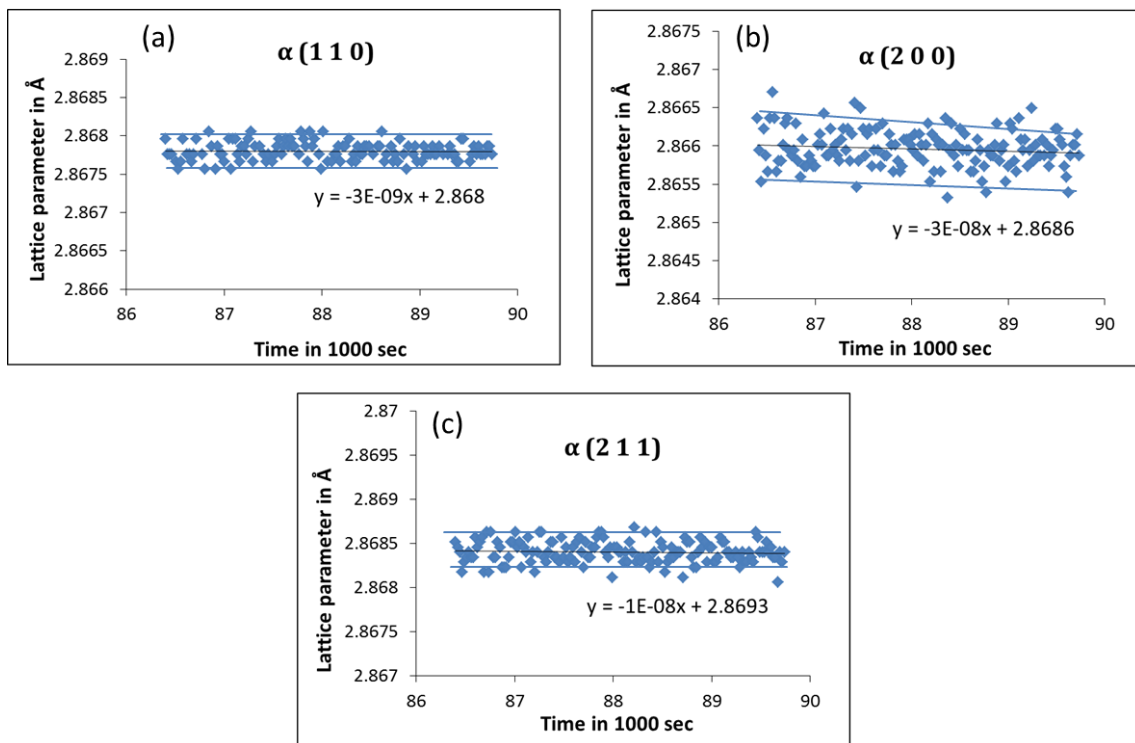


Figure 5-13: The line's positions related to the ferritic/martensitic phase after prior degassing of 24 hours at room temperature (a) $\alpha(110)$ (b) $\alpha(200)$ (c) $\alpha(211)$

Table 5-3: The calculated lattice parameter of both phases in the sample after degassing in room temperature for 24 hours and the lattice parameter of the uncharged material . The values were calculated from the average position of the lines on the X axis (Energy value)

Lattice plane	Uncharged lattice parameter in Å	Lattice parameter after degassing in Å	Lattice plane	Uncharged lattice parameter in Å	Lattice parameter after degassing in Å
γ (1 1 1)	3.579	3.582	α (1 1 0)	2.867	2.868
γ (2 0 0)	3.578	3.580	α (2 0 0)	2.866	2.866
γ (2 2 0)	3.583	3.588	α (2 1 1)	2.868	2.868
γ (3 1 1)	3.583	3.590			

By comparing the lattice parameter values of the hydrogen charged sample with those of an uncharged reference sample, it was found that the lattice of the first had not regained the original dimensions as of an uncharged sample. After degassing, the charged sample exhibited an expanded lattice parameter of the austenitic phase to a small extent.

It can be deduced that even after hydrogen desorption and stabilization of the lattice parameter value, some retained hydrogen remains in the material as solute hydrogen in interstitial sites, consequently inducing a slight lattice distortion. Moreover, the small extent of plastic deformation that occurred in the austenitic phase might be responsible for the respected irreversibility.

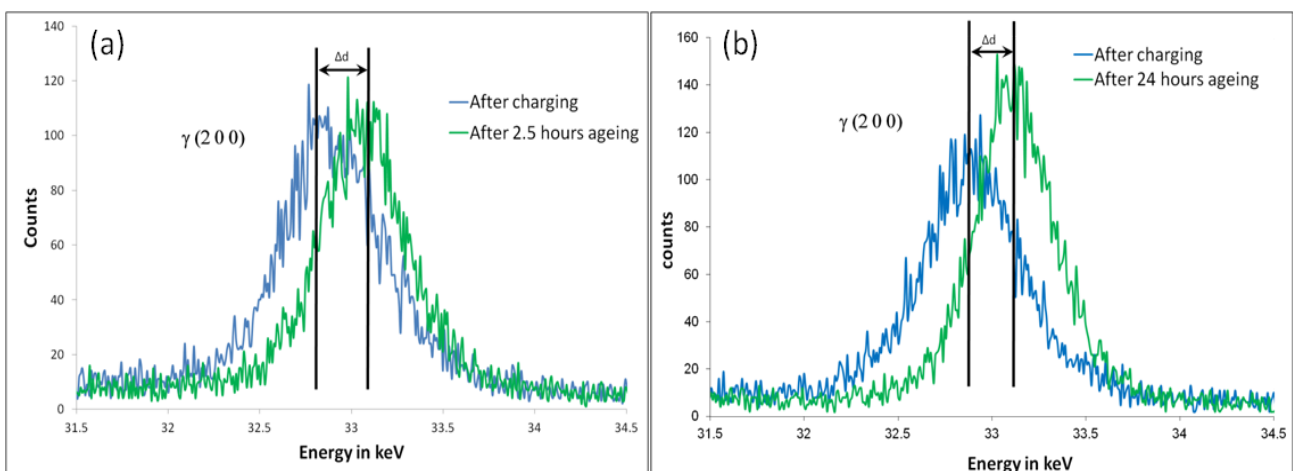


Figure 5-14: Illustration of the total shift of the austenitic diffraction line (2 0 0) during the degassing process at ambient temperature for (a) 2.5 hours and (b) 24 hours

The total shifts of the diffraction lines during effusion were calculated for the purpose of more explicit examination of the influence of orientation and depth upon hydrogen effusion. The corresponding changes of the interplanar spacing for each orientation during the examination process were calculated according to Bragg's law and presented in Table 5-4. For these calculations the distance between the initial line position (at the beginning of the experiment) and the final line position (at the end of the experiment) was measured as illustrated in Figure 5-14.

Table 5-4: Line shifts of the ferritic and austenitic phases

Austenitic phase				Ferritic/martensitic phase			
h k l	Depth of collected data [μm]	Δd after 2.5h [m]	Δd after 24h [m]	h k l	Depth of collected data [μm]	Δd after 2.5h [m]	Δd after 24h [m]
(1 1 1)	4.07	$5.63 \cdot 10^{-13}$	$7.79 \cdot 10^{-13}$	(1 1 0)	4.44	$5.79 \cdot 10^{-14}$	$6.23 \cdot 10^{-14}$
(2 0 0)	5.94	$9.46 \cdot 10^{-13}$	$1.22 \cdot 10^{-12}$	(2 0 0)	11.39	$2.22 \cdot 10^{-13}$	$2.38 \cdot 10^{-13}$
(2 2 0)	15.39	$4.12 \cdot 10^{-13}$	$6.55 \cdot 10^{-13}$	(2 1 1)	19.99	$1.23 \cdot 10^{-13}$	$1.59 \cdot 10^{-13}$
(3 1 1)	22.82	$3.17 \cdot 10^{-13}$	$6.17 \cdot 10^{-13}$				

It can be seen from the calculated values that the changes of the interplanar spacing in the ferritic/martensitic (α') phase is significantly smaller than that of austenitic (γ) phase. This observation reinforces the existent knowledge about hydrogen solubility in different microstructures. The hydrogen solubility in austenite (FCC microstructure) is about four to five orders of magnitude larger than the hydrogen solubility in ferrite (BCC microstructure) and martensite (BCT microstructure) [184–186]. This characteristic is attributed to the dimensions of the interstitial sites in the FCC structure, mostly the octahedral ones with the size of about 15% of the lattice parameter, which are generally larger than the interstitial sites in the BCC and/or BCT microstructures with the maximal size of 13% of the lattice parameter as shown and explained in prior Section 2.2 and illustrated in Figure 2-2.

From the values of the shifts of the diffraction lines, which were converted to changes of the lattice parameter, the maximal lattice strains for each orientation and corresponding depth were calculated according to the following equation:

$$(5-3) \quad \varepsilon = \frac{d_1 - d_0}{d_0}$$

Where ε is the strain, d_0 is the interplanar spacing of the lattice after hydrogen effusion (regarding to the inter-planar spacing value calculated after 24 hours of degassing at ambient temperature) and d_1 is the interplanar spacing of the fully charged sample. The strains were calculated according to the atomic interplanar spacing value in the beginning of the measurement, where it was maximal directly after the electrochemical charging process and the interplanar spacing after 24 hours of degassing where no more changes of the lattice parameter were observed. The values of the total strains, calculated for each of the examined diffraction lines are presented in Figure 5-15 as a function of the depth of the collected data. The depth of the collected data was calculated in accordance to the line's energy value as described in Section 4.4.1.

From a comparison of the strain values of the austenitic and the martensitic phases (presented in Figure 5-15 a and b, respectively) it can be deduced that the straining of the ferritic/martensitic (α) phase is by a factor between 3 and 5 smaller than in the austenitic (γ) phase which is also reflected by the values listed in Table 5-4. This has to be attributed to the fact that the hydrogen solubility in the austenitic (γ) phase is generally much higher than in the ferritic/martensitic (α) phase. These observations also indicate that the dissolved hydrogen is actually physically affecting the austenitic (γ) lattice to higher extent than the ferritic/martensitic (α) lattice, as the lattice of the austenitic phase is subjected to a higher extent of distortion.

From the analysis of hydrogen induced strains as a function of the depth inside the sample (Figure 5-15) it can be seen that the strain is relatively low at the area near the surface (at about 4 μm deep below the surface), increases further inside the sample and then decreases again further at deeper depths in the sample's bulk. This tendency is observed for both the austenitic (γ) and the ferritic/martensitic (α) phases. This may tentatively be attributed to a fast effusion of hydrogen from the surface during the early stages of the experiment, namely in the time period of a few minutes between the end of the electrochemical charging and the beginning of the EDXRD measurements.

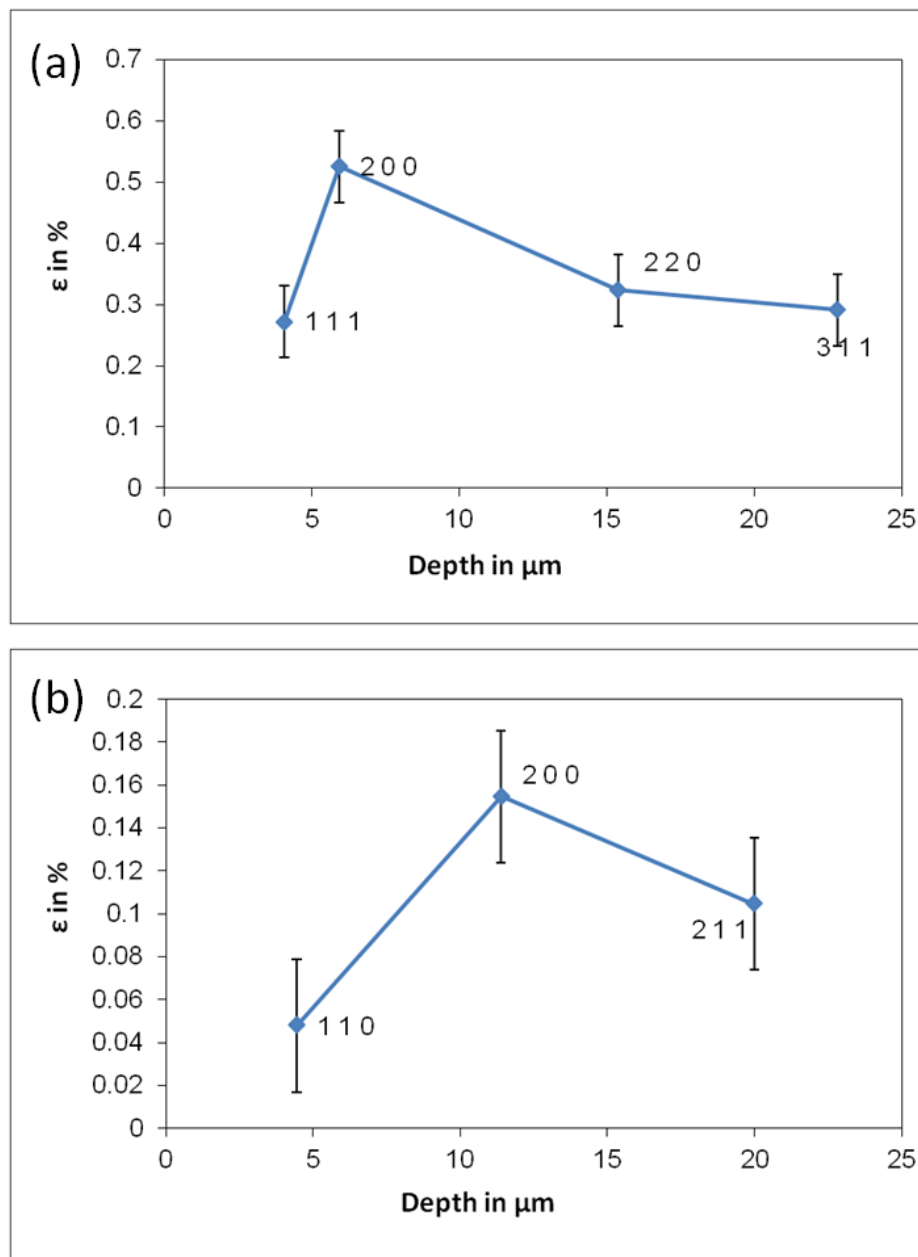


Figure 5-15: The maximum lattice strain induced by hydrogen on the (a) austenitic and the (b) ferritic/martensitic phase

The small extent of lattice parameter changes in the sample's bulk compared to the near surface area is attributed probably to inhomogeneity of the hydrogen distribution in the sample, namely lower hydrogen concentration in the sample's bulk than at the near surface region. It is assumed that an exponential hydrogen concentration profile exists and is ranging from the sample's surface toward the bulk. Since the hydrogen from the surface layer effuses almost immediately, a peak of hydrogen concentration appears just below the surface layer. For this reason the highest hydrogen concentration in the very beginning of

the measurements is located at the layer underneath the surface. After the degassing process and desorption of diffusible hydrogen it is assumed that only a small amount of retained hydrogen is homogeneously distributed in the sample.

This explains the strain differences in different depths as shown in Figure 5-15. Furthermore, it can be seen from the values of the hydrogen induced lattice strains that those exhibit very low values of maximal 0.16% in the ferritic/martensitic phase and values of around 0.5% in the austenitic phase. As known, the yield point of a metallic material is considered to be located at 0.2% of elongation. Therefore it can be deduced that the austenitic phase undergoes a plastic deformation to some extent during the electrochemical hydrogen charging procedure and ingress of hydrogen in the lattice. Plastic deformation process is accompanied with enhanced dislocations emission and movement. An enhanced dislocations presence induces a permanent distortion of the lattice due to the stress accumulation around the dislocations. This assumption is also supported by the examination of the diffraction line's broadness related to the austenitic phase. The changes of the diffraction line's broadness during the degassing process are shown in Figure 5-16.

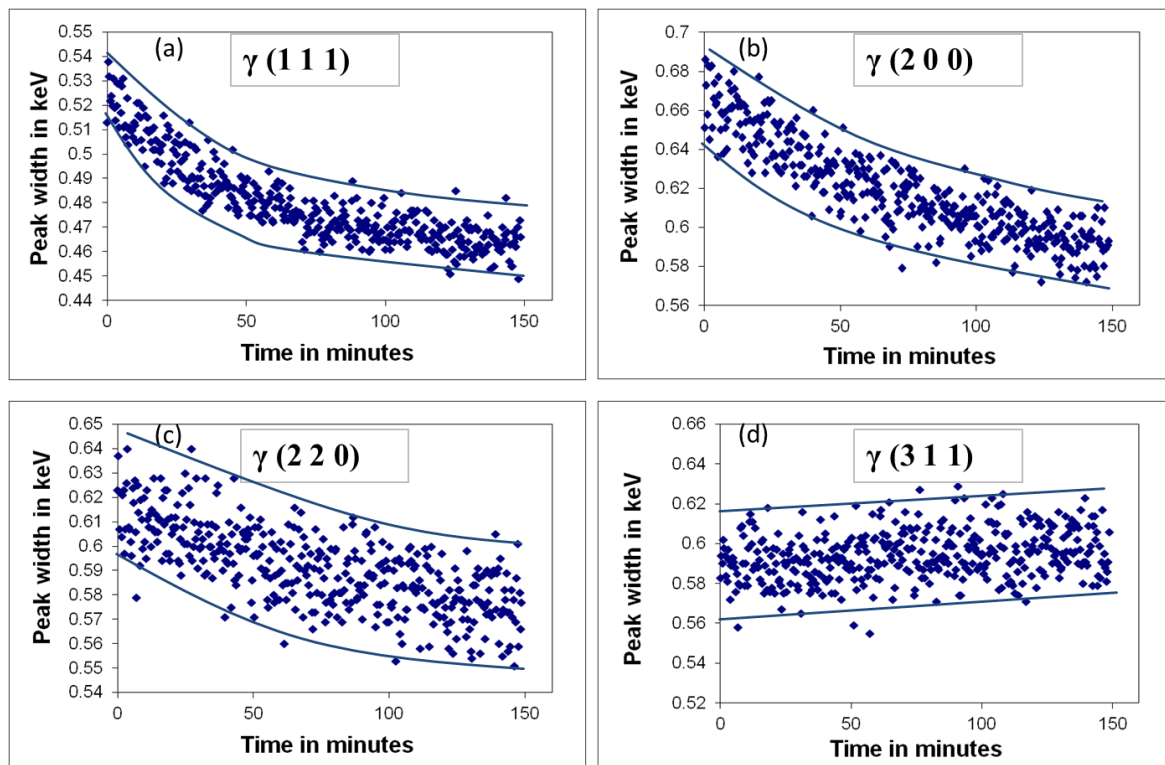


Figure 5-16: The changes of the broadness of the diffraction lines correlated with the austenitic phase (a) $\gamma(111)$ (b) $\gamma(200)$ (c) $\gamma(220)$ (d) $\gamma(311)$

It can be seen in this figure that the broadness of the austenitic diffraction lines is large in the beginning of experiment and decreases as hydrogen desorbs from the sample. The broadness of the diffraction lines indicates the homogeneity of the inter-planar spacing in the examined volume. As broader the diffraction lines are, the more inhomogeneous is the inter-planar spacing dispersion in the examined volume. Plastic deformation and enhanced dislocations emission is a cause of inhomogeneity of the lattice parameter and consequently a broader diffraction line. The enhanced emission of dislocations distorts the lattice and causes the inhomogeneity of the inter-planar spacing.

Calculations of the phase composition and its changes during the degassing and hydrogen desorption process are presented in Figure 5-17. These calculations were performed for each of the obtained diffraction patterns according to Laine as described in Section 4.6 [180]. It was performed by calculating and comparing the area below the diffraction line of the seven first lines; four of the austenitic phase and three of the ferritic/martensitic phase and deriving the average value from these twelve comparisons.

The calculated martensite content in the tested sample is about $62\% \pm 8\%$. These calculations indicate that the martensitic and austenitic phase content remained more or less constant during the process of hydrogen desorption at room temperature (total change of 0.5% of the martensitic content).

The large deviation of the EDXRD calculated values from the martensite content measured by EBSD and laboratory XRD is originated probably from the anisotropy of the sample's grains at the surface area. This anisotropy was most likely caused by the plastic deformation that was induced during the sample preparation procedure, i.e. machining and grinding. Since the calculation of the phase composition according to Laine is associated with isotropic materials (ideally powder), the calculated values in this case are accompanied with this relatively large standard deviation.

The calculation of the phase composition in the uncharged reference sample, performed by EDXRD as well, revealed the value of $55\% \pm 7\%$ martensite content in the tested volume. It can be stated according to this result that some extent of hydrogen induced phase transformation occurred in this steel during the hydrogen charging/ingress process. This can be attributed to the fact that hydrogen atoms presence in ferrous materials reduces the stability of the austenitic phase and consequently promoting martensitic transformation of this phase [12,187–189]. This observation is reasonable, since the

present austenitic phase in the studied material is referred to as retained and annealed austenite. During the process of hydrogen introduction into the material, stresses build up due to the formation of hydrogen concentration gradient. This gradient induces differences of the lattice parameter which inflict tensile and compressive stresses. These stresses combined with the reduction of the stability of the austenitic phase might eventually lead to austenite to martensite phase transformation as well as the initiation of cracking, as was intensively studied before [44,46,49,51,190–192] and showed in Section 5.2.

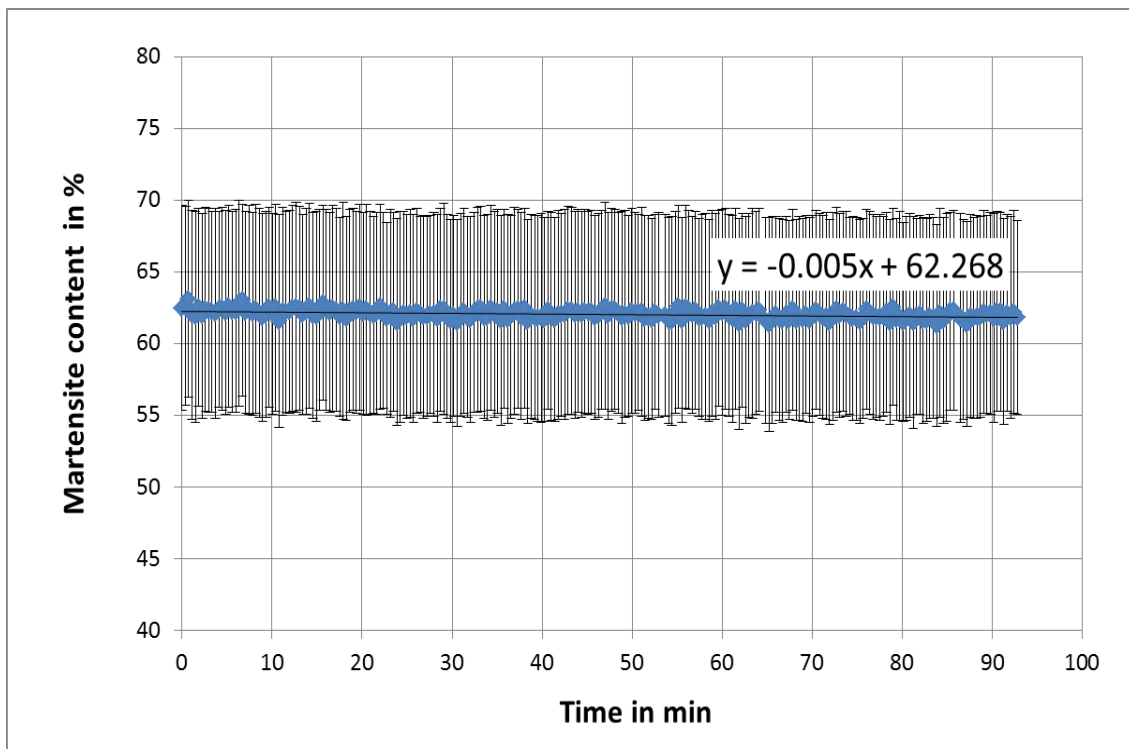


Figure 5-17: The martensite phase content in the sample during hydrogen desorption. the martensite content was calculated in accordance to Laine

5.5. Hydrogen desorption during continuous heating

In order to examine the influence of hydrogen desorption upon the lattice of SMSS during continuous heating process, a hydrogen charged sample was subjected to heat treatment and the changes of the diffraction patterns were examined by means of EDXRD method [193].

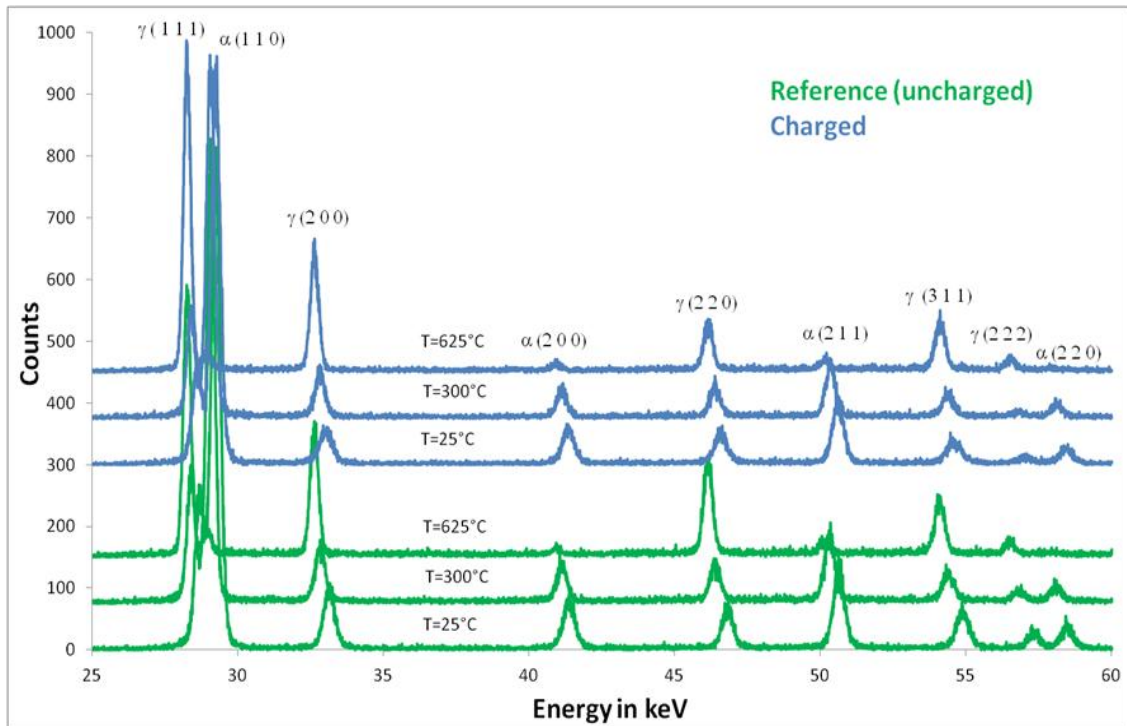


Figure 5-18: Example of the obtained diffraction spectrums collected at 25, 300 and 625°C for a hydrogenated sample and a reference uncharged sample

Figure 5-18 present a few representative diffractions patterns that were obtained during heating of a hydrogenated SMSS sample and an uncharged reference sample at a constant heating rate of 8°C per minute up to 625°C. The obtained diffraction patterns reveal a distinguishable shift of all obtained diffraction lines for both phases austenitic and ferritic/martensitic toward lower energy values during the heating process, i.e. at higher temperatures the positions of all of the diffraction lines were shifted toward lower energy values. In addition, it can be also seen from this figure that the intensities of the diffraction lines correlated to the austenitic phase were increased with higher temperatures while the intensities of the lines correlated to the ferritic/martensitic phase were decreased with higher temperatures. These mentioned effects will be discussed in this section separately and in detail.

The shift of the diffraction lines toward lower energy values can be generally attributed to the thermal volumetric expansion of the metal lattice. In order to further analyze and quantify these observations, the exact positions of the diffraction lines were determined by the application of the diffraction curve to a Pseudo-Voigt function in the same manner as was done in the previous section (Section 5.4). The obtained energy values (corresponding

to the diffraction line's position on the X axis in the diffraction pattern) were then converted to atomic interplanar spacing and respectively to lattice parameter in accordance to Bragg's law and by applying Equation 5-3. The calculated lattice parameters for all diffraction lines, obtained for both the hydrogenated sample and the uncharged reference sample have been plotted as a function of the temperature and are presented in the Figure 5-19 and Figure 5-20 for the austenitic and ferritic/martensitic phases, respectively. In general, thermal lattice expansion can be observed for both the hydrogenated and the reference samples in all of the examined orientations and depths. This thermal expansion is more or less linear proportional to the temperature.

The most significant difference of the line's positions, i.e. lattice parameters, between the charged and uncharged samples is observed mainly in the beginning of the heating process. This difference can be better seen with diffraction lines that are correlated to the austenitic phase. It can be seen, that in the very beginning of the experiment there is a significant gap between the lattice parameter of the hydrogenated sample and the reference sample. The cause for these lattice parameter differences between the charged and uncharged samples is the presence of solute hydrogen in the lattice interstitial sites.

It can be further seen that the lattice parameter of the hydrogenated sample is contracting during the initial stage of heating whereas the lattice parameter of the reference sample is expanding. This observation indicates that during the initial stage of heating the contraction of the lattice parameter due to hydrogen desorption has apparently a larger impact than the lattice expansion due to increased temperature. While the lattice of the uncharged sample experiences consistent thermal expansion, the lattice parameter of the charged sample contracts in the beginning as hydrogen is desorbed and then it expands after desorption of most of the diffusible hydrogen.

Thus, as a tentative conclusion it can be assumed that during the early stages of heating diffusible hydrogen desorbs from the interstitial sites and consequently the lattice parameter in the early stages of heating decreases significantly. Once most of the diffusible hydrogen desorbs from the interstitial sites, and the hydrogen desorption rate decreases, the lattice parameter expands due to the heating process and the consequent thermal expansion. The lattice however in this stage exhibits a smaller lattice parameter than that of the uncharged sample, until all diffusible hydrogen is depleted and both samples exhibit the same tendency. Since almost no hydrogen is present at the interstitial sites, the lattice parameter of the hydrogenated sample reaches the dimensions of the uncharged samples.

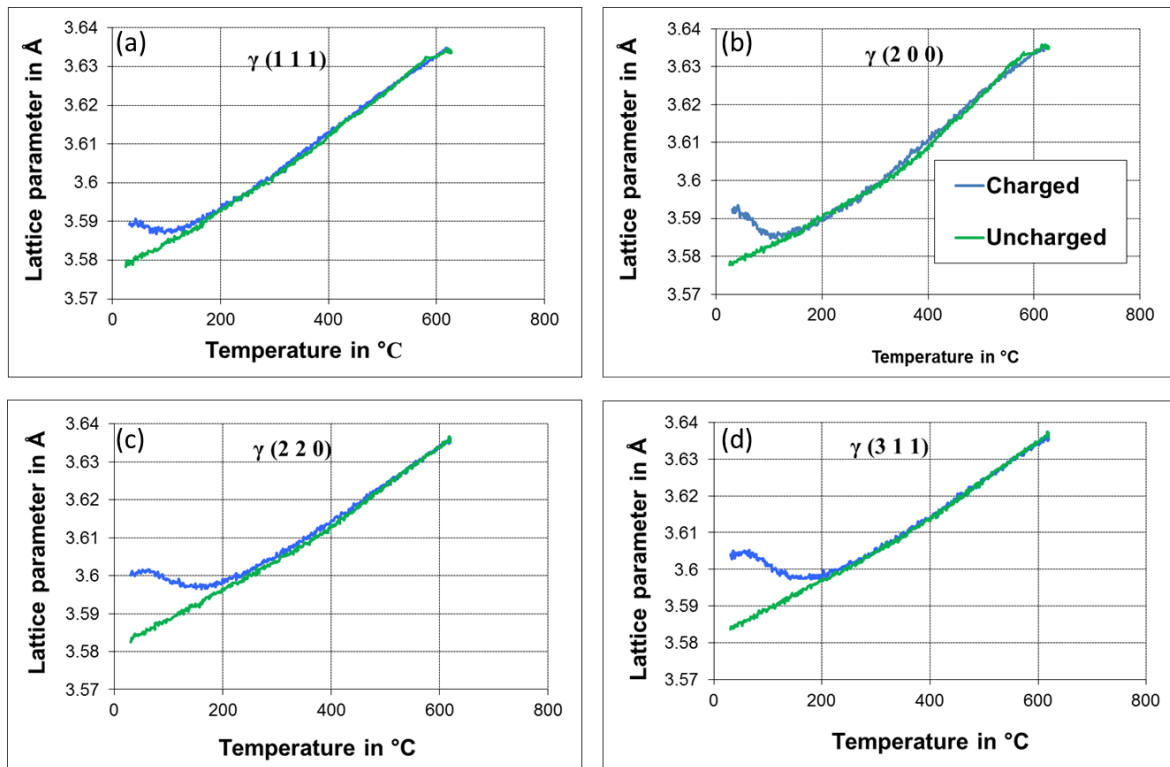


Figure 5-19: Lattice parameter changes measured for the austenitic phase during heating of a hydrogenated sample and a reference sample up to 625°C (a) $\gamma(111)$ (b) $\gamma(200)$ (c) $\gamma(220)$ (d) $\gamma(311)$

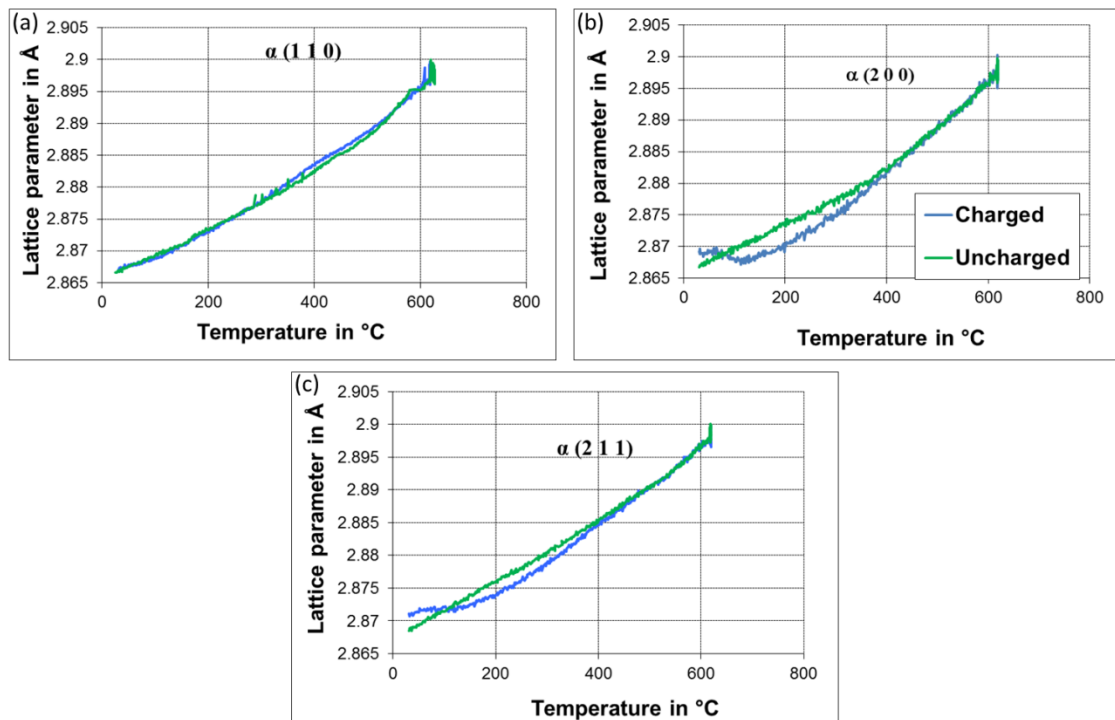


Figure 5-20: Lattice parameter changes measured for the martensitic/ferritic phase during heating of a hydrogenated sample and a reference sample up to 625°C (a) $\alpha(110)$ (b) $\alpha(200)$ (c) $\alpha(211)$

When the samples reach the temperature of about 200°C, both charged and uncharged samples possess the same tendency and lattice dimensions, as the majority of the diffusible hydrogen is depleted from the sample. This observation confirms the tendency of the hydrogen diffusion coefficient and its changes with regard to temperature. As can be seen in Figure 2-8, there is an intense increase of the diffusion coefficient by heating up to 200°C, which is moderated at higher temperatures. It can be accordingly assumed that the majority of the effusion process took place in the early stages of heating during the drastic increase of the hydrogen diffusion coefficient.

In order to eliminate the influence of the heating process on the dimensions of the lattice parameter of the hydrogen charged sample and to be able to isolate the influence of hydrogen upon it, the curves related to the reference sample have been subtracted from those of the charged one. This procedure was conducted assuming that the lattice parameter differences between the two samples are solely influenced by the solute hydrogen in interstitial sites. Hence, the subtraction of the reference sample's curve from the hydrogen charged sample's curve yields a curve that corresponds to qualitative hydrogen content in the charged sample during the effusion process. These differences of the lattice parameter in the austenitic and the ferritic/martensitic phases are presented in Figure 5-21 a and b, respectively.

It can be seen from the curve that at a temperature of about 200°C there is no more influence of the solute hydrogen on the lattice of the austenitic phase. At a temperature of around 370°C, a second presence of hydrogen in the lattice is observed, as the difference of the lattice parameters between the charged and uncharged samples exhibit a second increment. This is more pronounced in the austenitic phase than in the martensitic phase (see Figure 5-21 b).

By comparing the curves in Figure 5-21 a (representing the qualitative hydrogen content in the austenitic lattice according to EDXRD measurements) to the curves obtained by CGHE method (presented in Figure 5-22), a similar tendency of hydrogen desorption is observed. Both curves indicate, that hydrogen desorption occurs in two main stages. The first stage is desorption of the diffusible hydrogen. The hydrogen atoms located at interstitial lattice sites, which also have higher diffusivity than the trapped hydrogen atoms, effuse in the early stages of the heating process. This desorption phase includes the majority of the hydrogen content in the sample as exhibited by the large desorption peak in the CGHE

curve (Figure 5-22). The time period for this desorption is relatively short as the diffusivity of the solute hydrogen is significantly accelerated at elevated temperatures.

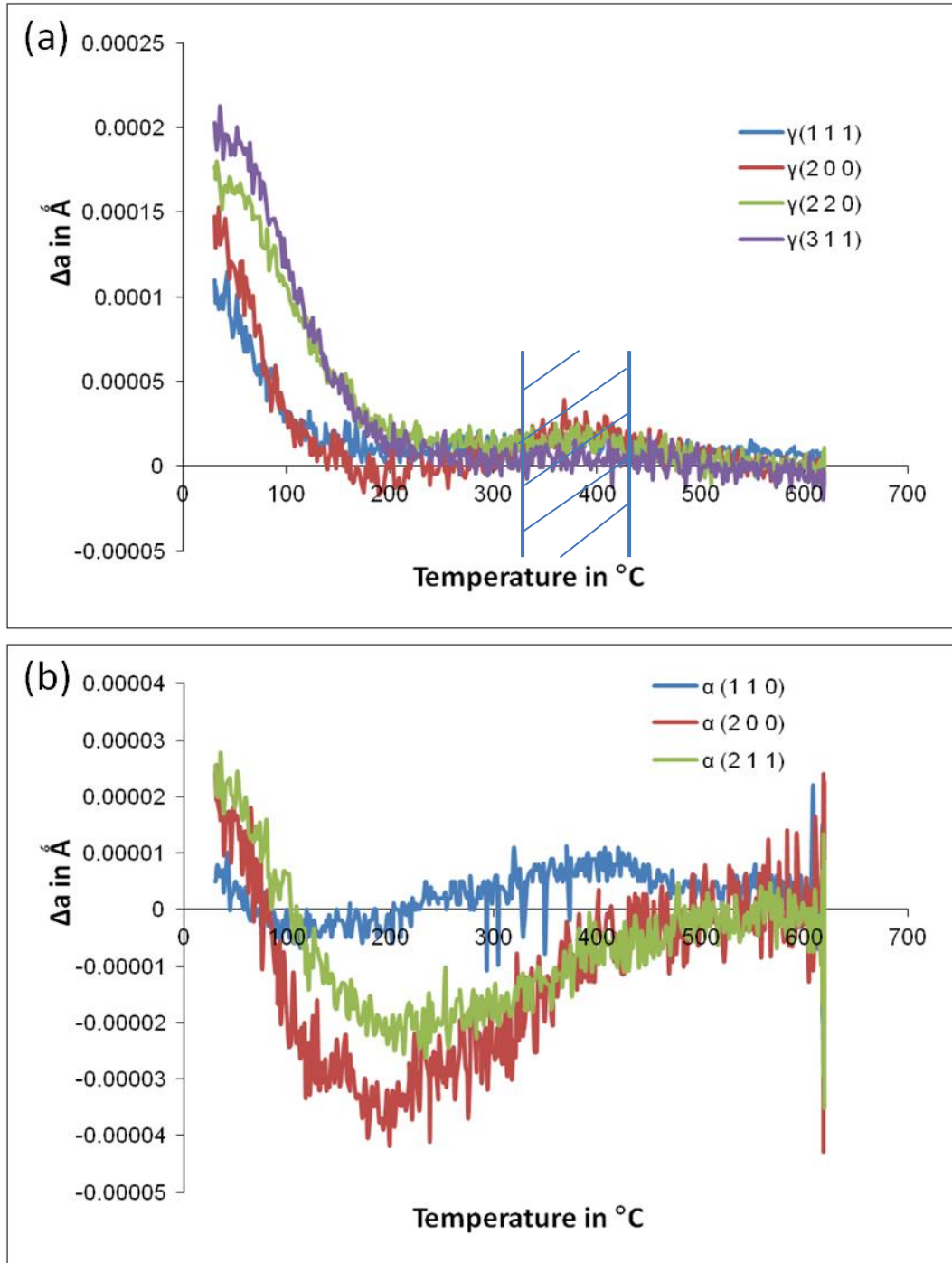


Figure 5-21: The lattice parameter differences between the hydrogen charged sample and uncharged reference sample of the (a) austenitic phase and the (b) ferritic/martensitic phase

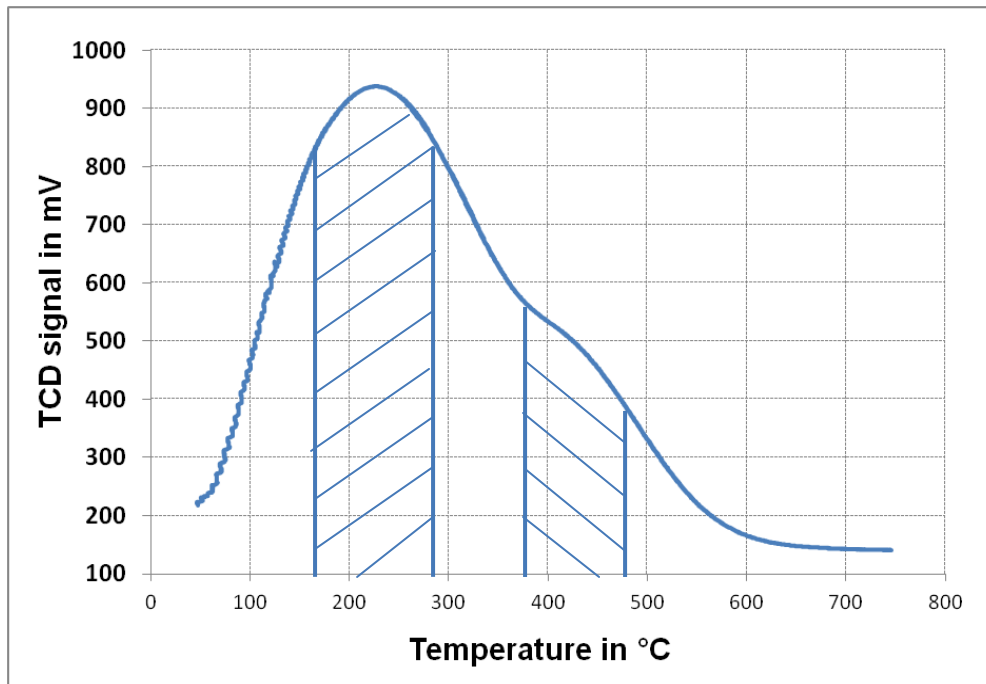


Figure 5-22: CGHE obtained curve for hydrogenated specimen heated with the same heating rate as used in the BESSY II experiment of 10K/min. the Y axis is the signal received from the TCD and is corresponded to the hydrogen content in the nitrogen carrier gas flux

The second stage of the effusion process is desorption of the trapped hydrogen atoms. The hydrogen atoms that were trapped in lattice imperfections (e.g. the phase's interfaces and dislocations) are de-trapped due to high thermal energy and diffuse through the lattice. This can be deduced since both curves exhibit a second and smaller hydrogen concentration peak, which corresponds to the temperature of about 400°C. When hydrogen is de-trapped, it leaves the trap site and it dissolves again in the lattice at the interstitial sites. This causes the secondary effect of the lattice expansion, namely trapped hydrogen becomes dissolved hydrogen as the temperature of the sample exceeds 400°C. It should be mentioned that the trapping sites of phase's interfaces are regarded as reversible kind of traps. This observation supports the theory that at elevated temperatures reversibly trapped hydrogen has a significant contribution to HAC, since it can easily diffuse through the lattice to regions of stress concentration.

It has been verified by previous examinations that the second desorption peak at around 400°C during the heat treatment procedure is attributed to the release of trapped hydrogen from reversible trap sites [97]. The determined binding energies for this released hydrogen range between 0.29 eV and 0.59 eV and thus, can be attributed to trapped

hydrogen at dislocations, grain boundaries, and in between the martensite laths [27]. The appearance of the second peak in the synchrotron measurements is attributed to the hydrogen atoms that were released from trapping site and diffuse through the lattice. This second peak is usually less pronounced in the synchrotron experiments since some of the released hydrogen uses alternative diffusion paths besides diffusion through the lattice, as for instance alongside grain boundaries or dislocations, often regarded as reversible trapping sites. Since the measurements are conducted under conditions of elevated temperatures, the hydrogen atoms have the sufficient thermal energy to avoid being trapped and overcome the activation energy for de-trapping, and as a result, these two kinds of lattice defects become legitimate diffusion paths [10,96].

As can be further seen from the comparison of the two diagrams (Figure 5-21 a and Figure 5-22), the desorption peaks of the CGHE curve appear at some later time than that in the EDXRD measurements. The reason for this difference lies on the principles of the two measurement methods. With EDXRD measurements the amount of solute hydrogen in the lattice is indirectly measured by measuring in-situ the changes of the lattice parameter. With the CGHE method the amount of the evolved hydrogen is measured so-called “ex-situ” by measuring the thermal conductivity changes of the carrier gas after it is carried with the nitrogen gas along the machine’s tubes to the TCD. This path of the hydrogen outside of the sample in the later method induces the corresponding time shift observed between the two compared curves.

The final position of the diffraction lines at the temperature of 625°C is more or less the same for both charged and uncharged samples. This observation is evidence that all of the solute and reversibly trapped hydrogen is released from the sample at such temperatures and after this kind of heat treatment. It might be anticipated that the residual hydrogen, if any, is bound at deeper traps and requires much higher thermal energy and longer heating time in order to be released from these traps and to effuse from the sample [59,62,64].

The diffraction lines correlated with the ferritic/martensitic phase show a different and unexpected behavior (See Figure 5-21 b) than those correlated to the austenitic phase. The tendency in the very beginning of the experiment is quite similar to the tendency in the austenitic phase, namely a contraction of the expanded lattice as the sample is heated due to hydrogen desorption. However, further in the heating process the charged sample’s lattice expands to a lesser extent than that of the uncharged one and exhibits a smaller lattice parameter than that of the reference sample. It appears that hydrogen presence in

the sample retards the thermal expansion of the ferritic/martensitic lattice. It is assumed that this is the result of the reaction of the ferritic/martensitic phase to the contraction of the austenitic phase. The lattice parameter of the austenitic phase contracts in the beginning of the heating process due to rapid hydrogen desorption. It can be further assumed that the lattice of the two phases interact with each other through low angle coherent interfaces. The retained austenite (or annealing/reversed austenite) precipitates between the martensitic laths in a diffusion controlled process. This means that the retained austenite is precipitating with low angle orientation to the martensitic laths [194]. Due to this, the majority of the retained austenite particles have a coherent boundary with the martensitic phase.

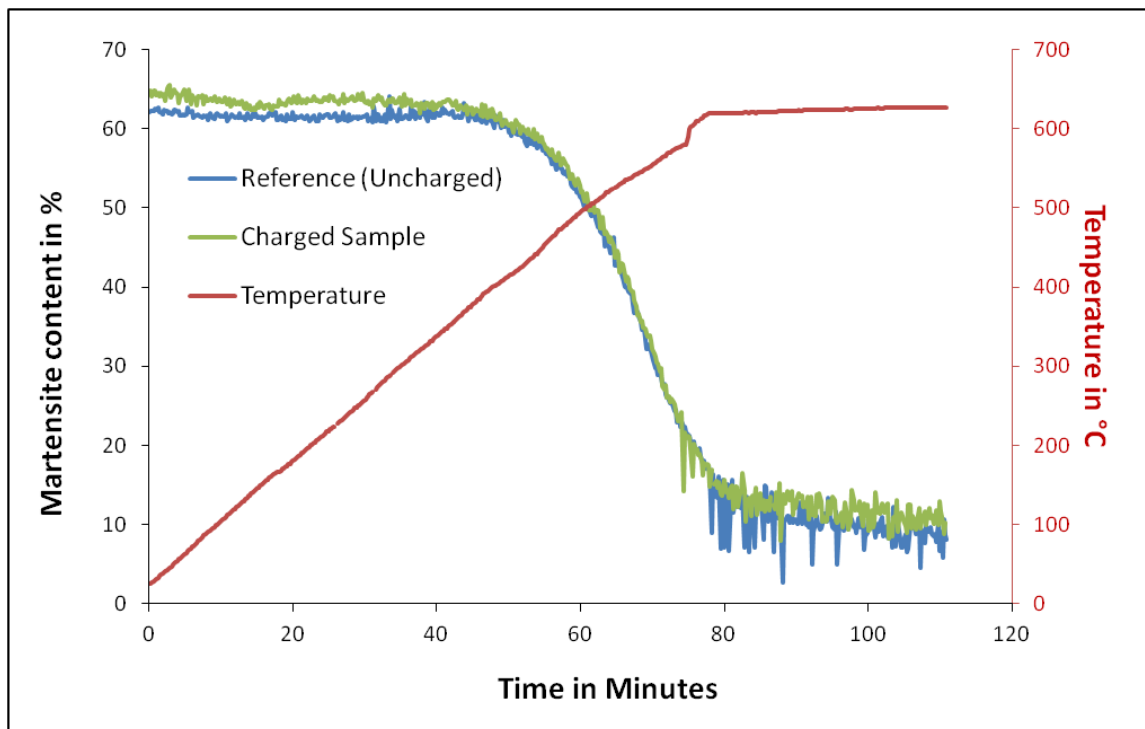


Figure 5-23: Martensite fraction in the microstructure of the steel, calculated according to Laine [180], dependence of the time and temperature for the hydrogenated sample and the uncharged reference sample

The γ (1 1 1) and the α (1 1 0) crystallographic plane families have the interplanar spacing of 2.07 Å and 2.03 Å respectively at the beginning of the experiment and 2.1 Å and 2.05 Å at the end of the experiment at the highest temperature. This relatively similar measure of interplanar spacing allows for a coherent relation between the crystallographic planes in the ferritic/martensitic phase and those in the austenitic phase. The lattice of the ferritic/martensitic phase contracts with that of the austenitic phase due to the coherent

interfaces to smaller dimensions than that of the uncharged sample. That means, that the contraction of the ferritic/martensitic lattice may be a secondary effect of hydrogen desorption since it is not directly related to hydrogen in the ferritic/martensitic phase, rather than being directly related to the contraction of the austenitic phase.

In addition, a slight difference can be seen, between the lattice parameter calculated from the first two austenitic lines which was calculated from the last two lines (Figure 5-19) corresponding to the uncharged sample. This difference is a result of an artifact, in which two diffraction lines that are adjacent to each other induce a shift of both toward higher energy values, consequently leading to a smaller calculated lattice parameter values [195].

Calculations of the phase composition during hydrogen evolution were conducted according to the diffraction lines intensity as was described in Section 4.6. These calculations revealed a significant difference between the hydrogenated and the reference sample.

From the curves in Figure 5-23 it can be seen that the temperature induced phase transformation from martensite to austenite begins at around 400°C (after about 50 minutes) and is completed at around 620°C (after about 80 minutes). However, this phase transformation is attributed solely to the elevated temperatures which induce the energetic preferability of the austenitic phase. It seems that hydrogen presence and hydrogen desorption have no apparent influence on the phase content of the sample. Both curves show no significant difference between the charged and uncharged samples during the austenitic transformation phase. Moreover, the beginning of the austenization (at about 400°C) corresponds to the end of the second desorption phase as shown earlier in this section (see Figure 5-21a).

However, it can be seen that the initial martensite content in the charged sample is higher than the martensite content in the uncharged reference sample. The two curves combine at around 500°C (after about 65 minutes), a temperature that corresponds to the depletion of most of the diffusible and reversibly trapped hydrogen. This indicates that the electrochemical charging process induces a small extent of $\gamma \rightarrow \alpha'$ phase transformation, as was also observed in the previous set of experiments (see Section 5.4).

For summary, the charging process induces two factors that affect the phase content in the material. The first factor, namely strains and consequent stresses in the material due to development of hydrogen concentration gradient from the interface of the austenitic phase

toward its bulk, as previously discussed. These stresses induce the austenite to martensite ($\gamma \rightarrow \alpha'$) phase transformation, as previously reported for austenitic stainless steels [43–45,190,192,196]. The second factor is the reduction of the austenitic phase chemical stability due to hydrogen presence in this phase, which promotes the correspondent phase transformation and consequently the increase of the martensite content in the charged sample as compared to the uncharged one. This effect is eliminated at around 250°C as the majority of the diffusible hydrogen is desorbed from the sample. To support this argumentation, it can be seen that during the early stage of the heating process, where the curve correlated to the uncharged reference sample exhibits a straight tendency, the curve of the charged sample exhibit a very small negative slope, indicating the reduction of the martensitic phase content during the effusion of hydrogen from the sample.

5.6. Hydrogen interaction with residual stresses

The main and dominating factor that causes the occurrence of HAC, especially but not solely in welded components, is the combination of residual stresses and hydrogen presence [197,198]. However, the interaction of hydrogen and residual stresses has been less investigated and there is no sufficient experimental data which provides information to elucidate this phenomenon. The influence of hydrogen presence on the residual stress state in the material has been examined by two X-ray diffraction techniques; the mobile diffractometer and high energy synchrotron X radiation. These examinations are presented in the following section and have been conducted with various hydrogen concentration levels and during the process of hydrogen desorption by degassing at ambient temperature.

In order to conduct a primary examination of the discussed phenomenon in SMSS, a hydrogenated sample was subjected to a continually examination by means of the mobile X-ray diffractometer according to the procedure described in Section 4.5.1. The sample, having the dimensions of 10x5x1 mm³ was electrochemically hydrogen charged for 24 hours with the current density of 20 mA/cm² (according to the process described in Section 4.2) in order to achieve the maximal possible hydrogen concentration in the surface layer (where the measurement of conventional XRD devices takes place). The results of the measurements for the martensitic/ferritic phase diffraction line measured and calculated in accordance to the crystallographic plane family α (2 1 1) are presented in Figure 5-24. These results revealed the presence of compressive residual stresses in the parallel plane

to the surface of the sample (measurement depth is limited up to 4 μm). These compressive stresses were decreased during hydrogen effusion as the measurements were conducted for a time period of about 6 hours at ambient temperature. By comparison of the tendency obtained in Figure 5-24 to the tendency of the results that are presented in Section 5.4, it can be deduced that the changes of the compressive residual stresses are more or less proportional to the changes of the hydrogen content in the alloy.

For further and more accurate determination of the hydrogen influence upon the residual stresses state in the material, six samples, subjected to the same mechanical processing (machining and mechanical grinding), and possessing the geometrical dimension of $10 \times 5 \times 1 \text{ mm}^3$ were electrochemically hydrogen charged for time periods of 1, 2 and 24 hours (with the current density of 20 mA/cm^2) for residual stresses measurements at the BESSY facility. The different charging times were chosen arbitrarily in order to measure and determine the influence of different hydrogen concentrations upon the residual stress state. The hydrogen concentrations were determined by applying the CGHE method (see Section 4.3) in three of the samples (one sample for each charging time period), and are summarized in Table 5-5. The remaining three samples were used for the residual stress measurements by means of EDXRD by applying the $\sin^2\psi$ method at the EDDI beamline [199].

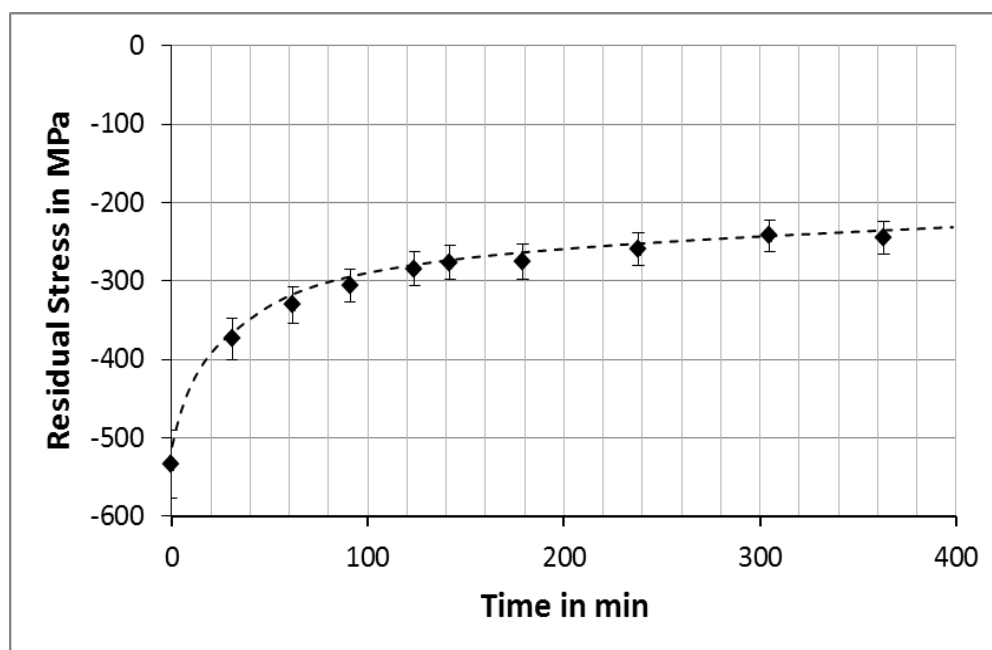


Figure 5-24: Residual stresses measurement by means of the mobile X-ray diffractometer for the (211) crystallographic plane family

Table 5-5: The hydrogen concentration in the SMSS samples after various charging periods

Electrochemical hydrogen charging time in hours	Hydrogen concentration in wt. ppm
1	6.7
2	28.3
24	403

The influence of hydrogen, immediately after the electrochemical charging process on the residual stresses state in the sample is presented Figure 5-25 a and b for both, the martensitic/ferritic and austenitic phase, respectively, as well as for the three mentioned above charging times (1, 2 and 24 hours). These diagrams show the presence of compressive residual stresses in the sample for all four measures of hydrogen content (including the uncharged state). These diagrams show also the distribution of the stresses from higher values at the surface of the sample to lower values at deeper levels in the sample's bulk (the calculations of the depth of the collected information were done as described in the previous Sections 5.4. and 5.5). The compressive residual stresses in the uncharged condition have been induced by the former mechanical processing, i.e. cutting and grinding of the sample as a part of the specimen preparation process. These processes are well known to have an effect on the surface layer and this effects decay towards deeper layers in the material.

It can be further seen in Figure 5-25 that after electrochemical hydrogen charging of the sample the compression residual stresses in both phases have increased. The values of this increment are proportional to the charging time, namely to the hydrogen concentration in the sample. The sample which was charged for 1 hour (having the hydrogen concentration of 6.7 wt. ppm) exhibits the lowest increment in comparison to the samples which were charged for 2 and 24 hours (having hydrogen concentration of 28.3 and 403 wt. ppm, respectively). The last ones show significantly higher values of compressive residual stresses and a large difference from the values of the residual stresses measured for the uncharged reference sample.

A quick and a false conclusion from this observation would be that the introduction of hydrogen in a steel component achieves a better fatigue resistance. Increased compressive stresses at the surface necessitate higher applied external load in order to initiate a crack and to assist the crack's propagation.

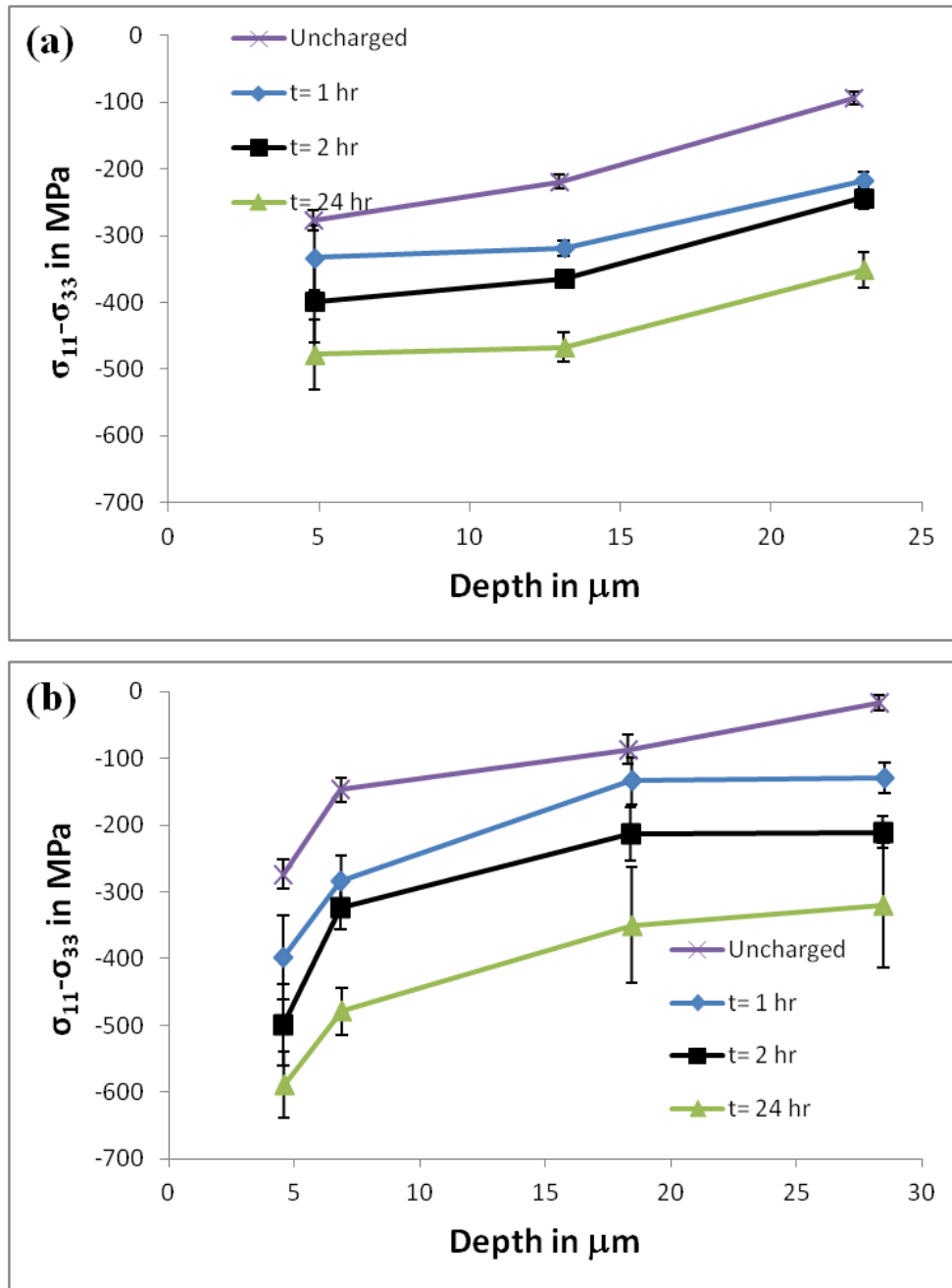


Figure 5-25: The residual stresses and their distribution in the sample's bulk before and after hydrogen cathodic charging with different charging times for the (a) ferritic/martensitic phase and the (b) austenitic phase

However, the basic assumption for residual stresses measurement using the $\sin^2\psi$ method is that the stress perpendicular to the surface (σ_{33}) is equal to zero, as the calculated stress is always the subtraction of stress perpendicular to the surface (σ_{33}) from the stress parallel to the surface (σ_{11} or σ_{22}). This assumption is not likely to be correct in case of electrochemically hydrogenated specimen; it was clearly observed in Section 5.4 that hydrogen presence strains the lattice in the perpendicular direction to the surface. It can be assumed based on the observations in Section 5.4 that the presence of hydrogen strains the lattice and consequently induces tensile stress in the direction normal to the surface (σ_{33}). Due to these facts the calculation of the residual stress using the $\sin^2\psi$ method yields a negative value. It can be assumed that the σ_{33} stress is larger than the parallel stress σ_{11} , consequently lowering the value of $\sigma_{33}-\sigma_{11}$. With hydrogen effusion the lattice is strained to a lesser extent and consequently the absolute value of $\sigma_{33}-\sigma_{11}$ decreases.

This claim is supported by the $\sin^2\psi$ plot (see Figure 5-26). It can be seen that there is a deviation from linearity of the interplanar spacing as a function of $\sin^2\psi$ as the curve approaches the value 1. This is an indication for a stress gradient in the direction normal to the surface (σ_{33}) [200].

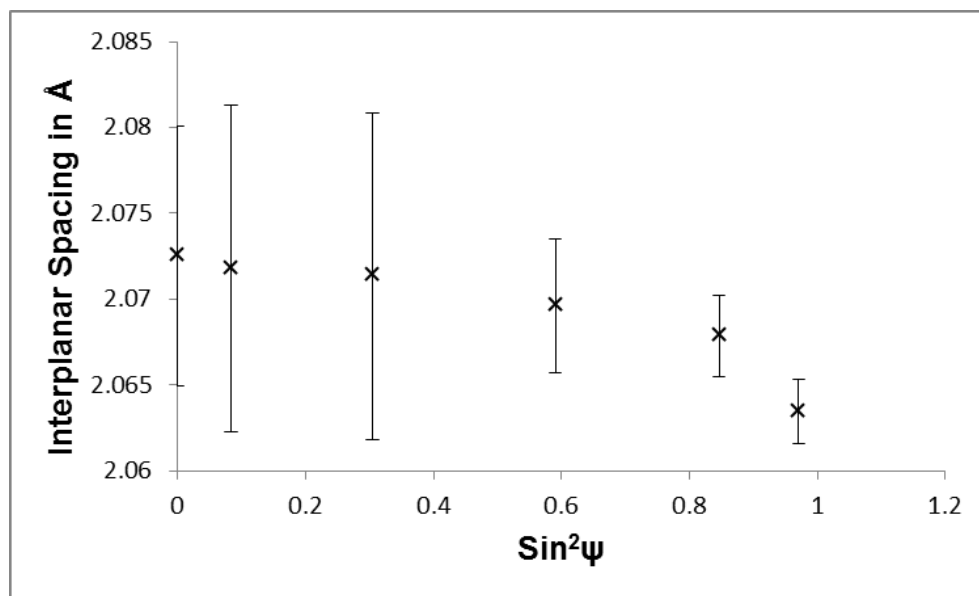


Figure 5-26: A $\sin^2\psi$ diagram taken from the beginning of the examination of the 1 hour charged sample. The deviation from linearity toward the right side of the diagram indicates the presence of stress gradient in the normal direction

The residual stresses values of the hydrogen charged samples, and their variation as a function of the degassing time are presented in Figure 5-30, Figure 5-31 and in Figure 5-32 for the 1, 2 hours and 24 hours electrochemically charged samples (having hydrogen concentrations of 6.7, 28.3 and 403 wt. ppm, respectively), respectively. It is evident also from these diagrams that the absolute values of $\sigma_{11}-\sigma_{33}$ decreases during hydrogen desorption at ambient temperature. This observation regards all three charging times and initial hydrogen concentrations. The changes of the residual stress values are more or less linear proportional to the changes of the lattice parameter as measured in Section 5.4 and in former publications and studies conducted by different measurement techniques (e.g. neutron radiography) [193,201,202].

In addition, it is evident that for all hydrogen concentrations the absolute value of the residual stress is larger at the surface and decreases in the sample's bulk. This might be attributed to the inhomogeneous distribution of the hydrogen concentration in the sample, varying from relatively high concentration at the surface to lower concentration in the sample's bulk. Furthermore, this can be also attributed to the effect of the mechanical processing and the consequent plastic deformation. This influences the surface layer of the sample and its effect fades toward the sample's bulk.

A further assumption is that wherever there is an increase of the compressive residual stresses in one location in the component there will be an increment of the tensile residual stresses in another location in the component and in the exact same orientation. That implies that the introduction of hydrogen in an unstressed sample induces in some regions a tensile stress and in other regions compressive stress in the same orientation. This is due to the basic characteristic of residual stress; the sum of it in all of the given orientation must be equal to zero when no external load is applied. This increase of the tensile residual stresses in some region might lead to the initiation of a crack and crack propagation when a relatively small external load is applied and failure will occur at unexpected conditions of low external load on the component.

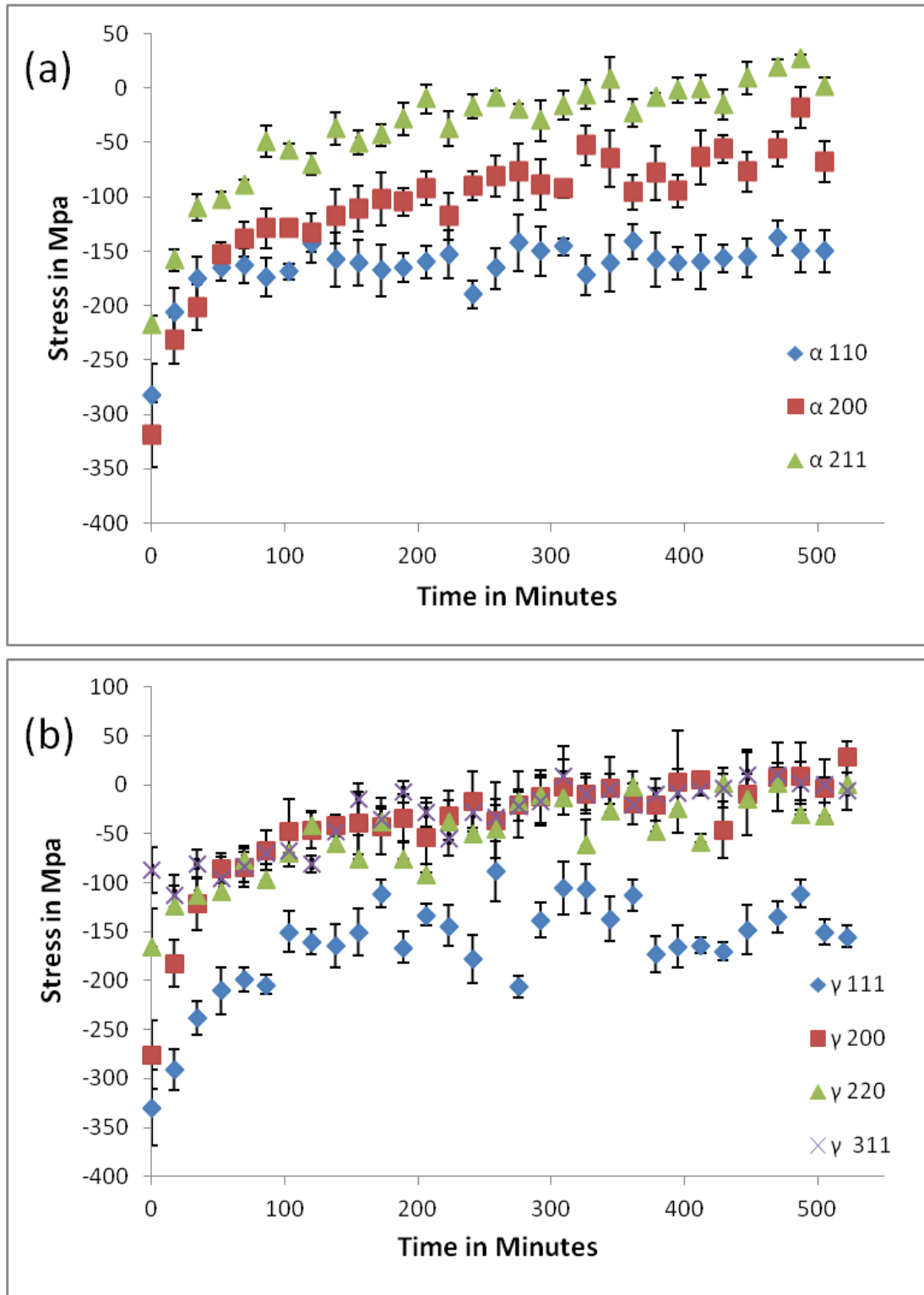


Figure 5-27: The changes of the residual stresses vs. time as the 1 hour hydrogenated sample was being aged at room temperature for hydrogen desorption. The changes appear in both phases; the (a) ferritic/martensitic phase and the (b) austenitic phase

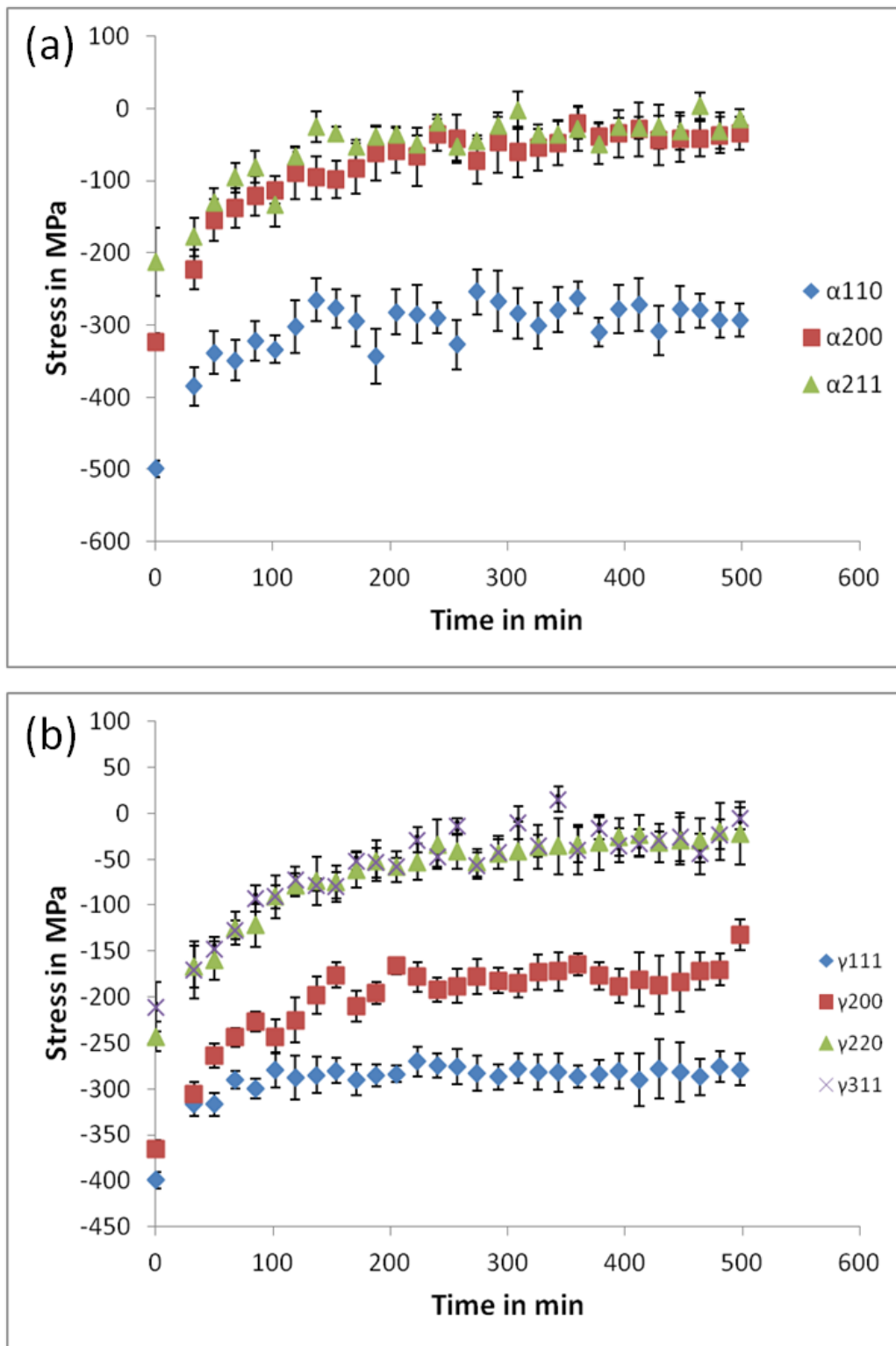


Figure 5-28: The changes of the residual stresses vs. time as the 2 hours hydrogenated sample was being aged at room temperature for hydrogen desorption. The changes appear in both phases; the (a) ferritic/martensitic phase and the (b) austenitic phase

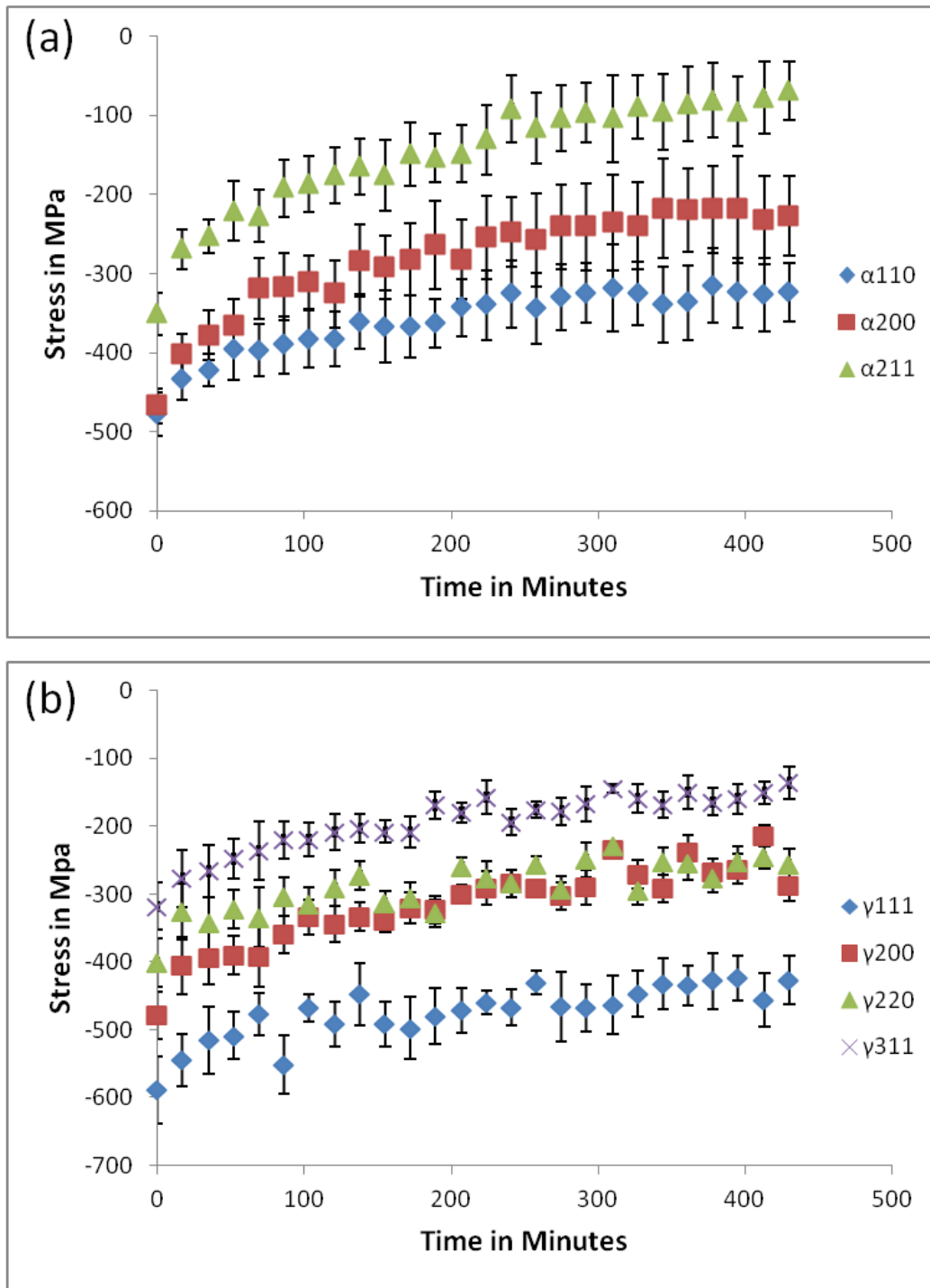


Figure 5-29: The changes of the residual stresses vs. time as the 24 hours hydrogenated sample was being aged at room temperature for hydrogen desorption. The changes appear in both phases; the (a) ferritic/martensitic phase and the (b) austenitic phase

In order to determine the dependency of the residual stress on the hydrogen concentration, the latter was calculated in accordance to the measured interplanar spacing as was explained and done in Section 5.4. The residual stresses as a function of the

hydrogen concentration are presented in Figure 5-30, Figure 5-31 and in Figure 5-32 for the martensitic/ferritic phase and the austenitic phase ('a' for ferritic/martensitic and 'b' for austenitic) and for all three initial hydrogen concentrations, respectively.

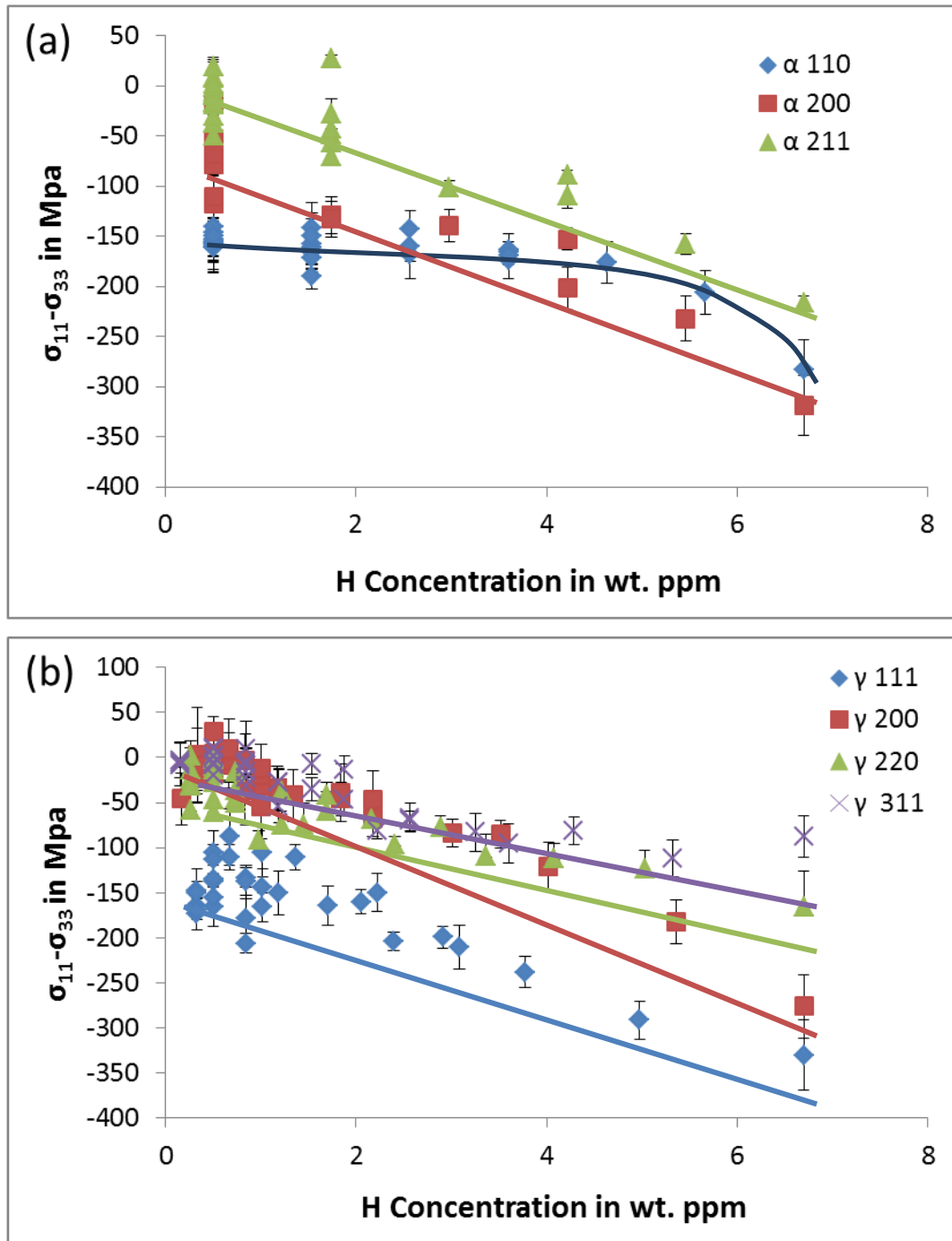


Figure 5-30: The changes of the residual stresses as a function of the hydrogen content for the 1 hour hydrogenated sample. The changes are presented for both phases; the (a) ferritic/martensitic phase and the (b) austenitic phase

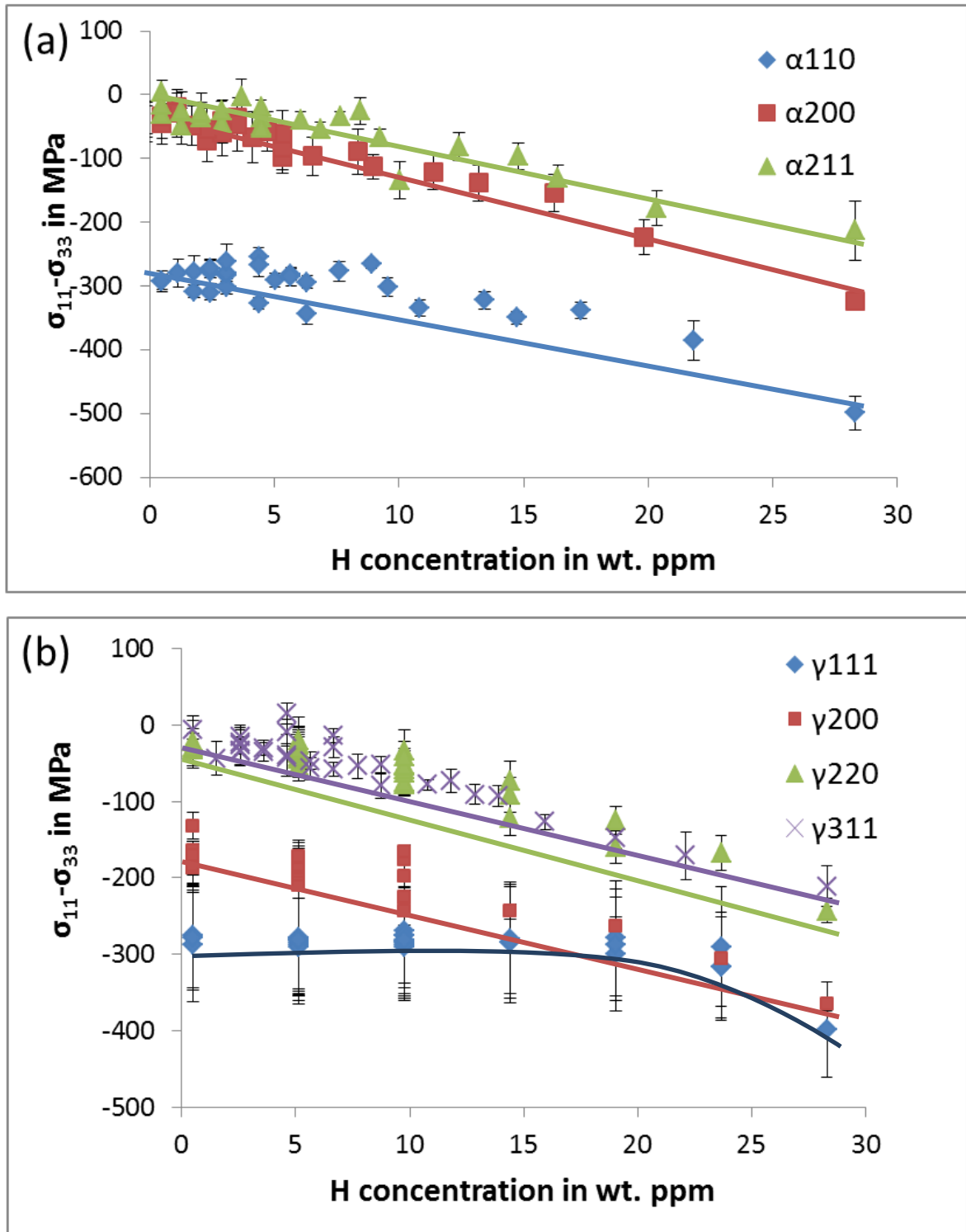


Figure 5-31: The changes of the residual stresses as a function of the hydrogen content for the 2 hour hydrogenated sample. The changes are presented for both phases; the (a) ferritic/martensitic phase and the (b) austenitic phase

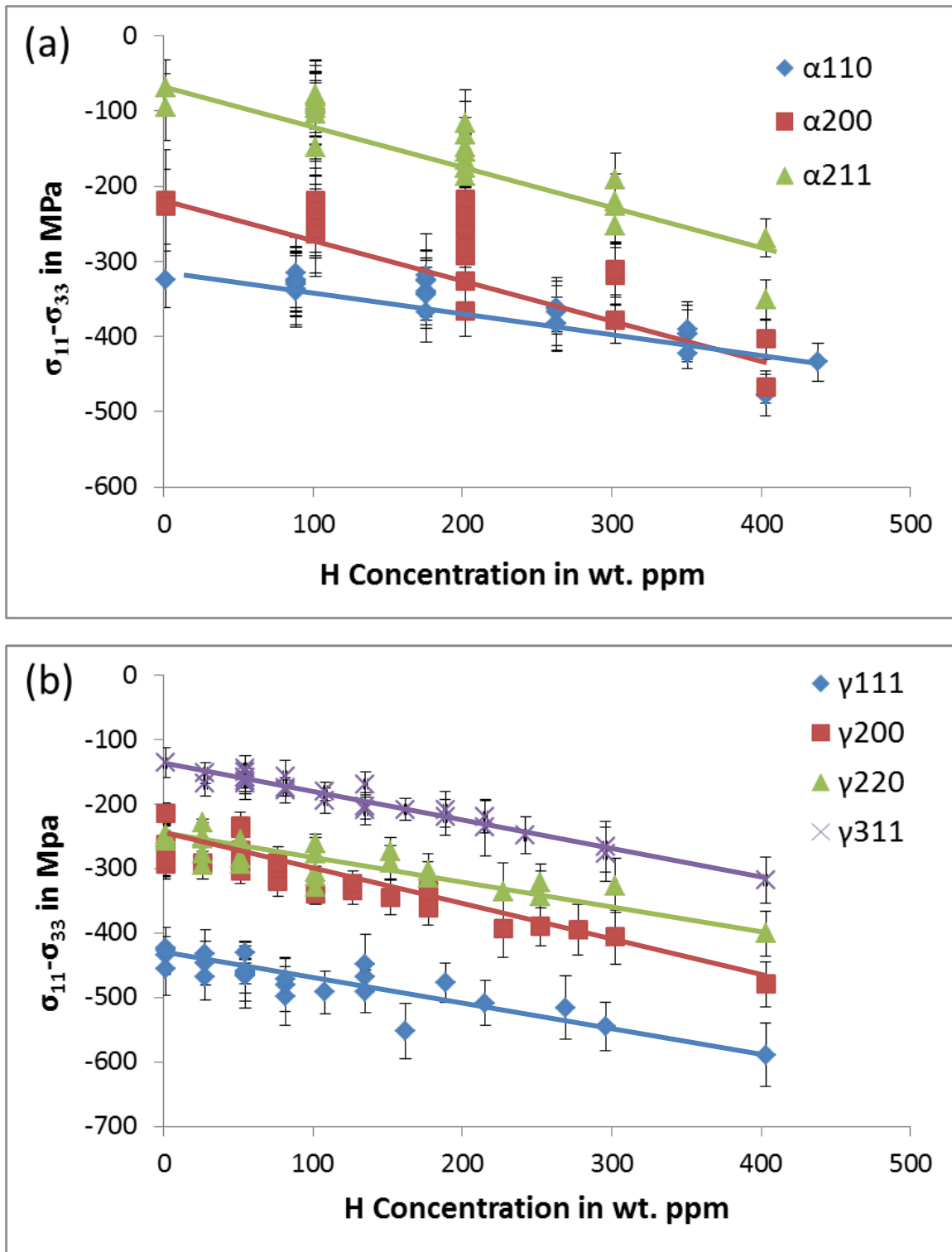


Figure 5-32: The changes of the residual stresses as a function of the hydrogen content for the 24 hour hydrogenated sample. The changes are presented for both phases; the (a) ferritic/martensitic phase and the (b) austenitic phase

To summarize, it is assumed that the changes of the σ_{11} stress are smaller compared to the σ_{33} stress, since the σ_{33} stress has the larger influence upon the calculated stresses. In addition, it can be claimed since the lattice contracts with hydrogen desorption that these tensile residual stresses σ_{33} decrease during desorption. It is reasonable according to these assumptions that the absolute value of the calculated stresses decreases with smaller hydrogen concentration. The diagrams are then in line with these assumptions. However, it is in general difficult to draw any unequivocal conclusions about the real behavior of the residual stress dependency on hydrogen in the lattice. However, these diagrams show at least a clear interaction between solute hydrogen and residual stresses in the supermartensitic tested sample.

The observed interaction of hydrogen with the residual stresses supports in principle the HELP theory. It is claimed according to this theory that hydrogen interacts with the stresses around a dislocation and reduces them, thus facilitating the movement of the dislocation. The observations in this section of the work indicate that there is an evident interaction of hydrogen with stress fields and consequently dislocation mobility can be enhanced with the presence of hydrogen.

In addition, the conducted measurements support the HEDE theory. Since the distances between the iron atoms increase with the presence of hydrogen, it can be claimed that the necessary external force for decohesion of the atomic bonding is smaller. It should be mentioned that the HEDE theory regards the weakening of the atomic bonds through the interaction of hydrogen's electron with the d orbitals of the iron atoms. However, this cannot be visualized by the synchrotron measurements. It is however evident that with the presence of hydrogen the necessary force for decohesion of the iron atoms is decreased through the straining of the metal lattice.

6. Conclusions and Perspectives

In this study, the main objective was set to examine in-situ the hydrogen phase specific transport behavior in SMSS at room temperature and high temperatures, and to examine the hydrogen influence and interaction with residual stresses present in the material using EDXRD.

The current state of knowledge regarding hydrogen damage in steel reflects the lack of parameters and measurement methods for obtaining important parameters (e.g. phase specific hydrogen diffusion coefficients and hydrogen concentrations). These parameters are necessary for the predication of the life time of service under conditions in environments providing the conditions for hydrogen uptake. From the obtained results and after a thorough discussion the following can be concluded:

1. The effects of hydrogen introduction on both phases present in the steel, i.e. FCC (γ) austenite and the BCT (α') martensite, and the kinetics of the respective hydrogen desorption at room temperature and at high temperature, can be clearly followed in such in-situ energy dispersive X-ray diffraction, by measuring the changes in the lattice parameter according to Bragg's law.
2. Hydrogen causes reversible lattice expansion in the respective FCC (γ) austenite and the BCT (α') martensite phase. After the hydrogen is desorbed, the lattice parameter in both phases regains almost its original dimensions. At ambient temperature, most of the dissolved hydrogen in the interstitial lattice sites of the two phases evolves within a time period of about 24 hours.
3. Consistent with the literature, hydrogen dissolution in the austenitic phase is associated with larger lattice expansion indicating higher hydrogen solubility in the austenitic phase than in the martensitic phase.
4. Hydrogen has a slight influence upon the phase transformation in the investigated SMSS. During degassing at room temperature there, was no apparent changes of the phase composition. However, the introduction of hydrogen causes a small extent of $\gamma \rightarrow \alpha$ phase transformation (about 9% in the tested material), as the martensite content of the hydrogen charged sample is higher than that of the uncharged reference sample.
5. The strains calculated from the lattice parameter, introduced by the hydrogen charging process, range below the yield point in the ferritic/martensitic phase and

above the yield point in the austenitic phase. This indicates that the lattice distortion caused by the hydrogenation process is reversible in the case of the ferritic/martensitic phase. However, the higher strains values in the austenitic phase indicate that plastic deformation occurred in this phase and dislocations have been emitted. This is supported by the increased broadness of the diffraction lines related to the austenitic phase. This fact may account for the difference between the lattice parameter of the austenitic phase in the uncharged reference sample and that of the charged sample.

6. The hydrogen diffusion coefficients calculated for the austenitic phase are about one order of magnitude smaller than those of the martensitic phase. This observation proves that hydrogen diffusion is faster in the body centered phase than in the face centered phase. The difference however is smaller than that documented in the literature. It is assumed that the values in the literature of hydrogen diffusion in austenitic stainless steels are affected from the high density of traps in this phase. In the conducted measurements the traps effect has no significant influence on the obtained results.
7. Similarly to respective carrier gas hot extractions, also during heating up to same temperatures in the synchrotron analyses, it can be observed that hydrogen is desorbed in two stages: (1) solute (diffusible) hydrogen is released from the lattice and then (2) reversibly trapped hydrogen probably from grain and phase boundaries, and dislocations. Since the release of trapped hydrogen becomes (at all) visible by lattice parameter changes during the synchrotron analyses, it could be anticipated that the trapped hydrogen portion is, at least partly, first released into the lattice causing minor but visible distortions before being evolved from the microstructure. This allows the conclusion that during de-trapping the hydrogen dissolves in the austenitic phase before effusing from the sample.
8. While heating the sample with temperature ramp of 8°C/minute, all the diffusible hydrogen evolves up to temperature of about 200°C and the trapped hydrogen is completely desorbed at about 500°C.
9. Hydrogen presence in the sample retards the thermal expansion during heating of the ferritic/martensitic lattice, as the lattice parameter expands to a smaller extent as compared to an uncharged sample. This observation may be attributed to the rapid contraction of the austenitic phase and the reaction of the ferritic/martensitic phase to this contraction due to the coherent low angle interfaces between the two phases

10. For a complete desorption of all the diffusible hydrogen, which is one of the main factors inducing HAC, degassing at elevated temperature above 600°C is required for the tested SMSS. However, that kind of process can alternate the microstructure and the phase composition of the steel.
11. The absolute value of $\sigma_{11}-\sigma_{33}$ increases with the presence of hydrogen and decreases again during degassing at ambient temperature and the consequent hydrogen desorption.
12. The change of the residual stress condition induced by hydrogen presence in the component is reversible, as the stresses regain their initial value after the hydrogen was desorbed from the sample. Moreover, the changes of the residual stresses values are directly related to the hydrogen content, as the curves corresponding to the residual stresses and the lattice parameter changes exhibit similar tendencies.
13. It is difficult to achieve any satisfactory statement about the behavior of the residual stresses on the parallel plane to the surface, since the $\sin^2\psi$ method regards the perpendicular stress σ_{33} as equal to zero, an assumption that cannot be assumed in the case of hydrogen presence and during the process of hydrogen desorption. It can be stated, however, that the value of the tensile stress σ_{33} is decreased with hydrogen desorption and/or the value of the compressive stress σ_{11} is decreased.
14. Hydrogen interacts with stress fields in the material. This supports the HELP theory, since the interaction with stress can lead to enhanced dislocation movement.
15. The EDXRD method can be applied to materials with the tendency to create hydrides. Since the crystal structure of the hydrides is different than that of the metal it can be easily recognized and the dynamics of the hydride precipitation process can be examined and studied. Moreover, the stresses that develop during hydride precipitation can be also measured and characterized.
16. This method can be applied to examine the influence of hydrogen presence with different concentration levels on the transformation temperature of steels. The phase composition can be calculated in in-situ scale and the dynamics of the transformation process can be examined.
17. It is proven through the comparison of the diffusion coefficient values calculated with EDXRD with those calculated with the permeation method that EDXRD is reliable for the measurements of phase specific diffusion coefficients in multi-phases materials. This attribute can be applied to the improvement of computer models for the prediction of HAC in multi-phase material e.g. duplex stainless steel.

7. References

1. H.G. Nelson: **Hydrogen embrittlement**, in: **Treatise on Materials Science and Technologie**, (1983) pp. 275–359
2. D. Herlach, C. Kottler, T. Wider, K. Maier: **Hydrogen embrittlement of metals**, *Materials Science and Engineering* 10 (1972), pp.357–368. DOI:10.1016/S0921-4526(00)00431-2
3. R.A. Oriani: **a decohesion theory for hydrogen-induced crack propagation**, in: R.W. Staehle (Ed.), **Stress Corrosion Cracking and Hydrogen Embrittlement of Iron Based Alloys**, Unieux-Firminy, France, (1973) pp. 351–358
4. W. Johnson: **On some remarkable changes produced in iron and steel by the action of hydrogen and acids**, *Proceedings of the Royal Society of London* 23 (1874), pp.168–179
5. H.K. Birnbaum, P. Sofronis: **Hydrogen-enhanced localized plasticity—a mechanism for hydrogen-related fracture**, *Materials Science and Engineering: A* 176 (1994), pp.191–202
6. G.M. Pressouyre, I.M. Bernstein: **A kinetic trapping model for hydrogen-induced cracking**, *Acta Metallurgica* 27 (1979), pp.89–100
7. H.K. Birnbaum, I.M. Robertson, P. Sofronis, D. Teter: **Mechanisms of hydrogen related fracture- a review**, in: T. Magnin (Ed.), **2nd International Conference on Corrosion Deformation Interaction**, Maney Publishing, (1997) pp. 173–195
8. C. Borchers, T. Michler, A. Pundt: **Effect of Hydrogen on the Mechanical Properties of Stainless Steels**, *Advanced Engineering Materials* 10 (2008), pp.11–23. DOI:10.1002/adem.200700252
9. Th. Böllinghaus, H. Hoffmeister, C. Middel: **scatterbands for hydrogen diffusion coefficients in steels having a ferritic or martensitic microstructure and steels having an austenitic microstructure at room temperature**, *Welding in the World(UK)* 37 (1996), pp.16–23
10. Th. Böllinghaus, H. Hoffmeister, A. Dangeleit: **A scatter band for hydrogen diffusion coefficients in micro-alloyed and low carbon structural steels**, *Welding in the World* 35 (1995), pp.83–96
11. N. Narita, H.K. Birnbaum: **On the role of phase transitions in the hydrogen embrittlement of stainless steels**, *Scripta Materialia* 14 (1980), pp.1355–1358
12. V. Gavriljuk: **Phase transformations and relaxation phenomena induced by hydrogen in austenitic stainless steels**, *International Journal of Hydrogen Energy* 22 (1997), pp.269–277

13. V. Bugaev, V. Gavriljuk, Y. Petrov, A. V Tarasenko: ***Mechanism of hydrogen-induced phase transformations in metals and alloys***, *International Journal of Hydrogen Energy* 22 (1997), pp.213–218
14. Th. Böllinghaus, H. Hoffmeister, J. Klemme, H. Alzer: ***Hydrogen Permeation in a Low Carbon Martensitic Stainless Steel Exposed to H₂S Containing Brines at Free Corrosion***, in: ***NACE International, CORROSION 99***, San Antonio, Tx, (1999)
15. Th. Böllinghaus: ***Hydrogen assisted cracking of supermartensitic stainless steels***, in: N.R. Moody, A.W. Thompson, R.E. Ricker, G.W. Was, R.H. Jones (Eds.), ***Hydrogen Effects on Material Behavior and Corrosion Deformation Interactions***, Hydrogen Effects On Materials Behavior And Corrosion Deformation Interactions, TMS, USA, TMS, USA, (2002) pp. 1009 – 1018
16. M. Nagumo, H. Shimura, T. Chaya, H. Hayashi, I. Ochiai: ***Fatigue damage and its interaction with hydrogen in martensitic steels***, *Materials Science and Engineering: A* 348 (2003), pp.192–200. DOI:10.1016/S0921-5093(02)00745-1
17. A. Nagao, C. Smith, M. Dadfarnia, P. Sofronis, I.M. Robertson: ***The role of hydrogen in hydrogen embrittlement fracture of lath martensitic steel***, *Acta Materialia* 60 (2012), pp.5182–5189
18. M. Wang, E. Akiyama, K. Tsuzaki: ***Effect of hydrogen and stress concentration on the notch tensile strength of AISI 4135 steel***, *Materials Science and Engineering: A* 398 (2005), pp.37–46. DOI:10.1016/j.msea.2005.03.008
19. K. Splichal, J. Berka, J. Burda, M. Falcník: ***Hydrogen embrittlement and fracture mode of EUROFER 97 ferritic-martensitic steel***, *International Journal of Pressure Vessels and Piping* 89 (2012), pp.42–47
20. M. Louthan: ***Hydrogen embrittlement of metals: a primer for the failure analyst***, *Journal of Failure Analysis and Prevention* 8 (2008), pp.289–307. DOI:10.1007/s11668-008-9133-x
21. V. Olden, C. Thaulow, R. Johnsen, E. Østby, T. Berstad: ***Influence of hydrogen from cathodic protection on the fracture susceptibility of 25%Cr duplex stainless steel – Constant load SENT testing and FE-modelling using hydrogen influenced cohesive zone elements***, *Engineering Fracture Mechanics* 76 (2009), pp.827–844. DOI:10.1016/j.engfracmech.2008.11.011
22. G. Rørvik, P. Kvaale, O. Akselsen: ***Sources and levels of hydrogen in TIG welding of 13% Cr martensitic stainless steels***, in: ***Supermartensitic Stainless Steels***, (1999) pp. 196–203
23. R. Mollan: ***Experience With 13cr Supermartensitic Stainless Steel In The Tuna Submarine Flowlines***, in: ***CORROSION 2005***, NACE International, Houston, Texas, (2005) pp. 1–20

24. H. Addach, P. Berçot, M. Rezrazi, M. Wery: **Hydrogen permeation in iron at different temperatures**, *Materials Letters* 59 (2005), pp.1347–1351.
DOI:10.1016/j.matlet.2004.12.037
25. H. Addach, P. Berçot, M. Rezrazi, J. Takadoum: **Study of the electrochemical permeation of hydrogen in iron**, *Corrosion Science* 51 (2009), pp.263–267.
DOI:10.1016/j.corsci.2008.10.024
26. L. Péter, B. Almási, B. Verő, H. Schneider: **Theoretical analysis of entrapment kinetics in hydrogen permeation experiments**, *Materials Science and Engineering: A* 339 (2003), pp.245–254. DOI:10.1016/S0921-5093(02)00109-0
27. S. Frappart, A. Oudriss, X. Feaugas, J. Creus, J. Bouhattate, F. Thébault, et al.: **Hydrogen trapping in martensitic steel investigated using electrochemical permeation and thermal desorption spectroscopy**, *Scripta Materialia* 65 (2011), pp.859–862. DOI:10.1016/j.scriptamat.2011.07.042
28. Th. Böllinghaus, D. Seeger: **Hydrogen Permeation In Supermartensitic Stainless Steel Weld Microstructures**, *CORROSION 2004* (2004), pp.1–14
29. Th. Böllinghaus, D. Seeger: **Hydrogen Permeation in Supermartensitic Stainless Steels Exposed to Realistic Formation Water Compositions**, *CORROSION 2003* (2003), pp.1–15
30. L.M. Smith, M. Celant: **Martensitic stainless steel flowlines - Do they pay?**, in: **Supermartensitic Stainless Steels '99**, (1999) pp. 66–73
31. J.C. Lippold, D.J. Kotecky: **Supermartensitic Stainless Steels**, in: **Welding Metallurgy and Weldability of Stainless Steels**, John Wiley & Sons Inc., New Jersey, (2005) pp. 80–83
32. P.D. Bilmes, M. Solari, C.L. Llorente: **Characteristics and effects of austenite resulting from tempering of 13Cr–NiMo martensitic steel weld metals**, *Materials Characterization* 46 (2001), pp.285–296. DOI:10.1016/S1044-5803(00)00099-1
33. A.W. Marshal, J.C.M. Farrar: **Welding of Ferritic and Martensitic 11-14% Cr Steels**, *Welding in the World* 45 (2001), pp.32–55
34. M. Kimura, Y. Miyata, T. Toyooka: **Development of New 13Cr Steel Pipe with High Strength and Good Toughness**, in: **NACE International, CORROSION**, Denver, Co, (2002)
35. M. Kimura, Y. Miyata, T. Toyooka, F. (Fred) Murase: **Corrosion Performance of Martensitic Stainless Steel Seamless Pipe for Linepipe Application**, in: **NACE International, CORROSION**, San Antonio, Tx, (1999)
36. J. Enerhaug, P.E. Kvaale, T. Rogne, M. Bjordal, J.M. Drugli: **Qualification of Welded Super 13%Cr Martensitic Stainless Steels for the Asgard Field**, in: **NACE International**, San Antonio, Tx, (1999)

37. T.G. Gooch, P. Woolin, A.G. Haynes: **Welding Metallurgy of Low Carbon 13% Chromium Martensitic Steels**, in: **Supermartensitic Stainless Steels**, (1999) pp. 188–195
38. Davis J.R: **ASM Specialty Handbook, Stainless Steel**, ASM International, Ohio, (1999)
39. G. Pantazopoulos, A. Vazdirvanidis: **Cracking of underground welded steel pipes caused by HAZ sensitization**, *Case Studies in Engineering Failure Analysis* 1 (2013), pp.43–47. DOI:10.1016/j.csefa.2012.10.001
40. D. Zou, X. Liu, Y. Han, W. Zhang, J. Li, K. Wu: **Influence of Heat Treatment Temperature on Microstructure and Property of 00Cr13Ni5Mo2 Supermartensitic Stainless Steel**, *Journal of Iron and Steel Research, International* 21 (2014), pp.364–368. DOI:10.1016/S1006-706X(14)60056-X
41. M. Tvrdy, V. Vodarek, G. Roznovska, A. Korcak, J. Seliga, J. Barta, et al.: **Production Development and Industrial Application of 12Cr-6Ni-2.5Mo Steels**, in: **Supermartensitic Stainless Steels**, Brussels, Belgium, (2002) pp. 29–36
42. D.D.G. Ulmer, C.J. Altstetter: **Phase relations in the hydrogen-austenite system**, *Acta Metallurgica et Materialia* 41 (1993), pp.2235–2241. DOI:10.1016/0956-7151(93)90393-7
43. P. Rozenak, L. Zevin, D. Eliezer: **Hydrogen effects on phase transformations in austenitic stainless steels**, *Journal of Materials Science* 19 (1984), pp.567–573
44. P. Rozenak, R. Bergman: **X-ray phase analysis of martensitic transformations in austenitic stainless steels electrochemically charged with hydrogen**, *Materials Science and Engineering: A* 437 (2006), pp.366–378. DOI:10.1016/j.msea.2006.07.140
45. P. Rozenak, L. Zevin, D. Eliezer: **Internal stresses in austenitic steels cathodically charged with hydrogen**, *Journal of Materials Science Letters* 2 (1983), pp.63–66. DOI:10.1007/BF00725432
46. N. Narita, C.J. Altstetter, H.K. Birnbaum: **Hydrogen-related phase transformations in austenitic stainless steels**, *Metallurgical Transactions A* 13 (1982), pp.1355–1365
47. S. Teus, V. Shyvanyuk, V.G. Gavriljuk: **Hydrogen-induced $\gamma \rightarrow \epsilon$ transformation and the role of ϵ -martensite in hydrogen embrittlement of austenitic steels**, *Materials Science & Engineering A* 497 (2008), pp.290–294
48. D.G. Ulmer, C.J. Altstetter: **Hydrogen-induced strain localization and failure of austenitic stainless steels at high hydrogen concentrations**, *Acta Metallurgica et Materialia* 39 (1991), pp.1237–1248. DOI:10.1016/0956-7151(91)90211-1

49. P. Rozenak, D. Eliezer: **Effects of ageing after cathodic charging in austenitic stainless steels**, *Journal of Materials Science* 19 (1984), pp.3873–3879. DOI:10.1007/BF00980750
50. E. Viyanit: **Numerical Simulation of Hydrogen Assisted Cracking in Supermartensitic Stainless Steel Welds**, Helmut Schmidt University- University of the Federal Armed Forces Hamburg, (2005)
51. P. Rozenak, D. Eliezer: **Phase changes related to hydrogen-induced cracking in austenitic stainless steel**, *Acta Metallurgica* 35 (1987), pp.2329–2340
52. D. Eliezer, E. Tal-Gutelmacher, C.E. Cross, Th. Böllinghaus: **Hydrogen absorption and desorption in a duplex-annealed Ti–6Al–4V alloy during exposure to different hydrogen-containing environments**, *Materials Science and Engineering: A* 433 (2006), pp.298–304. DOI:10.1016/j.msea.2006.06.088
53. D. Eliezer, E. Tal-Gutelmacher, C.E. Cross, Th. Böllinghaus: **Hydrogen trapping in β -21S titanium alloy**, *Materials Science and Engineering: A* 421 (2006), pp.200–207. DOI:10.1016/j.msea.2006.01.067
54. E. Dabah, V. Lisitsyn, D. Eliezer: **Performance of hydrogen trapping and phase transformation in hydrogenated duplex stainless steels**, *Materials Science & Engineering A* 527 (2010), pp.4851–4857. DOI:10.1016/j.msea.2010.04.016
55. D. Eliezer, Y. Nissim, T. Kannengießner: **Effects of Shielding with Various Hydrogen-Argon Mixtures on Supermartensitic Stainless Steel TIG Welds**, *Materials Testing* 52 (2010), pp.306–315. DOI:10.3139/120.110135
56. A. Pundt, R. Kirchheim: **HYDROGEN IN METALS: Microstructural Aspects**, *Annual Review of Materials Research* 36 (2006), pp.555–608. DOI:10.1146/annurev.matsci.36.090804.094451
57. R. Dayal, N. Parvathavarthini: **Hydrogen embrittlement in power plant steels**, *Sadhana* 28 (2003), pp.431–451
58. H.G. Lee, J.-Y. Lee: **Hydrogen trapping by TiC particles in iron**, *Acta Metallurgica* 32 (1984), pp.131–136. DOI:10.1016/0001-6160(84)90210-4
59. A. Krom, A. Bakker: **Hydrogen trapping models in steel**, *Metallurgical and Materials Transactions B* 31 (2000), pp.1475–1482
60. C. a Wert, R.C. Frank: **Trapping of Interstitials in Metals**, *Annual Review of Materials Science* 13 (1983), pp.139–172. DOI:10.1146/annurev.ms.13.080183.001035
61. A. McNabb, P. Foster: **A new analysis of the diffusion of hydrogen in iron and ferritic steels**, *Transactions of the Metallurgical Society of AIME* 227 (1963), pp.618–627

62. S. Lee, J. Lee: ***The trapping and transport phenomena of hydrogen in nickel***, *Metallurgical and Materials Transactions A* 17 (1986), pp.181–187
63. G.M. Pressouyre: ***A classification of hydrogen traps in steel***, *Metallurgical and Materials Transactions A* 10 (1979), pp.1571–1573. DOI:10.1007/BF02812023
64. R.A. Oriani: ***The diffusion and trapping of hydrogen in steel***, *Acta Metallurgica* 18 (1970), pp.147–157
65. I.S. Maroef, D.L. Olson, M. Eberhart, G.R. Edwards: ***Hydrogen trapping in ferritic steel weld metal***, *International Materials Reviews* 47 (2002), pp.191–223. DOI:10.1179/095066002225006548
66. S. Frappart, X. Feaugas, J. Creus: ***Hydrogen solubility, diffusivity and trapping in a tempered Fe-C-Cr martensitic steel under various mechanical stress states***, *Materials Science and Engineering A* 534 (2012), pp.384–393
67. F.G. Wei, T. Hara, K. Tsuzaki: ***Precise Determination of the Activation Energy for Desorption of Hydrogen in Two Ti-Added Steels by a Single Thermal-Desorption Spectrum***, *Metallurgical and Materials Transactions B* 35 (2004), pp.587–597
68. K. Lee, J.Y. Lee: ***A new method of the calculation of the hydrogen trap activation energy in metals***, *Journal of Materials Science Letters* 2 (1983), pp.538–540
69. F.J. Castro, G. Meyer: ***Thermal desorption spectroscopy (TDS) method for hydrogen desorption characterization (I): theoretical aspects***, *Journal of Alloys and Compounds* 330-332 (2002), pp.59–63. DOI:10.1016/S0925-8388(01)01625-5
70. W. Choo, J. Lee: ***Thermal analysis of trapped hydrogen in pure iron***, *Metallurgical and Materials Transactions A* 13 (1982), pp.135–140
71. M. Enomoto, D. Hirakami, T. Tarui: ***Modeling Thermal Desorption Analysis of Hydrogen in Steel***, *ISIJ International* 46 (2006), pp.1381–1387. DOI:10.2355/isijinternational.46.1381
72. J. Lee, S. Lee: ***Hydrogen trapping phenomena in metals with B.C.C. and F.C.C. crystals structures by the desorption thermal analysis technique.pdf***, *Surface and Coating Technology* 28 (1986), pp.301–314
73. E. Tal-Gutelmacher, D. Eliezer, E. Abramov: ***Thermal desorption spectroscopy (TDS)—Application in quantitative study of hydrogen evolution and trapping in crystalline and non-crystalline materials***, *Materials Science and Engineering: A* 445-446 (2007), pp.625–631. DOI:10.1016/j.msea.2006.09.089
74. A. Turnbull, R. Hutchings, D. Ferriss: ***Modelling of thermal desorption of hydrogen from metals***, *Materials Science and Engineering: A* 238 (1997), pp.317–328

75. K. Wilson, M. Baskes: **Thermal desorption of deuterium-implanted stainless steel**, *Journal of Nuclear Materials* 74 (1978), pp.179–184
76. K. Bergers, E. Camisão de Souza, I. Thomas, N. Mabho, J. Flock: **Determination of Hydrogen in Steel by Thermal Desorption Mass Spectrometry**, *Steel Research International* 81 (2010), pp.499–507. DOI:10.1002/srin.201000023
77. J. Chene: **hydrogen diffusion and trapping in steels and related embrittlement effect**, in: **Steel Hydrogen**, (2001) pp. 53–65
78. A. Taha, P. Sofronis: **A micromechanics approach to the study of hydrogen transport and embrittlement**, *Engineering Fracture Mechanics* 68 (2001), pp.803–837. DOI:10.1016/S0013-7944(00)00126-0
79. H. Johnson: **Hydrogen in iron**, *Metallurgical and Materials Transactions A* 19 (1988), pp.2371–2387
80. P. Bastien, P. Azou: **Influence de Lecrouissage sur le Frottement Interieur du fer et de Lacier, Charges ou non en Hydrogene**, *Comptes Rendus Hebdomadaires Des Seances de L'Academie Des Sciences* 232 (1951), pp.1845–1848
81. J. Tien, A. Thompson, I.M. Bernstein, R.J. Richards: **Hydrogen transport by dislocations**, *Metallurgical Transactions A* 7 (1976), pp.821–829
82. H. Johnson, J. Hirth: **Internal hydrogen supersaturation produced by dislocation transport**, *Metallurgical and Materials Transactions A* 7 (1976), pp.1543–1548
83. P. Sofronis, H.K. Birnbaum: **Mechanics of the hydrogen -dislocation-impurity interactions—I. Increasing shear modulus**, *Journal of the Mechanics and Physics of Solids* 43 (1995), pp.49–90
84. E. Sirois, H.K. Birnbaum: **Effects of hydrogen and carbon on thermally activated deformation in nickel**, *Acta Metallurgica et Materialia* 40 (1992), pp.1377–1385
85. M. Hashimoto, R. Latanision: **The role of dislocations during transport of hydrogen in hydrogen embrittlement of iron**, *Metallurgical and Materials Transactions A* 19 (1988), pp.2799–2803. DOI:10.1007/bf02645814
86. I. Robertson, H. Birnbaum: **Dislocation mobility and hydrogen—a brief review**, *Proc. 11th International Conference on Fracture* (2009),
87. H.K. Birnbaum: **Mechanisms of hydrogen related fracture of metals**, (1989)
88. A. Brass, J. Chene: **Influence of deformation on the hydrogen behavior in iron and nickel base alloys: a review of experimental data**, *Materials Science and Engineering: A* 242 (1998), pp.210–221
89. S.S.M. Charca, O.N.C.O. Uwakweh, V.V.A. Agarwala: **Comparative Study of Hydrogen Transport Behaviors in ARMCO-Fe and AF1410 Steels**, *Corrosion Reviews* 25 (2007), pp.377–400

90. E. Owczarek, T. Zakroczymski: **Hydrogen transport in a duplex stainless steel**, *Acta Materialia* 48 (2000), pp.3059–3070. DOI:10.1016/S1359-6454(00)00122-1
91. M. Louthan, R. Derrick: **Hydrogen transport in austenitic stainless steel**, *Corrosion Science* 15 (1975), pp.565–577
92. W.C. Luu, P.W. Liu, J.K. Wu: **Hydrogen transport and degradation of a commercial duplex stainless steel**, *Corrosion Science* 44 (2002), pp.1783–1791. DOI:10.1016/S0010-938X(01)00143-3
93. A. Turnbull, E. Lembach-Beylegaard, R. Hutchings: **Hydrogen transport in duplex stainless steels**, in: **Fourth International Conference Duplex Stainless Steels**, (1994)
94. D. Figueroa-Gordon, M. Robinson: **Hydrogen transport and embrittlement in 300 M and AerMet100 ultra high strength steels**, *Corrosion Science* 52 (2010), pp.1593–1602
95. A. Griffiths, R. Hutchings, A. Turnbull: **Hydrogen uptake and transport in low alloy steels**, *The Welding Research Council, Inc.* 526 (1994), pp.69–80
96. V. Olden, C. Thaulow, R. Johnsen: **Modelling of hydrogen diffusion and hydrogen induced cracking in supermartensitic and duplex stainless steels**, *Materials & Design* 29 (2008), pp.1934–1948. DOI:10.1016/j.matdes.2008.04.026
97. S. Brauser, T. Kannengießer: **Hydrogen absorption of different welded duplex steels**, *International Journal of Hydrogen Energy* 35 (2010), pp.4368–4374. DOI:10.1016/j.ijhydene.2010.01.148
98. E. Dabah, T. Kannengießer, T. Mente, K. Beyer, S. Brauser: **Quantification of hydrogen effective diffusion coefficients and effusion behavior in duplex stainless steel weld metals**, *Welding in the World* 57 (2013), pp.561–567. DOI:10.1007/s40194-013-0051-5
99. D. Seeger: **Wasserstoffaufnahme und -diffusion in Schweißnahtgefügen hochfester Stähle**, Helmut Schmidt University- University of the Federal Armed Forces Hamburg, (2004)
100. C.H. Noreña, P. Bruzzoni: **Effect of microstructure on hydrogen diffusion and trapping in a modified 9% Cr–1% Mo steel**, *Materials Science and Engineering: A* 527 (2010), pp.410–416. DOI:10.1016/j.msea.2009.08.025
101. D. Herlach: **Hydrogen embrittlement of metals**, *Physica B: Condensed Matter* 289-290 (2000), pp.443–446. DOI:10.1016/S0921-4526(00)00431-2
102. M. Louthan: **The Effect of Hydrogen on Metals**, New York, (1987)
103. P. Bastien, P. Azou: **Effect of Hydrogen on the Deformation and Fracture of Iron and Steel in Simple Tension**, in: **The First World Metallurgical Congress**, (1951)

104. E.A. Groshart: ***Design and Finish Requirements of High Strength Steels***, *Metal Finishing* 82 (1984), pp.49
105. E. Tal-Gutelmacher, D. Eliezer: ***The hydrogen embrittlement of titanium-based alloys***, *JOM* 110 (2005), pp.0–3
106. C.L. Briant, Z.F. Wang, N. Chollocoop: ***Hydrogen embrittlement of commercial purity titanium***, *Corrosion Science* 44 (2002), pp.1875–1888. DOI:10.1016/S0010-938X(01)00159-7
107. A. Barnoush, H. Vehoff: ***Hydrogen embrittlement of aluminum in aqueous environments examined by in situ electrochemical nanoindentation***, *Scripta Materialia* 58 (2008), pp.747–750. DOI:10.1016/j.scriptamat.2007.12.019
108. N. Eliaz, A. Shachar, B. Tal, D. Eliezer: ***Characteristics of hydrogen embrittlement, stress corrosion cracking and tempered martensite embrittlement in high-strength steels***, *Engineering Failure Analysis* 9 (2002), pp.167–184. DOI:10.1016/S1350-6307(01)00009-7
109. J. Hirth: ***Effects of hydrogen on the properties of iron and steel***, *Metallurgical Transactions A* 11 (1980), pp.861–890
110. C. Zapffe, C. Sims: ***Hydrogen embrittlement, internal stress and defects in steel***, in: ***Technical Publications And Contributions***, (1941) pp. 1–38
111. N. Petch, P. Stables: ***Delayed fracture of metals under static load***, *Nature* 169 (1952), pp.842–843
112. S.P. Lynch: ***Mechanisms of Hydrogen-Assisted Cracking***, *METALS FORUM* 2 (1979), pp.189–200
113. X. Ren, Q. Zhou, W. Chu, J. Li, Y. Su, L. Qiao: ***The mechanism of nucleation of hydrogen blister in metals***, *Chinese Science Bulletin* 52 (2007), pp.2000–2005. DOI:10.1007/s11434-007-0269-y
114. A. Griesche, E. Dabah, T. Kannengießner, N. Kardjilov, A. Hilger, I. Manke: ***Three-dimensional imaging of hydrogen blister in iron with neutron tomography***, *Acta Materialia* 78 (2014), pp.14–22. DOI:10.1016/j.actamat.2014.06.034
115. H.H. Uhlig: ***An Evaluation of Stress Corrosion Cracking Mechanisms***, in: ***ASM-Corrosion Volume 13***, (1987) pp. 86–97
116. N. Petch: ***The lowering of fracture-stress due to surface adsorption***, *Philosophical Magazine* 1 (1956), pp.331–337
117. E.N. Pugh: ***A Post Conference Evaluation of Our Understanding of the Failure Mechanisms***, in: R.W. Staehle (Ed.), ***Stress Corrosion Cracking and Hydrogen Embrittlement of Iron Based Alloys***, Unieux-Firminy, France, (1973) pp. 37–51

118. J.E. Hack: ***On the reconciliation of reduced cohesion and enhanced plasticity mechanisms for hydrogen embrittlement***, *Scripta Metallurgica* 19 (1985), pp.543–545
119. D.G. Westlake: ***A generalized model for hydrogen embrittlement***, in: *Trans ASM*, (1969) pp. 1000–1006
120. D. Eliezer, E. Tal-Gutelmacher, Th. Böllinghaus: ***Hydrogen Embrittlement in Hydride and non Hydride-Forming Systems- Microstructural/Phase Changes and Cracking Mechanisms***, in: *ICF11, Italy 2005*, (2013)
121. D.S. Shih, I.M. Robertson, H.K. Birnbaum: ***HYDROGEN EMBRITTLEMENT OF a TITANIUM : IN SITU TEM STUDIES***, *Acta Metallurgica* 36 (1988), pp.111–124
122. D. Teter, I.M. Robertson, H.K. Birnbaum: ***The Effects of Hydrogen on the Deformation and Fracture of β -Titanium***, *Acta Materialia* 49 (2001), pp.4313–4323
123. C. Owen, T. Scott: ***Relation between hydrogen embrittlement and the formation of hydride in the group V transition metals***, *Metallurgical and Materials Transactions B* 3 (1972), pp.1715–1726
124. C.D. Cann, E.E. Sexton: ***An electron optical study of hydride precipitation and growth at crack tips in zirconium***, *Acta Metallurgica* 28 (1980), pp.1215–1221
125. S.P. Lynch: ***Hydrogen embrittlement phenomena and mechanisms***, *Corrosion Reviews* 30 (2012), pp.105–123. DOI:10.1515/corrrev-2012-0502
126. R. Frohberg, W. Barnett, A. Troiano: ***Delayed failure and hydrogen embrittlement in steel***, *Trans ASM* 47 (1954), pp.941–954
127. A. Troiano: ***The role of hydrogen and other interstitials in the mechanical behavior of metals***, *Trans. ASM* 52 (1960), pp.54–80
128. R. Oriani: ***A mechanistic theory of hydrogen embrittlement of steels***, *Berichte Der Bunsengesellschaft* (1972), pp.848–857
129. R.A. Oriani: ***Hydrogen embrittlement of steels***, *Annual Review of Materials Science* 8 (1978), pp.327–57. DOI:10.1126/science.179.4070.228-c
130. W.W. Gerberich, R.A. Oriani, M. Lji, X. Chen, T. Foecke: ***The necessity of both plasticity and brittleness in the fracture thresholds of iron***, *Philosophical Magazine A* 63 (1991), pp.363–376
131. S. Lee, D. Unger: ***A decohesion model of hydrogen assisted cracking***, *Engineering Fracture Mechanics* 31 (1988), pp.647–660
132. S.P. Lynch: ***Progress towards understanding mechanisms of hydrogen embrittlement and stress corrosion cracking***, in: *CORROSION 2007*, (2007) pp. 1–55

133. S. Gesari, M. Pronsato, A. Juan: **The electronic structure and bonding of H pairs at $\Sigma=5$ BCC Fe grain boundary**, *Applied Surface Science* 187 (2002), pp.207–217
134. C. Beachem: **A new model for hydrogen-assisted cracking (hydrogen “embrittlement”)**, *Metallurgical and Materials Transactions B* 3 (1972), pp.437–451
135. I.M. Robertson: **The effect of hydrogen on dislocation dynamics**, *Engineering Fracture Mechanics* 64 (1999), pp.649–673
136. D. Delafosse, T. Magnin: **Hydrogen induced plasticity in stress corrosion cracking of engineering systems**, *Engineering Fracture Mechanics* 68 (2001), pp.693–729
137. P. Ferreira, I.M. Robertson, H.K. Birnbaum: **Hydrogen effects on the interaction between dislocations**, *Acta Materialia* 46 (1998), pp.1749–1757
138. S.P. Lynch: **A Fractographic Study of Gaseous Hydrogen Embrittlement and Liquid-Metal Embrittlement in a Tempered Martensitic Steel**, *Acta Metallurgica* 32 (1984), pp.79–90
139. S.P. Lynch: **Mechanisms of Environmentally Assisted Cracking in Al-Zn-Mg Single Crystals**, *Corrosion Science* 22 (1982), pp.925–937
140. S.P. Lynch: **A fractographic study of hydrogen-assisted cracking and liquid-metal embrittlement in nickel**, *Journal of Materials Science* 21 (1986), pp.692–704. DOI:10.1007/BF01145543
141. S.P. Lynch: **ENVIRONMENTALLY ASSISTED CRACKING - OVERVIEW OF EVIDENCE FOR AN ADSORPTION-INDUCED LOCALIZED-SLIP PROCESS**, *Acta Metallurgica* 36 (1988), pp.2639–2661
142. S.P. Lynch: **Metallographic contributions to understanding mechanisms of environmentally assisted cracking**, *Metallography* 23 (1989), pp.147–171
143. A. Barnoush, H. Vehoff: **Recent developments in the study of hydrogen embrittlement: Hydrogen effect on dislocation nucleation**, *Acta Materialia* 58 (2010), pp.5274–5285. DOI:10.1016/j.actamat.2010.05.057
144. A. Barnoush, H. Vehoff: **Electrochemical nanoindentation: A new approach to probe hydrogen/deformation interaction**, *Scripta Materialia* 55 (2006), pp.195–198. DOI:10.1016/j.scriptamat.2006.03.041
145. A. Barnoush, M. Asgari, R. Johnsen: **Resolving the hydrogen effect on dislocation nucleation and mobility by electrochemical nanoindentation**, *Scripta Materialia* 66 (2012), pp.414–417
146. G.M. Pressouyre: **Trap theory of hydrogen embrittlement**, *Acta Metallurgica* 28 (1980), pp.895–911

147. G.M. Pressouyre, I.M. Bernstein: **An example of the effect of hydrogen trapping on hydrogen embrittlement**, *Metallurgical and Materials Transactions A* 12 (1981), pp.835–844
148. G.M. Pressouyre, I.M. Bernstein: **A quantitative analysis of hydrogen trapping**, *Metallurgical and Materials Transactions A* 9 (1978), pp.1571–1580.
DOI:10.1007/BF02661939
149. Th. Böllinghaus, H. Hoffmeister, L. Reuter: **Material properties of as delivered and quenched modified martensitic stainless steels dependent on hydrogen concentration**, in: **Supermartensitic Stainless Steels**, Brussels, (1999) pp. 264–271
150. Th. Böllinghaus, H. Hoffmeister, T. Tanski, H. Hoffmeister: **Wet H₂S Performance of a Delivered and Quenched Modified Martensitic Stainless Steels Determined by SSRT**, in: **CORROSION 99**, San Antonio, Tx, (1999)
151. Th. Böllinghaus, H. Hoffmeister, I. Stiebe-Springer, W. Florian, T. Michael: **Component Testing of Welded Supermartensitic Stainless Steel Pipes**, in: **Eurocorr; Past Success - Future Challenges**, London, (2000)
152. Th. Böllinghaus, H. Hoffmeister, S. Dietrich: **Slow Strain Rate Testing of Low Carbon Martensitic Stainless Steels**, *EFC Publications The Institute of Materials* (1998), pp.274–285
153. K.G. Solheim, J.K. Solberg, J. Walmsley, F. Rosenqvist, T.H. Bjørnå: **The role of retained austenite in hydrogen embrittlement of supermartensitic stainless steel**, *Engineering Failure Analysis* 34 (2013), pp.140–149.
DOI:10.1016/j.engfailanal.2013.07.025
154. I.C. Noyan, J.B. Cohen: **Fundamental concepts in X-ray Diffraction**, in: **Residual Stress Measurement by Diffraction and Interpretation**, Springer-Verlag, New York, (1987) pp. 75–116
155. a. Steuwer, J.R. Santisteban, M. Turski, P.J. Withers, T. Buslaps: **High-resolution strain mapping in bulk samples using full-profile analysis of energy dispersive synchrotron X-ray diffraction data**, *Nuclear Instruments and Methods in Physics Research Section B: Beam Interactions with Materials and Atoms* 238 (2005), pp.200–204. DOI:10.1016/j.nimb.2005.06.049
156. a. Steuwer, L. Edwards, S. Pratihari, S. Ganguly, M. Peel, M.E. Fitzpatrick, et al.: **In situ analysis of cracks in structural materials using synchrotron X-ray tomography and diffraction**, *Nuclear Instruments and Methods in Physics Research Section B: Beam Interactions with Materials and Atoms* 246 (2006), pp.217–225.
DOI:10.1016/j.nimb.2005.12.063
157. P.J. Withers, H. Bhadeshia: **Residual stress. Part 1—measurement techniques**, *Materials Science and Technology* 17 (2001), pp.355–365

158. P.J. Withers, H.K.D.H. Bhadeshia: **Residual stress. Part 2 – Nature and origins**, *Materials Science and Technology* 17 (2001), pp.366–375.
DOI:10.1179/026708301101510087
159. J. Toribio: **Role of crack-tip residual stresses in stress corrosion behaviour of prestressing steel**, *Construction and Building Materials* 12 (1998), pp.283–287.
DOI:10.1016/S0950-0618(98)00010-5
160. G. Vanboven, W. Chen, R. Rogge: **The role of residual stress in neutral pH stress corrosion cracking of pipeline steels. Part I: Pitting and cracking occurrence**, *Acta Materialia* 55 (2007), pp.29–42. DOI:10.1016/j.actamat.2006.08.037
161. S. Ghosh, V.P.S. Rana, V. Kain, V. Mittal, S.K. Baveja: **Role of residual stresses induced by industrial fabrication on stress corrosion cracking susceptibility of austenitic stainless steel**, *Materials & Design* 32 (2011), pp.3823–3831.
DOI:10.1016/j.matdes.2011.03.012
162. P.J. Withers, M. Turski, L. Edwards, P.J. Bouchard, D.J. Buttle: **Recent advances in residual stress measurement**, *International Journal of Pressure Vessels and Piping* 85 (2008), pp.118–127. DOI:10.1016/j.ijpvp.2007.10.007
163. J. Toribio, V. Kharin, M. Lorenzo, D. Vergara: **Role of drawing-induced residual stresses and strains in the hydrogen embrittlement susceptibility of prestressing steels**, *Corrosion Science* 53 (2011), pp.3346–3355.
DOI:10.1016/j.corsci.2011.06.012
164. H.-S. Kim, J.-K. Park, W.-S. Lee, Y.-J. Baik: **Variation of residual stress in cubic boron nitride film caused by hydrogen addition during unbalanced magnetron sputtering**, *Thin Solid Films* 519 (2011), pp.7871–7874.
DOI:10.1016/j.tsf.2011.06.092
165. J. Toribio, M. Lorenzo, D. Vergara, V. Kharin: **Effects of manufacturing-induced residual stresses and strains on hydrogen embrittlement of cold drawn steels**, *Procedia Engineering* 10 (2011), pp.3540–3545. DOI:10.1016/j.proeng.2011.04.583
166. A. Barnoush, M. Zamanzade, H. Vehoff: **Direct observation of hydrogen-enhanced plasticity in super duplex stainless steel by means of in situ electrochemical methods**, *Scripta Materialia* 62 (2010), pp.242–245.
DOI:10.1016/j.scriptamat.2009.11.007
167. A.J.C. Varandas, M.C. a. Gomes: **Diffusion coefficient of hydrogen atoms and molecules from accurate spherically averaged H-H 2 interaction potentials**, *Molecular Physics* 45 (1982), pp.317–329. DOI:10.1080/00268978200100261
168. E. Tal-Gutelmacher, A. Pundt, R. Kirchheim: **The effect of residual hydrogen on hydrogenation behavior of titanium thin films**, *Scripta Materialia* 62 (2010), pp.709–712. DOI:10.1016/j.scriptamat.2010.01.037

169. E. Lunarska, O. Chernyayeva: **Effect of corrosion inhibitors on hydrogen uptake by Al from NaOH solution**, *International Journal of Hydrogen Energy* 31 (2006), pp.285–293. DOI:10.1016/j.ijhydene.2005.04.051
170. C. Genzel, I. a. Denks, J. Gibmeier, M. Klaus, G. Wagener: **The materials science synchrotron beamline EDDI for energy-dispersive diffraction analysis**, *Nuclear Instruments and Methods in Physics Research Section A: Accelerators, Spectrometers, Detectors and Associated Equipment* 578 (2007), pp.23–33. DOI:10.1016/j.nima.2007.05.209
171. **ISO DIS 3690: Welding and allied processes: Determination of hydrogen content in ferritic steel arc weld metal**, (2009)
172. M. Klaus, C. Genzel, H. Holzschuh: **Residual stress depth profiling in complex hard coating systems by X-ray diffraction**, *Thin Solid Films* 517 (2008), pp.1172–1176. DOI:10.1016/j.tsf.2008.05.018
173. I.C. Noyan, J.B. Cohen: **Determination of Stress and Strain Fields by Diffraction Methods**, in: **Residual Stress Measurement by Diffraction and Interpretation**, Springer-Verlag, New York, (1987) pp. 117–163
174. M.E. Fitzpatrick, A.T. Fry, P. Holdway, F.A. Kandil, J. Shackleton, L. Suominen: **Determination of Residual Stresses by X-ray Diffraction - Issue 2**, (2005)
175. T. Kannengießer, A. Kromm, M. Rethmeier, J. Gibmeier, C. Genzel: **Residual Stresses and In-situ Measurement of Phase Transformation in Low Transformation Temperature (LTT) Welding Materials**, *Advances in X-Ray ...* (2009), pp.755–762
176. M.L. Martinez-Perez, F.J. Mompean, J. Ruiz-Hervias, C.R. Borlado, J.M. Atienza, M. Garcia-Hernandez, et al.: **Residual stress profiling in the ferrite and cementite phases of cold-drawn steel rods by synchrotron X-ray and neutron diffraction**, *Acta Materialia* 52 (2004), pp.5303–5313. DOI:10.1016/j.actamat.2004.07.036
177. T. Gnaeupel-Herold, H. Prask: **A synchrotron study of residual stresses in a Al6022 deep drawn cup**, *Materials Science and Engineering A and Engineering: A* 366 (2004), pp.104–113. DOI:10.1016/j.msea.2003.08.059
178. D.R.P. Singh, X. Deng, N. Chawla, J. Bai, C. Hubbard, G. Tang, et al.: **Residual stress characterization of Al/SiC nanoscale multilayers using X-ray synchrotron radiation**, *Thin Solid Films* 519 (2010), pp.759–765. DOI:10.1016/j.tsf.2010.08.148
179. A. Kromm, T. Kannengießer, J. Gibmeier: **Determination of residual stresses in low transformation temperature (LTT-) weld metals using X-ray and high energy synchrotron radiation**, *Welding in the World* 53 (2009), pp.3–16
180. E.S.. Laine: **A high-speed determination of the volume fraction of ferrite in austenitic stainless steel by EDXRD**, *Journal of Physics F: Metal Physics* 8 (1978), pp.1343–1348

181. Y. Park, I. Maroef, A. Landau, D. Olson: **Retained austenite as a hydrogen trap in steel welds**, *Welding Journal* (2002), pp.27–35
182. E. Dabah, T. Kannengießer, D. Eliezer, Th. Böllinghaus: **In situ analysis of hydrogen behaviour in stainless steels by high energy synchrotron radiation**, *Materials Science and Engineering: A* 528 (2011), pp.1608–1614. DOI:10.1016/j.msea.2010.10.090
183. H. Peisl: **Lattice strains due to hydrogen in metals**, in: *Hydrogen in Metals I*, (1978) pp. 53–74
184. J.-Y.J.-L.J.-Y.J.-L. Lee: **The hydrogen solubility in AISI 4340 steel in the temperature range of 298 to 873 K and atmospheric hydrogen pressure**, *Journal of Materials Science Letters* 1 (1982), pp.489–492. DOI:10.1007/BF00721937
185. G.C. Jr, R.S. Jr: **Hydrogen solubility in austenitic stainless steels**, *Scripta Metallurgica* (1981),
186. K. Kiuchi, R. McLellan: **The solubility and diffusivity of hydrogen in well-annealed and deformed iron**, *Acta Metallurgica* 31 (1983), pp.961–984
187. K.J.L. Iyer: **Effect of hydrogen on austenite to martensite transformation in an austenitic stainless steel**, *Journal of Materials Science Letters* 6 (1987), pp.869–871. DOI:10.1007/BF01729852
188. T.-P. Perng, C.J. Altstetter: **Hydrogen effects in austenitic stainless steels**, *Materials Science and Engineering: A* 129 (1990), pp.99–107. DOI:10.1016/0921-5093(90)90348-7
189. J. Brooks, A. West: **Hydrogen induced ductility losses in austenitic stainless steel welds**, *Metallurgical and Materials Transactions A* 12 (1981), pp.213–223
190. P. Rozenak, D. Eliezer: **Behavior of sensitized AISI types 321 and 347 austenitic stainless steels in hydrogen**, *Metallurgical and Materials Transactions A* 20 (1989), pp.2187–2190
191. P. Rozenak, D. Eliezer: **Nature of the γ and γ^* phases in austenitic stainless steels cathodically charged with hydrogen**, *Metallurgical and Materials Transactions A* 19 (1988), pp.723–730
192. P. Rozenak, A. Loew: **Stress distributions due to hydrogen concentrations in electrochemically charged and aged austenitic stainless steel**, *Corrosion Science* 50 (2008), pp.3021–3030. DOI:10.1016/j.corsci.2008.08.045
193. E. Dabah, T. Kannengießer, D. Eliezer, Th. Böllinghaus: **In situ synchrotron X-ray radiation analysis of hydrogen behavior in stainless steel subjected to continuous heating**, *Journal of Materials Science* 47 (2012), pp.5879–5885
194. W. Jiang, D. Ye, J. Li, J. Su, K. Zhao: **Reverse transformation mechanism of martensite to austenite**, *Steel Research International* 85 (2014), pp.1150–1157

195. L. Spieß, R. Schwarzer, H. Behnken, C. Genzel: **moderne röntgenbeugung**, Wiesbaden, (2005)
196. D. Eliezer: **The behaviour of 316L stainless steel in hydrogen**, *Journal of Materials Science* 18 (1984), pp.1540–1547
197. L. Chen, P. Shewmon: **Stress-assisted hydrogen attack cracking in 2.25 Cr-1Mo steels at elevated temperatures**, *Metallurgical and Materials Transactions A* (1995),
198. V. Olden, A. Alvaro, O.M. Akselsen: **Hydrogen diffusion and hydrogen influenced critical stress intensity in an API X70 pipeline steel welded joint—Experiments and FE simulations**, *International Journal of Hydrogen Energy* 37 (2012), pp.11474–11486. DOI:10.1016/j.ijhydene.2012.05.005
199. E. Dabah, T. Kannengießer, D. Eliezer, Th. Böllinghaus: **Hydrogen Interaction with Residual Stresses in Steel Studied by Synchrotron X-Ray Diffraction**, *Materials Science Forum* 772 (2014), pp.91–95. DOI:10.4028/www.scientific.net/MSF.772.91
200. I.C. Noyan, J.B. Cohen: **Effect of Stress Gradients Normal to the Surface on d vs. $\sin^2\psi$ Data**, in: **Residual Stress Measurement by Diffraction and Interpretation**, Springer-Verlag, New York, (1987) pp. 140–144
201. K. Beyer, T. Kannengießer, A. Griesche, B. Schillinger: **Neutron radiography study of hydrogen desorption in technical iron**, *Journal of Materials Science* 46 (2011), pp.5171–5175
202. K. Beyer, T. Kannengießer, A. Griesche, B. Schillinger: **Study of hydrogen effusion in austenitic stainless steel by time-resolved in-situ measurements using neutron radiography**, *Nuclear Instruments and Methods in Physics Research Section A: Accelerators, Spectrometers, Detectors and Associated Equipment* 651 (2011), pp.211–215. DOI:10.1016/j.nima.2011.02.010

8. List of Figures

Figure 1-1: A marine vessel for welding and placement of the SMSS pipelines for the oil and gas transportation industry	2
Figure 2-1: Schematic illustration of the microstructural features of SMSS	3
Figure 2-2: Schematic illustration of the interstitial sites (octahedral and tetrahedral sites) for foreign atoms in BCC and FCC crystal structures [50]	8
Figure 2-3: Evidence for the formation of hydrogen rich HCP ϵ^* phase after hydrogen charging up to 25 at.% in austenitic stainless steel [42]	9
Figure 2-4: Schematic view of examples of destinations for hydrogen in a metal microstructure: (a) solid solution; (b) solute–hydrogen pair; (c) dislocation atmosphere; (d) grain boundary accumulation; (e) particle-matrix interface accumulation; (f) void containing recombined hydrogen (redrawn from Dayal [57]).....	11
Figure 2-5: Schematic of energy near a trap site where S_T is the trap site, S_n is a lattice interstitial site, E_{aD} is the activation energy for hydrogen diffusion for an atom located in lattice interstitial site, E_s is the saddle energy, E_B is the trap binding energy (redrawn from Lee [62])	11
Figure 2-6: Schematic of energy steps necessary to the diffusion of hydrogen atom through a metal lattice in some particular cases: (a) existing attractive force, (b) distorted lattice, (c) attractive trap, (d) physical trap and (e) mixed trap where D_i is the effective size of the trap, E_d is the activation energy for diffusion and E_t is the activation energy of the trap [63].....	13
Figure 2-7: Thermal desorption spectrum of a LECO standard sample with a known hydrogen concentration [76]	16
Figure 2-8: Published values of hydrogen diffusion coefficients in two types of SMSS as a function of temperature [99] (the literature values are taken from [9])	19
Figure 2-9: Illustration of the principles of the pressure theory: It describes the formation of hydrogen molecules in microstructural defects [50,113]	22

- Figure 2-10: A cross section of hydrogen induced blister after electrochemical cathodic charging in technical iron of ARMCO grade. The formation of this blister is described in detail in [114] 22
- Figure 2-11: Schematic illustration of the absorption mechanism: hydrogen ion from the environment B, interacts and reduces the cohesive strength of strained bond A-A₀ at the tip of a crack (redrawn from Pugh [117]) 23
- Figure 2-12: Hydrogen induced cracks along the α phase boundaries in duplex Ti alloy, in the areas where hydride tend to form [120] 25
- Figure 2-13: Schematic diagram illustrating subcritical crack growth involving hydrogen diffusion to hydrostatically stressed regions, then formation and fracture of a brittle hydride at a crack tip (redrawn from Lynch [125]) 26
- Figure 2-14: HEDE mechanism, involving separation of atomic planes due to the weakening of the interatomic bonding by (i) solute hydrogen, (ii) absorbed hydrogen and (iii) hydrogen at particle-matrix interfaces [132] 27
- Figure 2-15: Steps in hydrogen enhanced local plasticity, HELP: (1) Slip planes activated at the crack tip, (2) enhanced plasticity on (111) planes due to hydrogen absorption, (3) pile up of dislocations near obstacle, (4) initiation of crack or micro void due to the local stress increase and (5) crack opens by shear De-cohesion along the slip plane [136] 29
- Figure 2-16: The influence of 90 torr hydrogen gas on dislocation configuration. The white dislocations show the position with hydrogen and the black dislocation show the initial position [137] 30
- Figure 2-17: Effect of introducing hydrogen into the controlled environment transmission electron microscope and hence into 310S stainless steel on the motion of extrinsic dislocations in a grain boundary [86] . The introduced hydrogen atmosphere pressure is stated in the images. The last image is a combination of the first and the third images 30
- Figure 2-18: Schematic diagrams illustrating (a) the adsorption induced dislocation emission (AIDE) mechanism for transgranular crack growth, which involves alternate-slip from crack tips facilitating coalescence of cracks with voids formed in the plastic zone ahead of cracks, and (b) ductile crack growth

involving coalescence of cracks with voids by egress of dislocations nucleated from near-crack-tip sources [142]..... 32

Figure 2-19: (a, b, c) External hydrogen atmosphere and transport by dislocation (a) the dislocation just nucleated at the surface has picked up hydrogen and moves toward the flaw. (b) On passing over an irreversible trap some hydrogen is lost (c) some more hydrogen is lost by the reversible trap. Thus the flaw sees less hydrogen coming in (a', b', c') material precharged and transport by dislocations. (a') hydrogen is distributed over all of the traps when the dislocation begin to move. (b') some hydrogen is lost on the irreversible trap (c') the dislocation recharge itself upon passing a reversible trap. Thus the flaw will see more hydrogen coming in [146] 35

Figure 2-20: Failures in the Tune pipeline that occurred due to HAC. The right side photos present failure of the weld due to hydrogen absorbed during welding process. The left side photos present failure induced after the reparation and coating process. Hydrogen was introduced through gaps in the coating and the cathodic protection that was applied to the flowline [23] 36

Figure 2-21: The changes of the real fracture strain due to hydrogen in SMSS (reconstructed from Böllinghaus [149]) 38

Figure 2-22: Optical microscopy and SEM inspection of the fracture surfaces of SMSS pipeline (a) overview (b) coarsened grains HAZ (c) main crack initiation in the HAZ (d) initiation of cracks at pits in the HAZ [151] 38

Figure 2-23: Without hydrogen charging (a) the area of crack initiation and (b) the central area of crack growth [19] 39

Figure 2-24: Charged with 3 wt. ppm hydrogen (a) area of crack initiation, (b) central area of crack growth and (c) area of near final fracture [19] 39

Figure 2-25: TEM micrographs showing microstructure immediately beneath the hydrogen assisted fracture surfaces characterized as (a) "flat", (b) "quasi cleavage" and (c) low temperature induced "quasi cleavage". Arrows and arrow heads indicate slip bands and lath boundaries, respectively [17] 40

Figure 2-26: SEM (Scanning Electron Microscopy) images of a martensitic steel subjected to a fatigue test at a stress amplitude of 610 MPa (a) with and (b) without hydrogen [16]	41
Figure 2-27: Loss of RA (the ratio between the cross section of the fractured sample and the initial cross section before testing) as a function of retained austenite for two types of SMSS pipeline steels (containing 12% Cr content) [153]	42
Figure 2-28: Illustration of constructive interference between X-ray photons according to Bragg's law	44
Figure 2-29: Classification of the three types of residual stresses according to their scale [157]	46
Figure 2-30: Distributions of relative concentrations of hydrogen (C/C^*) as a function of the dimensionless radial coordinate r/a , at diffusoin time of 200 hours, for three modeling scenes: stress-and-strain assisted diffusion (full line), stress-only assisted diffusion (dashed line) and conventional diffusion with no stress or strain assistance (dotted line) [165]	47
Figure 2-31: EC-AFM deflection mode images from the surface of the sample during in situ electrochemical H-charging. (a) Before H-charging at the open circuit potential; on the left is a ferrite grain and on the right is an austenite grain which can be easily distinguished by its convex grain boundary. (b) The image of the same position after 1 h of in situ H-charging. (c) The image of the same position after 2.5 h of in situ H-charging. (d) Higher magnification image from the surface of the austenite grain [166]	48
Figure 4-1: TEM image of the SMSS showing the martensitic lath microstructure and the austenite particles (see the black arrows) that are fined distributed between the martensitic laths [99]	53
Figure 4-2: Technical stress-strain diagram of the as received SMSS. The tensile test was conducted at BAM laboratory at room temperature	55
Figure 4-3: The electrochemical cathodic charging cell. The sample in the middle of the bottle which acts as a cathode, and the platinum electrode on the right side which acts as an anode	56
Figure 4-4: The laboratory setup of the CGHE system developed by JUWE	57

Figure 4-5: Schematic of the CGHE system 57

Figure 4-6: Calibration curve of the TCD signal dependency on hydrogen content in the carrier gas..... 58

Figure 4-7: Energy spectrum of the white beam through a pinhole of 1X1 mm² corresponding to a ring current of 250mA [110] 59

Figure 4-8: The experimental setup of the desorption at ambient temperature experiment 60

Figure 4-9: The experimental assembly in the EDDI experiments chamber at the synchrotron facility BESSY II in Berlin 60

Figure 4-10: An example of a diffraction spectrum of a steel sample, obtained using EDXRD [170]..... 61

Figure 4-11: An example of the fit of the diffraction line $\alpha(2\ 1\ 1)$ to the Pseudo-Voigt function (the black spots are the experimental results and the green curve is the fit) . 62

Figure 4-12: Photography of the specimen holder in the measurement chamber at the EDDI beamline. The cuboid sample is mounted in the centre of the specimen holder. Underneath the sample is the heating unit isolated from the sample with a ceramic layer 63

Figure 4-13: Schematic illustration showing diffraction planes parallel to the surface and at an angle φ_ψ . Note σ_{11} and σ_{22} both lie in the plane of the specimen surface (redrawn from Fitzpatrick [174])..... 65

Figure 4-14: Illustration of the angles and rotations used in residual stress measurements with the $\sin^2\psi$ (For the conducted measurements only 2θ) [174] 66

Figure 4-15: The G3 mobile diffractometer system for residual stresses measurement 67

Figure 4-16: The geometry of the tensile specimens for HE analysis 69

Figure 5-1: The microstructure of the as received material in the (a) perpendicular direction and in the (b) rolling direction 71

Figure 5-2: SEM image of the studied SMSS, where the martensitic laths can be clearly seen (This image is perpendicular to the rolling direction) 72

Figure 5-3: Tensile test results for a hydrogenated SMSS (red curve) and of an uncharged reference sample (blue curve) showing the drastic degradation of the ductility of the hydrogenated sample	73
Figure 5-4: Identified cracks, appearing during hydrogen electrochemical charging in the microstructure of the SMSS	74
Figure 5-5: CGHE analysis at around 900°C for the super martensitic "as charged" sample	76
Figure 5-6: Energy dispersive X-ray diffraction spectrums, taken immediately after charging (t=0), after 1 hour of degassing at ambient temperature (t=1). After 2 hours and after 24 hours of degassing of the hydrogenated sample at ambient temperature (t=2 and t=24)	77
Figure 5-7: The changing of the line's positions during degassing at room temperature of the austenitic phase related lines (a) γ (111) (b) γ (200) (c) γ (220) (d) γ (311)	79
Figure 5-8: The changing of the line's positions during degassing at room temperature of the ferrite/martensite phase related lines (a) α (110) (b) α (200) (c) α (211)..	79
Figure 5-9: The lattice parameter changes of the austenitic phase during degassing of a hydrogenated sample at room temperature (a) γ (111) (b) γ (200) (c) γ (220) (d) γ (311)	81
Figure 5-10: The lattice parameter changes of the ferritic/martensitic phase during degassing of a hydrogenated sample at room temperature (a) α (110) (b) α (200) (c) α (211)	81
Figure 5-11: Fitting of the effusion curve to the solution of Fick's second law	83
Figure 5-12: The line's positions related to the austenitic phase after prior degassing of 24 hours at room temperature (a) γ (111) (b) γ (200) (c) γ (220) (d) γ (311)	85
Figure 5-13: The line's positions related to the ferritic/martensitic phase after prior degassing of 24 hours at room temperature (a) α (110) (b) α (200) (c) α (211)	85

Figure 5-14: Illustration of the total shift of the austenitic diffraction line (2 0 0) during the degassing process at ambient temperature for (a) 2.5 hours and (b) 24 hours 86

Figure 5-15: The maximum lattice strain induced by hydrogen on the (a) austenitic and the (b) ferritic/martensitic phase 89

Figure 5-16: The changes of the broadness of the diffraction lines correlated with the austenitic phase (a) γ (111) (b) γ (200) (c) γ (220) (d) γ (311) 90

Figure 5-17: The martensite phase content in the sample during hydrogen desorption. the martensite content was calculated in accordance to Laine 92

Figure 5-18: Example of the obtained diffraction spectrums collected at 25, 300 and 625°C for a hydrogenated sample and a reference uncharged sample 93

Figure 5-19: Lattice parameter changes measured for the austenitic phase during heating of a hydrogenated sample and a reference sample up to 625°C (a) γ (111) (b) γ (200) (c) γ (220) (d) γ (311) 95

Figure 5-20: Lattice parameter changes measured for the martensitic/ferritic phase during heating of a hydrogenated sample and a reference sample up to 625°C (a) α (110) (b) α (200) (c) α (211) 95

Figure 5-21: The lattice parameter differences between the hydrogen charged sample and uncharged reference sample of the (a) austenitic phase and the (b) ferritic/martensitic phase 97

Figure 5-22: CGHE obtained curve for hydrogenated specimen heated with the same heating rate as used in the BESSY II experiment of 10K/min. the Y axis is the signal received from the TCD and is corresponded to the hydrogen content in the nitrogen carrier gas flux 98

Figure 5-23: Martensite fraction in the microstructure of the steel, calculated according to Laine [180], dependence of the time and temperature for the hydrogenated sample and the uncharged reference sample 100

Figure 5-24: Residual stresses measurement by means of the mobile X-ray diffractometer for the (211) crystallographic plane family 103

- Figure 5-25: The residual stresses and their distribution in the sample's bulk before and after hydrogen cathodic charging with different charging times for the (a) ferritic/martensitic phase and the (b) austenitic phase 105
- Figure 5-26: A $\sin^2\psi$ diagram taken from the beginning of the examination of the 1 hour charged sample. The deviation from linearity toward the right side of the diagram indicates the presence of stress gradient in the normal direction... 106
- Figure 5-27: The changes of the residual stresses vs. time as the 1 hour hydrogenated sample was being aged at room temperature for hydrogen desorption. The changes appear in both phases; the (a) ferritic/martensitic phase and the (b) austenitic phase 108
- Figure 5-28: The changes of the residual stresses vs. time as the 2 hours hydrogenated sample was being aged at room temperature for hydrogen desorption. The changes appear in both phases; the (a) ferritic/martensitic phase and the (b) austenitic phase 109
- Figure 5-29: The changes of the residual stresses vs. time as the 24 hours hydrogenated sample was being aged at room temperature for hydrogen desorption. The changes appear in both phases; the (a) ferritic/martensitic phase and the (b) austenitic phase 110
- Figure 5-30: The changes of the residual stresses as a function of the hydrogen content for the 1 hour hydrogenated sample. The changes are presented for both phases; the (a) ferritic/martensitic phase and the (b) austenitic phase 111
- Figure 5-31: The changes of the residual stresses as a function of the hydrogen content for the 2 hour hydrogenated sample. The changes are presented for both phases; the (a) ferritic/martensitic phase and the (b) austenitic phase 112
- Figure 5-32: The changes of the residual stresses as a function of the hydrogen content for the 24 hour hydrogenated sample. The changes are presented for both phases; the (a) ferritic/martensitic phase and the (b) austenitic phase 113

9. List of Tables

Table 2-1: The three main SMSS grade in accordance to the concentration of alloying elements (the values are presented in wt.-%) [34–36]	5
Table 2-2: Martensite start, martensite final and AC_1 temperatures of the martensitic stainless steel categories [33].....	5
Table 2-3: Binding energies of various types of hydrogen traps in steels (The data is obtained from thermal desorption analysis method and hydrogen permeation method performed by various researchers) [63,65]	14
Table 4-1: Chemical composition of the investigated SMSS as received from the manufacturer (values are given in wt.-%).....	54
Table 5-1: Summary of the mechanical properties of SMSS with and without the presence of hydrogen.....	74
Table 5-2: Calculated diffusion coefficients from the effusion curves	83
Table 5-3: The calculated lattice parameter of both phases in the sample after degassing in room temperature for 24 hours and the lattice parameter of the uncharged material . The values were calculated from the average position of the lines on the X axis (Energy value)	86
Table 5-4: Line shifts of the ferritic and austenitic phases	87
Table 5-5: The hydrogen concentration in the SMSS samples after various charging periods	104

Abbreviations

AFM - Atomic Force Microscopy
AIDE - Adsorption Induced Dislocation Emission
BAM - Bundesanstalt für Materialforschung und -Prüfung
BCC - Body Centered Cubic
BCT - Body Centered Tetragonal
CGHE - Carrier Gas Hot Extraction
EDXRD - Energy Dispersive X - Ray Diffraction
ELC - Extra Low Carbon
FCC - Face Centered Cubic
HAC - Hydrogen Assisted Cracking
HB - Hardness Brinell
HCP - Hexagonal Closed Pack
HE - Hydrogen Embrittlement
HEDE - Hydrogen Enhanced Decohesion
HELP - Hydrogen Enhanced Localized Plasticity
HIC - Hydrogen Induced Cracking
keV - kilo electron Volt
LC - Low Carbon
MPa - Mega Pascal
MVC - Microvoid Coalescence
OM - Optical Microscopy
ppm - parts per million
SEM - Scanning Electron Microscopy
SMSS - Supermartensitic Stainless Steel
TCD - Thermal Conductivity Detector
TDA - Thermal Desorption Analysis
TDS - Thermal Desorption Spectroscopy
TEM - Transmission Electron Microscopy
UTS - Ultimate Tensile Strength
Wt. - Weight
XRD - X-Ray Diffraction

Curriculum Vitae

Personal details:

Name: Dabah, Eitan

Born: 10th of September 1981 in Rishon Lezion, Israel

Nationality: Israeli

Education:

09/1987 – 07/1993	Oranim elementary school in Rishon Lezion
09/1993 – 06/1996	Aharon Karon middle school in Rishon Lezion
09/1996 – 06/1999	Gan-Nahum gymnasiums in Rishon Lezion
09/2004 – 07/2008	Bachelor of Science in materials engineering in Ben-Gurion University in Beer-Sheva, Israel
07/2007 – 09/2009	Master of Science in materials engineering in Ben-Gurion University in Beer-Sheva, Israel
01/2010 – 01/2015	Federal Institute for Materials Research and Testing in Berlin, Germany

Other:

03/2000 – 03/2003	Basic military service
09/2008 – 07/2009	teaching assistant at the department of material engineering, Ben-Gurion University
03/2009 – 07/2009	teaching assistant at the department of mechanical engineering, Sami-Shamun College of technology